Ph.D. DISSERTATION

Measurement of the differential Drell-Yan cross section in pp collisions at $\sqrt{s} = 13$ TeV with the CMS detector

CMS 검출기의 질량 중심 에너지 13 TeV 양성자-양성자 충돌 데이터를 이용한 Drell-Yan 과정의 미분 산란 단면적 측정

BY

Kyeongpil Lee

JULY 2020

DEPARTMENT OF PHYSICS AND ASTRONOMY
COLLEGE OF NATURAL SCIENCE
SEOUL NATIONAL UNIVERSITY

Ph.D. DISSERTATION

Measurement of the differential Drell-Yan cross section in pp collisions at $\sqrt{s} = 13$ TeV with the CMS detector

CMS 검출기의 질량 중심 에너지 13 TeV 양성자-양성자 충돌 데이터를 이용한 Drell-Yan 과정의 미분 산란 단면적 측정

BY

Kyeongpil Lee

JULY 2020

DEPARTMENT OF PHYSICS AND ASTRONOMY
COLLEGE OF NATURAL SCIENCE
SEOUL NATIONAL UNIVERSITY

Measurement of the differential Drell-Yan cross section in pp collisions at $\sqrt{s} = 13$ TeV with the CMS detector

CMS 검출기의 질량 중심 에너지 13 TeV 양성자-양성자 충돌 데이터를 이용한 Drell-Yan 과정의 미분 산란 단면적 측정

지도교수 양 운 기

이 논문을 이학박사 학위논문으로 제출함

2020 년 7 월

서울대학교 대학원

물리천문학부

이 경 필

이경필의 이학박사 학위논문을 인준함

2020 년 7 월

위 원 장 _____

부위원장 _____

위 원 _____

위 원 _____

위 원 _____

Abstract

This thesis describes the measurement of differential Drell-Yan (DY) cross section with respect to the dilepton mass with a range from 15 GeV to 3000 GeV in the dimuon and dielectron channel, which provides a precise test of the standard model and the improvement of the understanding of the proton structure. This is the first DY measurement at the center of mass energy of 13 TeV over a wide dilepton mass range from the region below Z resonance to the TeV scale. The results are based on the data from the proton-proton collision collected by the Compact Muon Solenoid detector at Large Hadron Collider, corresponding to an integrated luminosity of 2.8 (2.3)fb^{-1} for the dimuon (dielectron) channel. The differential cross sections with the corrections for the kinematic acceptance and the final state radiation (FSR) effect in the individual channels are presented. Another version of the results without the acceptance and FSR corrections is also presented to minimize the uncertainties from theoretical inputs. The results in the full phase space of the two channels are combined to have better precision after taking into account the correlations between channels and measurement bins. The presented results are compared to the next-to and next-to-next-to-leading order predictions at perturbative quantum chromodynamics, and the experimental results are in agreement with the theoretical predictions within associated uncertainties.

Keywords: SNU, High Energy Physics, LHC, CMS, Drell-Yan, Cross Section, Thesis

Student Number: 2014-21367

Contents

List of Figures

List of Tables

Chapter 1

Introduction

Since the atomic theory of Democritus in Ancient Greece, the idea on the indivisible constituents of everything in the universe fascinates physicists through the history of physics. Their efforts enable to finally develop one of the successful theories for the fundamental particles and their interactions in the modern particle physics, the standard model (SM). The SM explains the matters in the universe as the composition of a few elementary particles, the quarks and leptons. Their interactions are described by the quantum chromodynamics (QCD) for the strong interaction and the electroweak theory which unifies the electromagnetic and weak interactions. Furthermore, the origin of the mass of the elementary particles is explained by the Higgs mechanism. The predictions by the SM have been consistent with various experimental results. The discovery of W and Z boson from the Super Proton Synchrotron, the precision measurements for the electroweak observables from Large Electron-Positron Collider, and the discovery of the top quark by Collider Detector at Fermilab and D0 experiments are the famous examples of the success achieved by the

SM before the Large Hadron Collider (LHC) era.

However, still there are many open questions that cannot be explained by the SM, including the existence of the dark matter, non-zero mass of the neutrino predicted by the neutrino flavor oscillation, the asymmetry of matter and anti-matter in the universe, unification with the gravitational force, and so on. Therefore, the LHC, the largest particle collider in the world with the highest center of mass energy, has been built and started to operate since 2010 to find hints of the new physics beyond the SM (BSM) as well as the discovery of the last piece of the SM, Higgs boson. The latter one was accomplished by the A Toroidal LHC Apparatus (ATLAS) and Compact Muon Solenoid (CMS) collaborations in 2012, but there was no clear evidence found of new physics so far. Therefore, the efforts for the discovery of BSM is still ongoing and they are performed in two ways in general. The first one is the direct search for the feature of new physics like a resonance produced by a hypothetical particle predicted in BSM. The other way is the precision measurement of physics quantities in various physics processes. It provides the test of the validity of the SM with high precision. If a deviation between the SM prediction and the experimental result is found, it could provide a indirect hint of new physics.

The measurement of the cross section of the Drell-Yan (DY) process is one of the well-known precision measurements in experimental particle physics. The DY process in LHC is the process that produces two leptons in the final state from the decay of the Z boson or virtual photon, made by the annihilation of quark and anti-quark pair from two colliding protons. Due to its simple topology, the theoretical prediction of its production rate (cross section) by the SM is already well established up to next-to-next-to-leading order at perturbative QCD not only for the inclusive but also for the differential cross sections with respect to various observables. In the experimental side,

the cross section can precisely be measured due to its clean signature on particle detectors, which leads the high detection efficiency and resolution of lepton momentum. Therefore, the measurement of the differential DY cross section can provide a precise test of the SM.

Furthermore, the cross section results can contribute to improve the understanding on the structure of the proton. According to the SM, the proton is composed of quarks and gluons binded by the strong interaction. Their quantitative distributions cannot be computed with the perturbative QCD, and therefore it should be determined by fitting many experimental data. As the DY process occurs via the annihilation of quark and anti-quark, the differential cross section results can provide the information of the quark and anti-quark distribution in various energy scale. Because the knowledge on the structure of the proton is a vital ingredient to interpret the data collected in proton-proton collision in LHC, the improvement on the understanding of the proton structure has a global impact in LHC physics programs. IN parallel, the improved precision on DY production rate will increase the sensitivity for new physics searches with lepton final states where the DY process is one of the major backgrounds.

Due to its importance, the differential DY cross sections have been continuously measured in CMS using the data collected with the center of mass energy of 7 and 8 TeV. This thesis presents the latest result with the new center of mass energy, 13 TeV, using the data collected by CMS detector in 2015 corresponding to an integrated luminosity of about 3fb^{-1}. The cross section is measured with respect to the dilepton mass over a wide range from 15 GeV to 3000 GeV in the dimuon and dielectron channels.

The structure of the thesis is following. In chapter 2, the theoretical background behind the measurement is discussed. First of all, the standard model

is described, and the description on the current understanding of the proton structure is followed as well as its history. The theoretical cross section of the DY process and the motivation of its measurement are explained in the later section. In chapter 3, the LHC is introduced with its particle acceleration method and the particle detectors inside of it. The section for the CMS detector is followed with the details on each subsystem from the innermost to outermost subdetectors, as well as the trigger and data acquisition system. In chapter 4, the reconstruction algorithm of various physics objects is discussed. A special algorithm for the global event reconstruction is firstly introduced, and the details on the reconstruction of each object are followed. The analysis details are presented from chapter 5 to chapter 8. In chapter 5, the overview of the analysis is briefly introduced, and the description on the event selection method is followed as well as the data and MC samples. The procedure of the background estimation is illustrated in the last section. Chapter 6 is dedicated to the corrections applied to the signal yield from the data. It includes the corrections for the detector resolution, acceptance and efficiency, and the final state radiation effects. After the discussion on the estimation of the systematic uncertainty in chapter 7, the differential cross section results are presented in chapter 8. The procedure of the combination between two channels is also described with the combined results. Finally, in chapter 9, the contents are summarized with the conclusion of the thesis.

Chapter 2

Theoretical backgrounds

2.1 The Standard Model of particle physics

The standard model (SM) is one of the most successful theories to describe the interactions between the fundamental particles that compose the matter of the universe. In this section, the list of the fundemantal particles and their interactions are introduced, and the description on the SM Lagrangian which explains how the interactions works will be followed, including the Higgs mechanism.

2.1.1 Fundamental particles and their interactions

In SM, the fundamental constituents of the matter in the universe are the quarks and leptons with spin $\frac{1}{2}$ (fermions). The quarks (q), which can interact via all fundamental interactions in the SM (strong, electromagnetic and weak interactions), compose the bound states via strong interaction like meson (quark and anti-quark bound states) and baryon (three quark bound states). The proton and neutron, the constituent of the nucleus of atoms, are the famous example of the baryon. In contrast, leptons are not subjected to strong

interaction. Also, some of leptons called neutrino (ν) does not have the electric charge and it only interacts via weak interaction. The example of the lepton is the electron, which is also a constituent of atoms.

On the other hand, there is other type of particles in the SM called gauge bosons with integer spin. In the quantum field theory, the interaction (or "force") between fundamental particles is interpreted as the exchange of a particle that mediates the interaction, and the gauge bosons play a role of such mediator. The strong interaction is mediated by gluons (g) that have 8 different types depending on its "color" charge (the charge for strong interaction similar to the electric charge for electromagnetic interaction), and the interaction is described by the quantum chromodynamics (QCD). The electromagnetic and weak interactions are mediated by photon (γ) and massive W and Z bosons ($W^{\pm}$ and Z) respectively. Their interactions are described by the electroweak theory based on Quantum Electrodynamics (QED).

Finally, the scalar Higgs boson is the last particle in the SM as the origin of the mass of massive gauge bosons and fermions. The mechanism of how the Higgs boson gives masses to fundamental particles will be described in the later section 2.1.2.

The full list of the quarks, leptons, gauge and Higgs bosons are summarized in the Fig. 2.1 with their properties.

2.1.2 The SM Lagrangian

The SM is the quantum field theory invariant under the local gauge transformations in the symmetry group $\mathrm{SU(3)_C} \times \mathrm{SU(2)_L} \times \mathrm{U(1)_Y}$. $\mathrm{SU(3)_C}$ describes the strong interaction (QCD), and $\mathrm{SU(2)_L} \times \mathrm{U(1)_Y}$ represents the electroweak theory.

The mathematical structure of the interaction can be constructed by im-

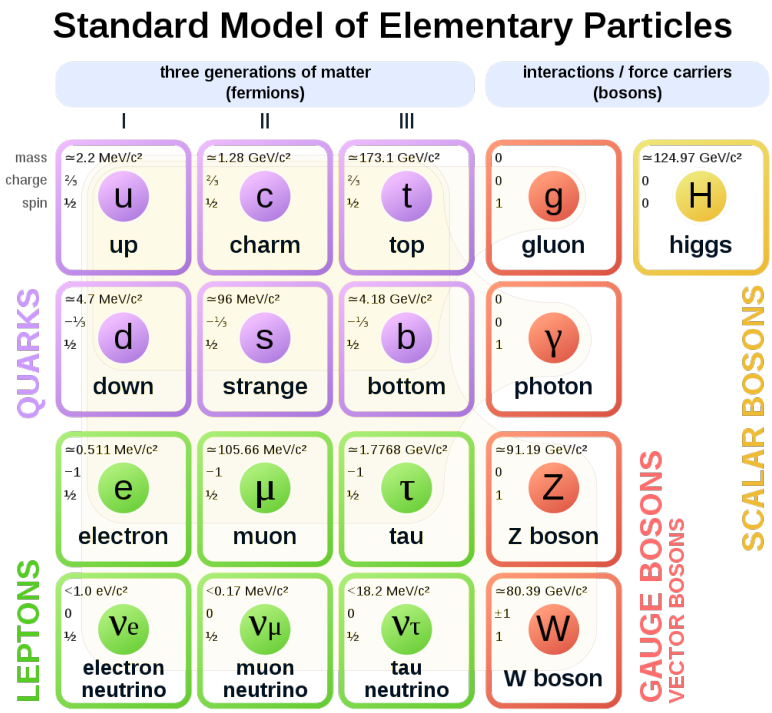

Figure 2.1: The list of the fundamental particles in SM with their properties [1].

posing the invariance under the local gauge transformations on the free fermion Lagrangian. The vector field that emerges in the modification of the Lagrangian to have gauge invariance, called gauge field, is associated to the mediator of the interaction (gauge bosons). The details will be discussed for each interaction below.

Electroweak interaction

The Lagrangian corresponding to Dirac equation that describes free particles with spin $\frac{1}{2}$ is:

$$\mathcal{L} = i\bar{\psi}\gamma_\mu\partial^\mu\psi - m\bar{\psi}\psi \tag{2.1}$$

In order to make the Lagrangian invariant under the local gauge transformation with an arbitrary function $\alpha(x)$, i.e.

$$\psi(x) \to e^{i\alpha(x)}\psi(x), \tag{2.2}$$

a new vector field is introduced with its transformation following the form:

$$A_\mu \to A_\mu + \frac{1}{e}\partial_\mu\alpha(x) \tag{2.3}$$

If a new derivative D_μ is defined with a new vector field A_μ like below,

$$D_\mu \equiv \partial_\mu - ieA_\mu \tag{2.4}$$

The Lagrangian

$$\mathcal{L} = i\bar{\psi}\gamma_\mu D^\mu\psi - m\bar{\psi}\psi \tag{2.5}$$

becomes invariant under the local gauge transformation. According to (2.5), interestingly, the A_μ field can be considered as the photon field in QED be-

cause it couples to ψ with the same form of the photon field. Therefore, to have a complete form of Lagrangian, the kinetic term of A_μ can be inserted with a gauge invariant form (strength tensor)

$$F_{\mu\nu} \equiv \partial_\mu A_\nu - \partial_\nu A_\mu \tag{2.6}$$

The final Lagrangian for QED can be constructed like below:

$$\begin{aligned} \mathcal{L} &= i\bar{\psi}\gamma_\mu D^\mu \psi - m\bar{\psi}\psi - \frac{1}{4}F_{\mu\nu}F^{\mu\nu} \\ &= \bar{\psi}(i\gamma_\mu \partial^\mu \psi - m)\psi + e\bar{\psi}\gamma^\mu A_\mu \psi - \frac{1}{4}F_{\mu\nu}F^{\mu\nu} \end{aligned} \tag{2.7}$$

One thing to notice is that the mass term of the photon field A_μ ($\sim m^2 A_\mu A^\mu$) is not allowed in the Lagrangian as it violates the local gauge invariance. In other words, the theory requires that the photon is massless.

The next step is to extend the same idea to the electroweak theory. In the theory, the electromagnetic and weak currents are unified in $\mathrm{SU(2)_L} \times \mathrm{U(1)_Y}$ symmetry group by weak isotriplet and isosinglet currents.

The weak isotriplet current is expressed like below with the three vector bosons W^μ:

$$-ig\bar{\chi_L}\gamma_\mu T \cdot W^\mu \chi_L \qquad (\mathrm{SU(2)_L}) \tag{2.8}$$

where g is the coupling constant associated to $\mathrm{SU(2)_L}$ and T is the generator of $\mathrm{SU(2)_L}$ group that satisfies $[T^i, T^j] = i\epsilon_{ijk}T^k$ with the antisymmetric tensor e_{ijk}. χ_L is the weak isospin doublet for left-handed fermions, e.g. $\chi_L = \begin{pmatrix} \nu \\ e^- \end{pmatrix}_L$.

The weak isosinglet current (also called as weak hypercharge current) is:

$$-ig'\bar{\psi}\gamma_\mu \frac{Y}{2}\psi B^\mu \qquad (\mathrm{SU(1)_Y}) \tag{2.9}$$

where g' is the coupling constant associated to $\mathrm{SU(1)_Y}$ and Y is the weak hypercharge that also plays a role as the generator of $\mathrm{U(1)_Y}$. The electric charge Q, the third component of weak isospin T^3 and Y are connected via the relation below:

$$Q = T^3 + \frac{Y}{2} \tag{2.10}$$

After the electromagnetic current is replaced by weak isosinglet and triplet currents, again the Lagrangian is required to be invariant under local gauge transformations in $\mathrm{SU(2)_L} \times \mathrm{U(1)_Y}$:

$$\begin{aligned} \chi_L &\to e^{i\alpha(x)\cdot T + i\beta(x)Y}\chi_L \\ \psi_R &\to e^{i\beta(x)Y}\psi_R \end{aligned} \tag{2.11}$$

for arbitrary functions $\alpha(x)$ and $\beta(x)$. The behavior of B_μ under the gauge transformation and the modification of the derivative associated to B_μ can be inferred from A_μ case in QED ((2.3) and (2.4)) as they are both U(1) group. In the case of W_μ associated to $\mathrm{SU(2)_L}$, it is required to transform under the gauge transformation as:

$$W_\mu \to W_\mu - \frac{1}{g}\partial_\mu \alpha - \alpha \times W_\mu \tag{2.12}$$

Then, the local gauge invariance of SU(2) group can be obtained via the modification of the derivative below:

$$\partial_\mu \to \partial_\mu + ig\frac{\tau}{2}W_\mu \tag{2.13}$$

where τ denotes the Pauli matrices.

With the combination of needed modifications from $\mathrm{SU(2)_L}$ and $\mathrm{U(1)_Y}$, the Lagrangian of the electroweak interaction with local gauge invariance can be constructed including the kinetic term for the gauge bosons:

$$\begin{aligned}\mathcal{L} &= \bar{L}\gamma^{\mu}\left(i\partial_{\mu} - g\frac{1}{2}\tau W_{\mu} - g'\frac{Y}{2}B_{\mu}\right)L \\ &+ \bar{R}\gamma^{\mu}\left(i\partial_{\mu} - g'\frac{1}{2}YB_{\mu}\right)R \\ &- \frac{1}{4}W_{\mu\nu}W^{\mu\nu} - \frac{1}{4}B_{\mu\nu}B^{\mu\nu}\end{aligned} \tag{2.14}$$

where L (R) represents the left-handed (right-handed) fermion doublet (singlet).

The field strength $W_{\mu\nu}$ and $B_{\mu\nu}$ are defined as:

$$\begin{aligned}W_{\mu\nu} &\equiv \partial_{\mu}W_{\nu} - \partial_{\nu}W_{\mu} - gW_{\mu} \times W_{\nu} \\ B_{\mu\nu} &\equiv \partial_{\mu}B_{\nu} - \partial_{\nu}B_{\mu}\end{aligned} \tag{2.15}$$

The difference of the form of $W_{\mu\nu}$ with respect to $B_{\mu\nu}$ comes from the non-Abelian character of the group (i.e. group multiplication is not commutative).

Strong interaction

Similar to the construction of Lagrangian of electroweak interaction, the starting point is the Lagrangian of the free quarks:

$$\mathcal{L} = \bar{q_j}\left(i\gamma^{\mu}\partial_{\mu} - m\right)q_j \tag{2.16}$$

with j=1, 2, 3 for different color states for a quark flavor.

The local gauge transformation under $\mathrm{SU(3)_C}$ is expressed as:

$$q(x) \to Uq(x) = e^{i\alpha_a(x)T_a}q(x) \tag{2.17}$$

where $\alpha(x)$ is an arbitrary function and T_a (a=1, 2 ... 8) is the generator of $\mathrm{SU(3)_C}$ group. The commutation relation of T_a is

$$[T_a, T_b] = i f_{abc} T_c \tag{2.18}$$

with the structure constant of the group f_{abc}. As the generators are not commute each other, the $\mathrm{SU(3)_C}$ is also non-Abelian group.

To obtain the Lagrangian invariant under local gauge transformation (2.17), new (eight) gauge fields G^a_μ are needed which transform like below:

$$G^a_\mu \to G^a_\mu - \frac{1}{g_s}\partial_\mu \alpha_a - f_{abc}\alpha_b G^c_\mu \tag{2.19}$$

where g_s is the coupling constant of the strong interaction.

With such G_μ, the replacement of the derivative in the Lagrangian (2.16) with the form

$$\partial_\mu \to \partial_\mu + i g_s T_a G^a_\mu \tag{2.20}$$

makes the Lagrangian invariant under local gauge transformation.

The final form of the Lagrangian including the kinetic term of the gauge bosons is:

$$\mathcal{L} = \bar{q}\left(i\gamma^\mu \partial_\mu - m\right) q - g_s \left(\bar{q}\gamma^\mu T_a q\right) G^a_\mu - \frac{1}{4} G^a_{\mu\nu} G^{\mu\nu}_a \tag{2.21}$$

where

$$G^a_{\mu\nu} \equiv \partial_\mu G^a_\nu - \partial_\nu G^a_\mu - g_s f_{abc} G^b_\mu G^c_\mu \tag{2.22}$$

Similar to QED, the mass term of G^a_μ is not allowed to conserve the gauge invariance of the Lagrangian. The gauge boson corresponds to G^a_μ should be massless, which is in agreement with gluons.

Higgs mechanism

The Lagrangian of the strong and electroweak interactions with fundamental particles are constructed above, but the terms to explain the mass of fermions and massive gauge bosons ($W^{\pm}$ and Z) were missing, which should exist to be consistent with experimental results. As discussed earlier, direct insert of the mass terms ($\sim m^2\bar{\psi}\psi$) is not preferable as it ruins the gauge invariance of the Lagrangian. However, there is a way to generate the mass terms without violating the invariance via "spontaneous symmetry breaking".

To understand the idea, consider a simple Lagrangian for a complex scaler field $\phi = (\phi_1 + i\phi_2)/\sqrt{2}$ such that:

$$\mathcal{L} = |\partial_\mu \phi|^2 - \mu^2|\phi|^2 - \lambda|\phi|^4 \tag{2.23}$$

If the local gauge invariance under U(1) is imposed using the same technique for QED Lagrangian (2.7), the Lagrangian is changed like below:

$$\mathcal{L} = |D_\mu \phi|^2 - \mu^2|\phi|^2 - \lambda|\phi|^4 - \frac{1}{4}F_{\mu\nu}F^{\mu\nu} \tag{2.24}$$

The shape of the potential term of the scaler field $V(\phi) = \mu^2|\phi|^2 + \lambda|\phi|^4$, is shown in Fig. 2.2. The position of the minimum is given by the expression below:

$$\phi_1^2 + \phi_2^2 = v^2 \qquad (v \equiv -\frac{\mu^2}{\lambda}) \tag{2.25}$$

If a perturbation near the minimum is performed with a choice

$$\phi(x) = \frac{1}{\sqrt{2}}[v + \eta(x) + i\xi(x)], \tag{2.26}$$

The Lagrangian is changed to:

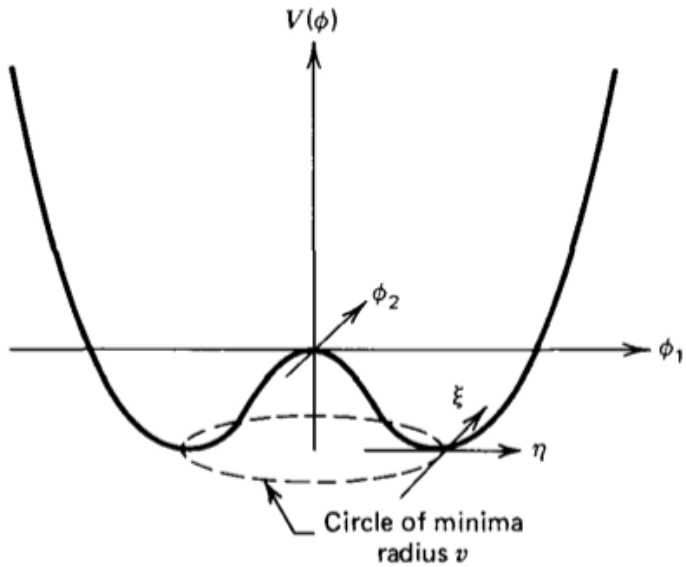

Figure 2.2: The shape of the potential of the complex scalar field ϕ [2].

$$\mathcal{L} = \frac{1}{2}(\partial_\mu \xi)^2 + \frac{1}{2}(\partial_\mu \eta)^2 - \frac{1}{2}(\sqrt{2\lambda v^2})\eta^2 + \frac{1}{2}e^2 v^2 A_\mu A^\mu ... \tag{2.27}$$

If $\lambda > 0$ and $\mu^2 < 0$, the above Lagrangian can be interpreted as the interaction of 2 real scaler bosons (η, ξ) and 1 vector boson (A) with their masses:

$$m_\xi = 0, \qquad m_\eta = \sqrt{2\lambda v^2}, \qquad m_A = ev \tag{2.28}$$

Therefore, by the choice on the form of the scaler field near minimum that leads the symmetry breaking ("spontaneous symmetry breaking"), the vector boson can acquire the mass.

However, the total degree of freedom (dof) in the Lagrangian seems not consistent with this form. At the beginning, the total dof is 4 that comes from 2 dof in complex scalar field (ϕ_1, ϕ_2) and 2 dof in massless vector field A. After

the substitution (2.26), total dof seems to 5 as each η and ξ has 1 dof and massive vector field A has 3 dof. The spurious additional dof can be removed by the gauge transformation such that:

$$\phi(x) \to \frac{1}{\sqrt{2}}[v + h(x)] \tag{2.29}$$

and the final Lagrangian with correct degree of freedom is:

$$\mathcal{L} = \frac{1}{2}(\partial_\mu h)^2 - \frac{1}{2}(\sqrt{2\lambda v^2})h^2 + \frac{1}{2}e^2 v^2 A_\mu A^\mu + ... \tag{2.30}$$

As seen, the massless scalar boson (Goldstone boson) is absorbed to the vector boson mass and removed from the Lagrangian by the gauge transformation. The remaining particles are the massive vector boson A and scalar boson h called Higgs boson. The procedure to generate mass of fields without breaking local gauge invariance is called Higgs mechanism.

Final Lagrangian

With the combination of the Lagrangian for the electroweak and strong interactions as well as the Higgs mechanism, the SM Lagrangian can be expressed like below:

$$\begin{aligned}
\mathcal{L}_{\text{SM}} = & -\frac{1}{4}G^a_{\mu\nu}G^{\mu\nu}_a - \frac{1}{4}W_{\mu\nu}W^{\mu\nu} - \frac{1}{4}B_{\mu\nu}B^{\mu\nu} \\
& + \bar{q}\gamma^\mu \left(i\partial_\mu - g_s T_a G^a_\mu\right) q \\
& + \bar{L}\gamma^\mu \left(i\partial_\mu - g\frac{1}{2}\tau_a W^a_\mu - g'\frac{1}{2}YB_\mu\right) L \\
& + \bar{R}\gamma^\mu \left(i\partial_\mu - g'\frac{1}{2}YB_\mu\right) R \\
& + \left|\left(i\partial_\mu - g\frac{1}{2}\tau_a W^a_\mu - g'\frac{1}{2}YB_\mu\right)\phi\right|^2 - V(\phi) \\
& - (G_1\bar{L}\phi R + G_2\bar{L}\phi_c R + \text{hermitian conjugate})
\end{aligned} \tag{2.31}$$

The first line represents the self interactions of the gauge bosons.

The second line describes the strong interactions between gluons and quarks (q). Other fermions are not included in the expression as they are not have color charge. The following third and forth lines are related to the interactions between electroweak gauge bosons and fermions. As the charged electroweak current only couples to the left-handed fermions, the expression is different between L and R.

The fifth line is inserted to provide the mass term of the massive electroweak gauge bosons ($W^{\pm}$ and Z) via Higgs mechanism using the complex scalar field invariant under SU(2)×SU(1) local gauge transformation.

The last line is also associated to Higgs mechanism to provide the mass of the fermions. $\phi_c = -i\tau_2\phi^*$ is introduced to generate the mass term of up-type quarks in a quark doublet.

2.2 The structure of the proton

In this section, the history and current understanding on the structure of the proton is discussed. Firstly, a brief history about understanding of the proton structure is introduced including flavor SU(3) symmetry and quark model, deep inelastic electron-proton scattering experiments with the interpretation of the results using parton model, and the validity of the interpretation of partons as quarks and gluons. After that, the details on the modern parton distribution function (PDF), which contains the information on the proton structure, are discussed. The general method to determine the PDF via global QCD analyses is presented, followed by a few example of modern PDFs.

2.2.1 Proton structure in quark model

Isospin symmetry

After the discovery of the neutron, nuclear physicists found that the proton and neutron mass are quite similar each other ($m_{\text{proton}} = 938.27\,\text{MeV}$, $m_{\text{neutron}} = 939.57\,\text{MeV}$). It tempts them to treat the proton and neutron as two manifestations of a single particle called "nucleon", like the electrons with different spins. Therefore, the concept of isospin is developed by Heisenberg to express the proton and neutron with two different isospin states of a nucleon by copying the algebra for spin. The proton is treated as the nucleon with $I_3 = \frac{1}{2}$, and the neutron is the counterpart of neutron with $I_3 = -\frac{1}{2}$ like below:

$$p = |I = \frac{1}{2}, I_3 = \frac{1}{2}\rangle\,, n = |I = \frac{1}{2}, I_3 = -\frac{1}{2}\rangle \tag{2.32}$$

As an example of usefulness of the isospin concept, the two nucleon system can be expressed by adding proton and neutron isospin states similar to a carbon copy of two electron system:

$$\begin{aligned}
&|I = 1, I_3 = 1\rangle = |\frac{1}{2}, \frac{1}{2}\rangle\,|\frac{1}{2}, \frac{1}{2}\rangle = pp \\
&|I = 1, I_3 = 0\rangle = \sqrt{\frac{1}{2}}(|\frac{1}{2}, \frac{1}{2}\rangle\,|\frac{1}{2}, -\frac{1}{2}\rangle + |\frac{1}{2}, -\frac{1}{2}\rangle\,|\frac{1}{2}, \frac{1}{2}\rangle) = \sqrt{\frac{1}{2}}(pn + np) \\
&|I = 1, I_3 = -1\rangle = |\frac{1}{2}, -\frac{1}{2}\rangle\,|\frac{1}{2}, -\frac{1}{2}\rangle = nn \\
&|I = 0, I_3 = 0\rangle = \sqrt{\frac{1}{2}}(|\frac{1}{2}, \frac{1}{2}\rangle\,|\frac{1}{2}, -\frac{1}{2}\rangle - |\frac{1}{2}, -\frac{1}{2}\rangle\,|\frac{1}{2}, \frac{1}{2}\rangle) = \sqrt{\frac{1}{2}}(pn - np)
\end{aligned} \tag{2.33}$$

By various experiments and observations, it is found that the nuclear force (strong interaction) does not distinguish between proton and neutron. For example, the mass of ^{6}He($= {}^4\text{He} + nn$), excited ^{6}Li($= {}^4\text{He} + np$) and

^{6}Be($= {}^4\mathrm{He} + pp$) is degenerated after corrections for the electromagnetic effects. It can be interpreted that the nuclear force is invariant under the isospin transformation (i.e. nuclear force is invariant under the rotation in the isospin space: the force is same for any I_3), which called as the isospin symmetry.

In terms of group theory, the isospin symmetry can be described by SU(2) by regarding the proton and neutron as the fundamental representation.

Flavor SU(3) symmetry and the quark model

In 1950s, a new type of hadrons is discovered with long lifetime compared to the time scale of the decay governed by the strong interaction. Even though their masses are heavy enough to decay into lighter objects without any violation of conservation laws known at the time (charge and baryon number conservation), they survived much longer than the expectation. For instance, according to Table 2.1, the decay mode of Δ^- and Σ^- baryon is exactly same but the difference of the lifetime is huge, $\mathcal{O}(10^{13})$s, even though their masses are quite close each other.

To explain the behavior of this kind of strange particles, Gell-Mann and Nishijima proposed a new quantum number called "strangeness" assigned to each baryon with an integer. Under the assumption that the strangeness should be conserved in strong and electromagnetic interactions, the strange behaviors are successfully explained. For example, the long lifetime of Σ^- baryon can be understood in the way that the strangeness of Σ^- baryon is -1, but the strangeness of n and π^- is 0. Therefore, the decay $\Sigma^- \to n\pi^-$ is forbidden to strong interaction, and only happens via weak interaction which can violate the conservation law of the strangeness. However, the decay of Δ^- baryon $\Delta^- \to n\pi^-$ can happen via strong interaction as the strangeness of Δ^- baryon is 0 and the strangeness of the reaction is conserved.

Baryon	Mass	Lifetime
Δ^-	1232 MeV	$\tau(\Delta^- \to n\pi^-) \sim 10^{-23}$s
Σ^-	1193 MeV	$\tau(\Sigma^- \to n\pi^-) \sim 10^{-10}$s

Table 2.1: Comparison of the lifetime between Δ^- and Σ^- baryon with same decay mode.

Due to the success of the strangeness concept, it was natural to extend the isospin symmetry to a larger group, SU(3), including the strangeness. It is called as flavor SU(3) to distinguish it from $SU(3)_C$ for QCD with colors.

In 1961, Gell-Mann and Ne'eman proposed a group of mesons and baryons in SU(3) representations called "Eightfold way" as seen in Fig. 2.3. The particles are aligned with respect to the their strangeness and the electric charge (or they can be represented with respect to hypercharge, the sum of the baryon number and strangeness, and isospin).

One of the triumph of the Eightfold way is the prediction of Ω^- baryon, which was not discovered yet when the Eightfold way was proposed. Ω^- baryon was predicted as the last particle at the bottom of baryon decuplet by Gell-Mann in 1962. Its mass was also predicted by the "equal mass spacing rule" in decuplet, which is a empirical rule that the particle mass linearly increases with its strangeness. Finally, it was discovered by an experiment at Brookhaven with the predicted mass [3] in 1964.

Therefore, the singlets, octets and decuplets of hadrons are completed in SU(3) representation, but the triplets as the fundamental representation of SU(3) were not discovered yet. Gell-Mann and Zweig proposed hypothetical particles called "quarks" ("aces" in Zweig's term) corresponding to the SU(3) triplets. The individual quarks are denoted as u, d and s corresponding to

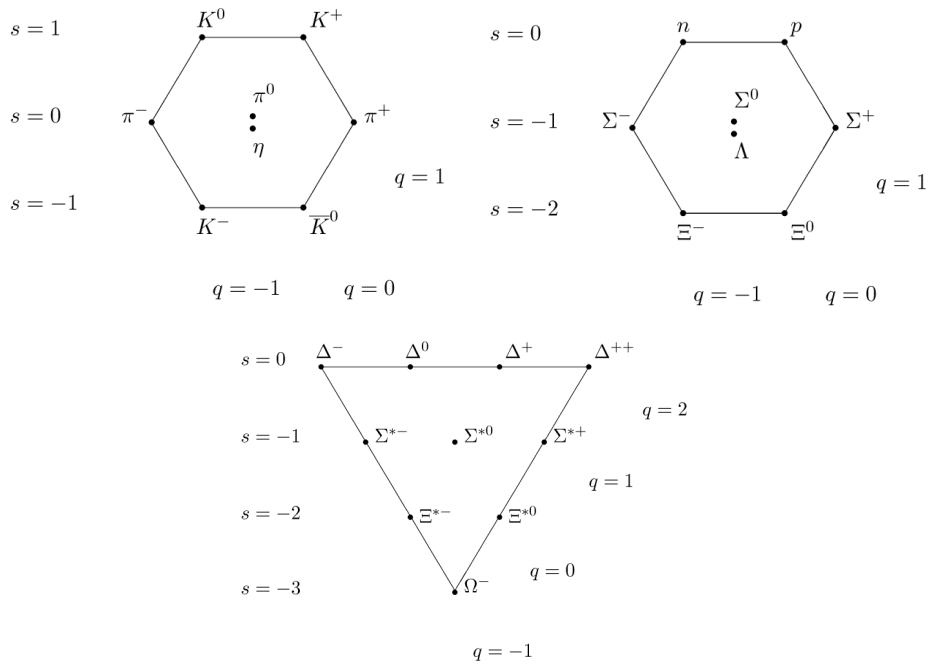

Figure 2.3: The eightfold way, the group of mesons and baryons in SU(3) representation suggested by Gell-Mann and Ne'eman in 1961. Top two plots show the meson nonet (octet plus singlet η) (left) and baryon octet with spin $J = \frac{1}{2}$ (right). The bottom plot is the baryon decuplet with spin $J = \frac{3}{2}$.

up, down and strange quark respectively, and their fractional electric charges and baryon numbers are shown in Fig. 2.2. Any representation (mesons and baryons) can be built by combining the quarks as they are the fundamental representation of SU(3), and this indicates that the quark is the constituent of the hadrons. However, when it was invented, it was considered as just a mathematical tool to build the hadron's SU(3) group as there was no evidence of the existence of quarks at the time. The quarks were accepted as physical particles after deep inelastic electron-nucleon scattering experiments, which provides indirect evidence of quarks inside of nucleons.

Quark	Electric charge	Baryon number	Strangeness
Up quark (u)	$\frac{2}{3}$	$\frac{1}{3}$	0
Down quark (d)	$-\frac{1}{3}$	$\frac{1}{3}$	0
Strange quark (s)	$-\frac{1}{3}$	$\frac{1}{3}$	-1

Table 2.2: List of quarks and their properties in flavor SU(3).

2.2.2 Deep inelastic electron-nucleon scattering

Scattering experiment by firing particles to a target has been frequently used as the method to understand the structure of the target through the history of physics. One of the well-known example is the Rutherford scattering experiment, which leads the discovery of nucleus inside of atoms. The similar approach was performed by scattering electrons to the proton and neutron targets to understand the substructure of the nucleons.

Elastic electron-proton scattering

In the electron-proton scattering experiment, the proton is seen as a particle with finite size if the energy of the electron beam is not enough to provide smaller wavelength of virtual photon than the size of proton, which is called as *elastic electron-proton scattering* shown in Fig. 2.4.

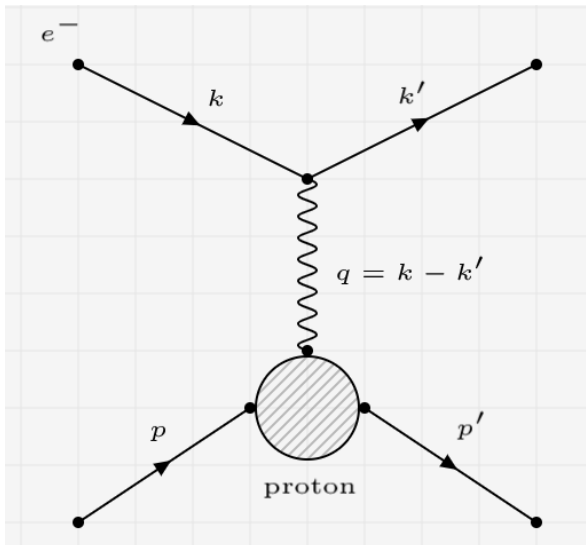

Figure 2.4: Elastic electron-proton scattering.

In this case, the cross section of the scattering can be obtained by the analogy of the electron scattering to a point-like particle (e.g. muon) with "form factors" that contains the information about the detailed structure of proton. After taking into account the recoil of the proton and its magnetic moment, the differential cross section of the scattering can be expressed by the Rosenbluth formula below:

$$\frac{d\sigma}{d\Omega} = \frac{\alpha^2}{4E^2 \sin^4 \theta/2} \frac{E'}{E} \left(\frac{G_E^2 + \tau G_M^2}{1+\tau} \cos^2 \frac{\theta}{2} + 2\tau G_M^2 \sin^2 \frac{\theta}{2} \right) \\ \left(E/E' = 1 + \frac{2E}{M} \sin^2 \frac{\theta}{2} \right) \tag{2.34}$$

where E and E' are the initial and final energy of the electron, α is the fine structure constant ($\sim 1/137$), M is the proton mass, θ is the scattered angle of electron, τ is $-q^2/4M$ with $q = k - k'$ as shown in Fig. 2.4 (momentum transfer), and $G_M(q^2)$ and $G_E(q^2)$ are the proton form factors as a function of q^2 which can be determined by experimental data. The dependence of form factors on q^2 indicates that the observable proton structure depends on the energy of the virtual photon.

Deep inelastic electron-proton scattering

If the energy of the electron increased compared to the elastic scattering case, the proton target could be excited or even start to break up into hadrons after the collision ($ep \to eX$) as seen in Fig. 2.5. This is called as *deep inelastic electron-proton scattering* (DIS).

In contrast to the elastic scattering, the propagator of the hardon's final state is not clearly known. The ignorance on the hadron's final state is encoded in "structure function" that can be experimentally determined, and the differential cross section of the scattering can be expressed like below:

$$\frac{d\sigma}{dE' d\Omega} = \frac{\alpha^2}{4E^2 \sin^4 \frac{\theta}{2}} \left(W_2 \cos^2 \frac{\theta}{2} + 2W_1 \sin^2 \frac{\theta}{2} \right) \tag{2.35}$$

where $W_1(\nu, q^2)$ and $W_2(\nu, q^2)$ are the structure functions depending on $\nu = E - E'$ and q^2.

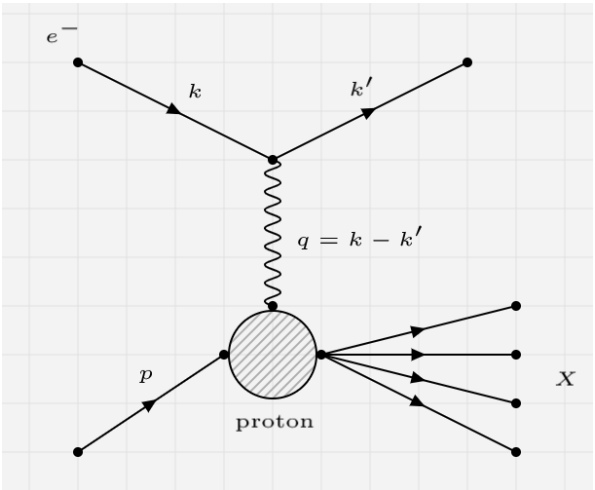

Figure 2.5: Deep inelastic electron-proton scattering ($ep \to eX$).

Bjorken Scaling and Parton model

However, in last 1960s, an interesting behavior of the structure functions is observed in a DIS experiments with high Q^2 ($Q^2 = -q^2$) at Stanford Linear Accelerator Center (SLAC) using up to 20 GeV electron beam (SLAC-MIT DIS experiments). The DIS cross section as a function of momentum transfer Q^2 didn't fall sharper like the elastic scattering case as shown in Fig. 2.6. This indicated that the structure of the proton could be different with a soft proton without any core, which was believed at the time by elastic scattering experiments.

In 1968, Bjorken predicted that the structure functions $W_1(\nu, q^2)$ and $W_2(\nu, q^2)$ will only depend on the ratio $\omega = 2m_p\nu/Q^2$ with proton mass m_p [4]. In other words, the structure function is independent of Q^2 in same ω, which is impossible if the electron scattered to a particle with finite size as shown in the dependence of proton form factors G_E and G_M on Q^2 in the elastic ep scattering. The Bjorken's prediction was proven to be true by DIS data from

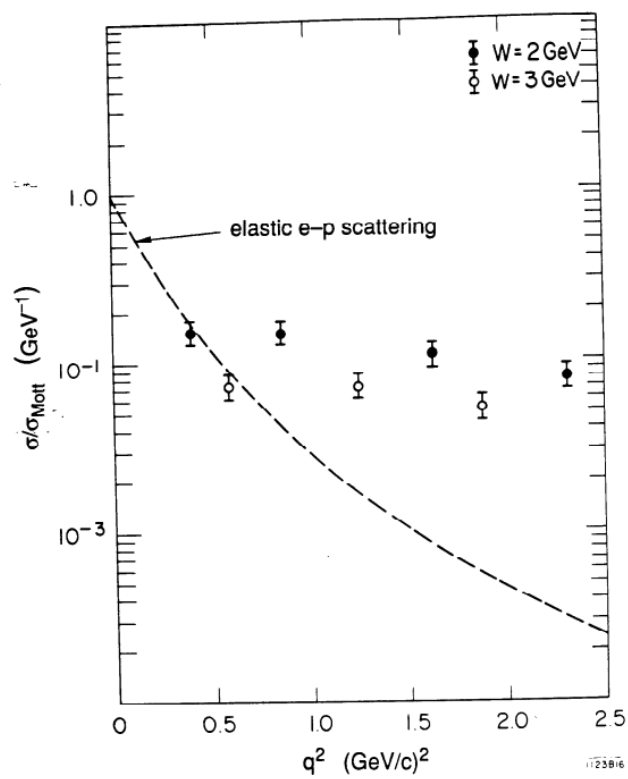

Figure 2.6: The DIS cross section (as a ratio to the Mott cross section) as a function of Q^2 by SLAC-MIT experiment. W means the mass of the recoiled hadrons measured by missing mass in the experiment.

the SLAC-MIT experiment, and this behavior is called "Bjorken scaling".

The physical meaning of the Bjorken scaling becomes clearer by "parton" model proposed by Feynman in the same year, which interpreted the proton as a composite particle that consists of point-like constituents called partons. Then, the proton can be expressed as the collection of partons with the momentum xp where x is the fraction of momentum carried by each parton with respect to the parent's proton momentum p, as shown in Fig. 2.7.

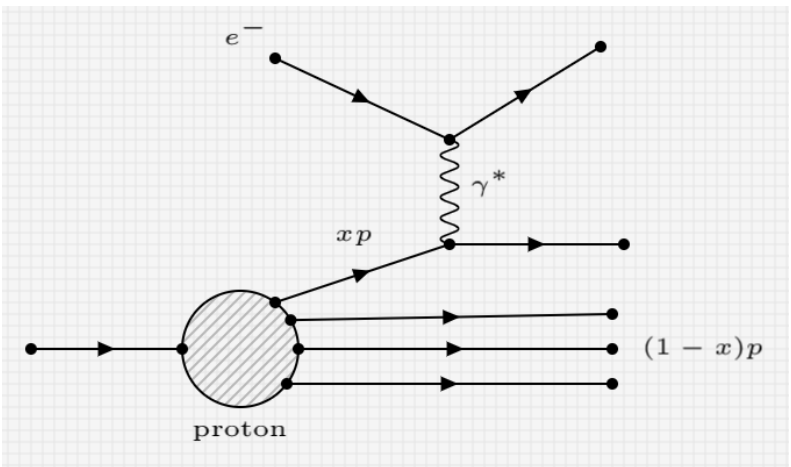

Figure 2.7: DIS interpreted by parton model.

In the parton model, DIS can be interpreted as the scattering between the electron and a point-like particle (parton) with momentum xp. The cross section of electron-parton scattering can easily be obtained by the analogy from the electron-muon scattering cross section after switching the muon mass to the parton mass ($m_\mu \to m_{parton} = xm_p$):

$$\frac{d\sigma}{dE'd\Omega} = \frac{\alpha^2}{4E^2 \sin^4 \frac{\theta}{2}} \left(\cos^2 \frac{\theta}{2} + \frac{Q^2}{2(xm_p)^2} \sin^2 \frac{\theta}{2} \right) \delta \left(\nu - \frac{Q^2}{2xm_p} \right) \tag{2.36}$$

If it is compared to DIS cross section 2.35, the structure functions for electron-parton scattering can be written as below:

$$
\begin{aligned}
2W_1^{parton} &= \frac{Q^2}{2(xm_p)^2}\delta\left(\nu - \frac{Q^2}{2xm_p}\right) \rightarrow m_p W_1^{parton} = \frac{1}{2x\omega}\delta\left(x - 1/\omega\right) \\
W_2^{parton} &= \delta\left(\nu - Q^2/2xm_p\right) \rightarrow \nu W_2^{parton} = x\delta\left(x - 1/\omega\right)
\end{aligned}
\tag{2.37}
$$

$a\delta(x) = \delta(x/a)$ is used to obtain the right formulas.

To obtain the structure function on the proton, (2.37) should be summed over all partons inside of proton. To describe the distribution of partons inside of proton, the parton distribution function (PDF) $f_i(x)$ is introduced such that it means the probability of ith parton carrying the fraction x of the proton momentum. Using PDF, the sum of structure functions over all partons can be expressed like below:

$$
\begin{aligned}
F_1 &\equiv m_p W_1 \\
&= \sum_i \int dx e_i^2 f_i(x) m_p W_1^{parton} \\
&= \sum_i \int dx e_i^2 f_i(x) \frac{1}{2x\omega}\delta\left(x - 1/\omega\right) = \frac{1}{2}\sum_i e_i^2 f_i(x)|_{x=1/\omega} \\
F_2 &\equiv \nu W_2 \\
&= \sum_i \int dx e_i^2 f_i(x) \nu W_2^{parton} \\
&= \sum_i \int dx e_i^2 f_i(x) x\delta\left(x - 1/\omega\right) = \sum_i e_i^2 x f_i(x)|_{x=1/\omega}
\end{aligned}
\tag{2.38}
$$

where e_i^2 is the charge of each parton. In summary, the structure functions were the parton distribution function that only depends on the parton momentum fraction x, which is same with the inverse of ω that Bjorken proposed. The parton model successfully explained the Bjorken scaling.

Interpretation of partons as quarks

After the success of the parton model, the quark, which was previously considered as a pure mathematical tool to build SU(3) representation of hadrons, became one of the strong candidates of the parton. To prove this, a measurement of the ratio of the cross section between electron-proton and electron-neutron scattering was proposed because it can be predicted by the parton-quark model from the constituents of proton (uud) and neutron (udd). As the structure functions depend on the charge of partons e_i^2, the predicted ratio with the quark's fractional charge is unique compared to the other candidates of partons at the time. In terms of parton distribution functions, the structure function of the proton F_2^{ep} and and neutron F_2^{en} can be expressed below:

$$\begin{aligned}
\frac{1}{x}F_2^{ep} &= \left(\frac{2}{3}\right)^2 (u^p(x) + \bar{u}^p(x)) + \left(\frac{1}{3}\right)^2 (d^p(x) + \bar{d}^p(x)) + \left(\frac{1}{3}\right)^2 (s^p(x) + \bar{s}^p(x)) \\
\frac{1}{x}F_2^{en} &= \left(\frac{2}{3}\right)^2 (u^n(x) + \bar{u}^n(x)) + \left(\frac{1}{3}\right)^2 (d^n(x) + \bar{d}^n(x)) + \left(\frac{1}{3}\right)^2 (s^n(x) + \bar{s}^n(x))
\end{aligned} \tag{2.39}$$

where $u^{p(n)}$, $d^{p(n)}$, $s^{p(n)}$ are the PDFs of up, down and strange quark in the proton (neutron). The PDFs for anti-quarks are denoted as $\bar{u}^{p(n)}$, $\bar{d}^{p(n)}$, $\bar{s}^{p(n)}$.

The amount of u in the proton is same with d in the neutron (and also for d). In addition, the amount of s should be same between proton and neutron (as they are sea quarks that come from quark and anti-quark production inside of the nucleon). Therefore, it is convenient to define:

$$
\begin{aligned}
u(x) &\equiv u^p(x) = d^n(x) \\
d(x) &\equiv d^p(x) = u^n(x) \\
s(x) &\equiv s^p(x) = s^n(x)
\end{aligned}
\tag{2.40}
$$

Also, $u(x)$, $d(x)$ and $s(x)$ (and their anti-particles) can be more divided into the contribution from valence quarks (v) and sea quarks (s):

$$
\begin{aligned}
u(x) &= u_v(x) + u_s(x) \\
d(x) &= d_v(x) + d_s(x) \\
S(x) &\equiv u_s(x) = \bar{u}_s(x) = d_s(x) = \bar{d}_s(x) = s_s(x) = \bar{s}_s(x)
\end{aligned}
\tag{2.41}
$$

The last equality is based on the assumption that the probability of the sea quark and its anti-quark production is similar among quark flavors. With the combination of (2.40) and (2.41), F_2^{ep}, F_2^{en} and their ratio is expressed like below:

$$
\begin{aligned}
\frac{1}{x}F_2^{ep} &= \frac{4}{9}u_v + \frac{1}{9}d_v + \frac{4}{3}S \\
\frac{1}{x}F_2^{en} &= \frac{1}{9}u_v + \frac{4}{9}d_v + \frac{4}{3}S \\
\rightarrow F_2^{en}/F_2^{ep} &= \frac{4u_v + d_v + 12S}{u_v + 4d_v + 12S}
\end{aligned}
\tag{2.42}
$$

The behavior of F_2^{en}/F_2^{ep} as a function of x can be inferred by taking a limit $x \to 0$ and $x \to 1$. In $x \to 0$, the quark has very little momentum. Then the sea quarks with little momentum from $q\bar{q}$ pair production dominate over valence quark, which leads $F_2^{en}/F_2^{ep} \to 1$. In the opposite direction, $x \to 1$, the sea quarks are dominated by valence quarks, especially by u_v as the proton has 2 u_v and 1 d_v. It leads the ratio became $F_2^{en}/F_2^{ep} \to \frac{4u_v+d_v}{u_v+4d_v} \sim \frac{1}{4}$.

This predictions is confirmed by the data from SLAC-MIT experiment as seen in Fig.2.8. Therefore, the quark is consistent with the constituent of nucleons, and the study of the proton structure moves to understanding of the parton distribution function in terms of QCD framework, which governs the interaction between quarks and gluons.

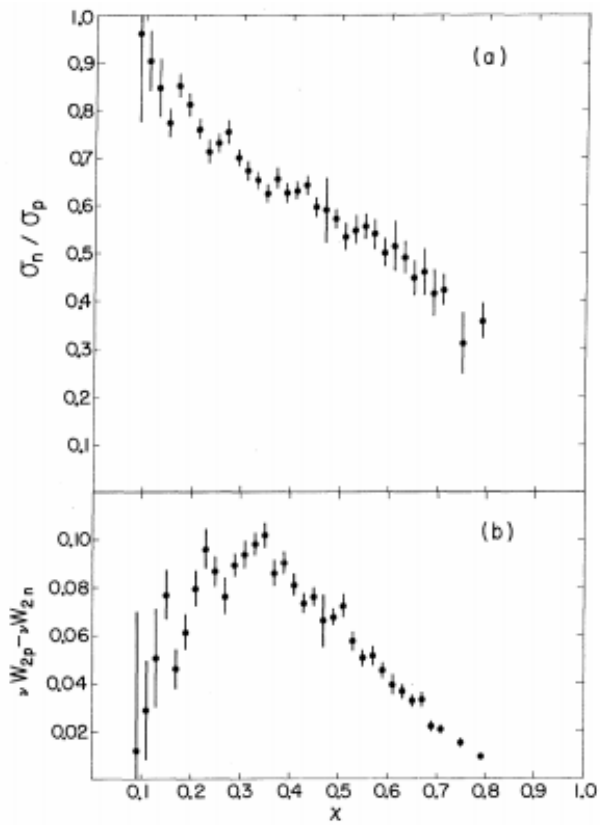

Figure 2.8: The ratio of the cross section between the electron-proton and the electron-neutron scattering as a function of x from the SLAC-MIT experiment [5].

2.2.3 Modern parton distribution functions

In modern PDFs, gluons are considered as partons as well as quarks, which explains the missing momentum of the proton and the scaling violation [6]. Also, heavy quarks (charm and bottom quarks) are also included as one of the constituents of the nucleon depending on the energy scale of the process. This section introduces the strategy of PDF determination and several examples of modern PDFs.

PDF determination by global QCD analyses

The determination of modern PDFs has been performed by extracting PDFs from fitting to multiple experimental data sets, which called "global QCD analysis". The global QCD analysis consists of 1) theoretical bases that provide the mathematical framework of the global fitting and 2) various experimental data that provide the information on the PDFs.

Theoretical base The first theoretical base is the QCD factorization theorem, which allows the total cross section of hard scattering processes can be divided into short and long distance parts. In the case of DIS, the general form of the structure functions can be expressed according to the theorem in QCD framework [7]:

$$F(x, Q^2) = x \int_x^1 \frac{dy}{y} \sum_i C_i \left(\frac{x}{y}, \alpha_s(\mu_R), \mu_F, Q \right) f_i(y, \mu_F) \tag{2.43}$$

where $y = q \cdot P / k \cdot P$ with incoming proton momentum P, C_i is the coefficient functions related to the $q_i + \gamma^* \to X$ partonic cross section, and μ_R and μ_F is the renormalization and factorization scale. According to the expression, clearly the short distance process represented by C_i and the long distance dy-

namics encoded in PDF (f_i) are separated. The important feature is that only C_i is process dependent, and f_i is universal for all processes. This implies that the PDF, which cannot be calculated perturbatively, can be extracted from a global analysis using experimental data with various scattering processes, by combining with predicted partonic cross sections calculated in perturbative way for each process. Therefore, the factorization theorem provides the reason why the global QCD analysis can work for PDF determination.

The other theoretical tool is Dokshitzer–Gribov–Lipatov–Altarelli–Parisi (DGLAP) equation [8, 9, 10, 11], which provides the rule of the evolution of PDF on Q^2 like below [7]:

$$Q^2 \frac{\partial}{\partial Q^2} f_i(x, Q^2) = \sum_i P_{ij}(x, \alpha_s) \otimes f_i(x, Q^2) \tag{2.44}$$

where $P_{ij}(x, Q^2)$ are the Altarelli-Parisi splitting functions, and $\otimes$ means the convolution defined as $f(x) \otimes g(x) = \int_x^1 (dy/y) f(y) g(x/y)$.

It implies that the precise measurement on PDF in a specific Q^2 region can leads the knowledge to the other Q^2 region, which is powerful for PDF determination in various Q^2 range.

Experimental data Various experimental data for PDF determination have been accumulated from the first DIS experiment and the latest studies in Large Hadron Collider (LHC), and Fig. 2.9 shows the example of the list of the data used in NNPDF 3.1, one of modern PDFs widely used, determination [12] in (x, Q^2) plane.

According to the Fig. 2.9, the low x and Q^2 region is mostly covered by collider DIS that came from HERA experiments with lepton-proton collision at $\sqrt{s} =\sim 320\,\mathrm{GeV}$. In the higher x range, fixed target experiments are used to constraint the PDF around $0.1 < x < 1$. For higher Q^2 region that requires

high energy to probe, the contribution comes from collider experiment data including Drell-Yan, transverse momentum of Z boson, $t\bar{t}$ production near $10^3 < Q^2 < 10^5$ range, and the highest Q^2 region is covered by inclusive jet production data.

Example of modern PDFs

There are several PDF fitting groups to provide the state-of-the-art PDFs such as CT [13], NNPDF [12], MMHT [14] and ABM [15]. In this section, CT and NNPDF are introduced as representative modern PDFs.

CT The first CT PDF was presented in 1991 with CTEQ1 PDF [16] by Wu-ki Tung and his collaborators, and the latest version of PDF is CT18 [13] including the latest experimental data from the LHC in their global QCD analysis. The parametrization of the CT PDF at a certain input scale Q_0 is performed using the functional form for parton i below [17]:

$$xf_i(x, Q_0) = x^{a_1}(1-x)^{a_2} P_i(x) \tag{2.45}$$

$(1-x)^{a_2}$ ensures that $f_i \to 0$ in $x \to 1$ elastic limit, and the x^{a_1} is the behavior predicted in Regge theory in $x \to 0$ limit. $P_i(x)$ is the interpolating function that represents the smoothly varying behavior of PDF on x between $x \to 0$ and $x \to 1$ regions. Since CT14 [17], the chosen $P_i(x)$ is the Bernstein polynomials. For example, $P_i(x)$ for valance up quark is expressed as a linear combination of 0-4th order polynomial:

$$P_{u_v} = d_0 p_0(y) + d_1 p_1(y) + d_2 p_2(y) + d_3 p_3(y) + d_4 p_4(y) \tag{2.46}$$

where $y = \sqrt{x}$ and $p_i(y)$ is i-th order Bernstein polynomial. Expression in terms of y and $p_i(y)$ leads to slower variations on x and smaller correlation

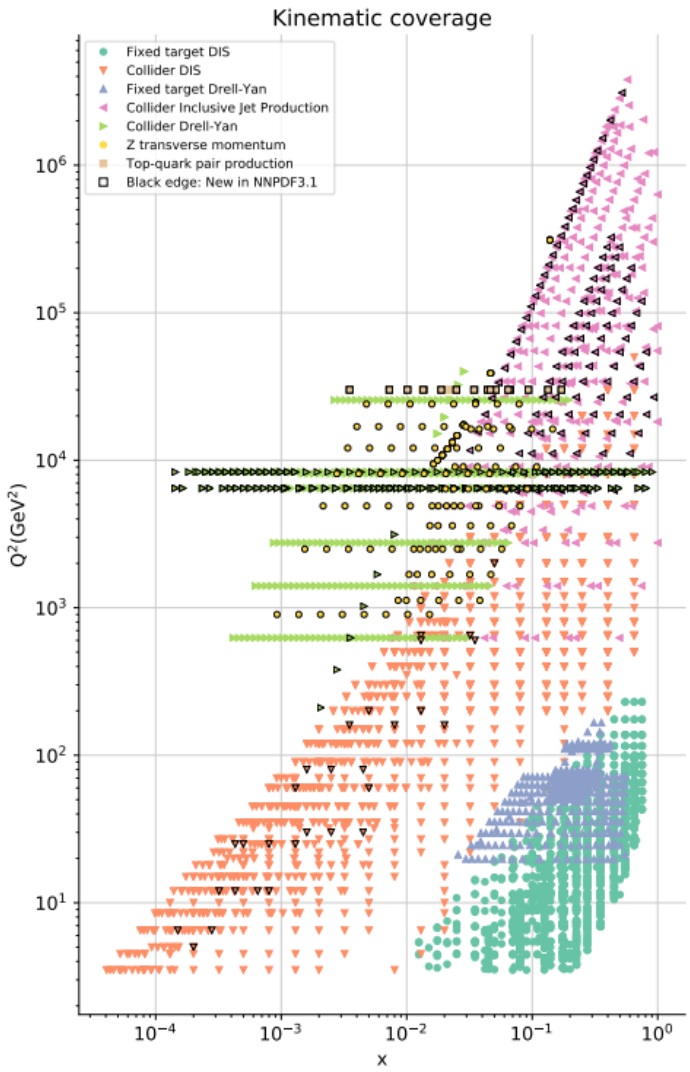

Figure 2.9: List of the experimental data in (x, Q^2) plane used in global QCD analysis for NNPDF 3.1 [12].

between coefficients compared to the nominal polynomial with x.

Once the PDF is determined at the scale Q_0, the PDF at any scale Q can be determined via DGLAP evolution equation. The example parton distribution functions from CT18 in two different Q values are shown in Fig. 2.10.

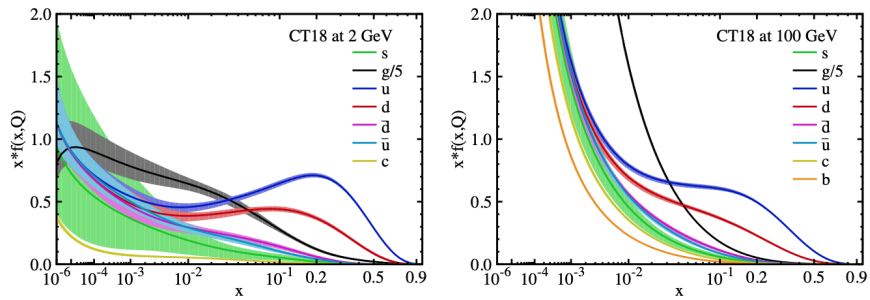

Figure 2.10: The CT18 parton distribution function in $Q = 2\,\text{GeV}$ (left) and $Q = 100\,\text{GeV}$ (right) for each parton [13].

NNPDF The first paper with NNPDF methodology was appeared in 2002 to determine DIS structure functions based on several fixed target data [18], and the methodology was extended to direct determination of PDF up to NNPDF 3.1 [12] where the latest LHC experimental data are included.

The initial stage of the parametrization for the PDF determination is same with the other PDFs. The parametrization is started at a specific scale $Q_0 \sim 1\,\text{GeV}$. However, instead of assuming a simple functional form of PDF, NNPDF uses the neural network technique for PDF determination. Even though this approach requires many experimental data to produce reliable results, it allows to avoid possible theoretical bias which could be introduced in the assumption of PDF form. The disadvantage is also getting smaller as more experimental data is accumulated especially from various LHC data analyses.

The example of various parton's distribution functions from NNPDF 3.1

with different scales are shown in Fig. 2.11.

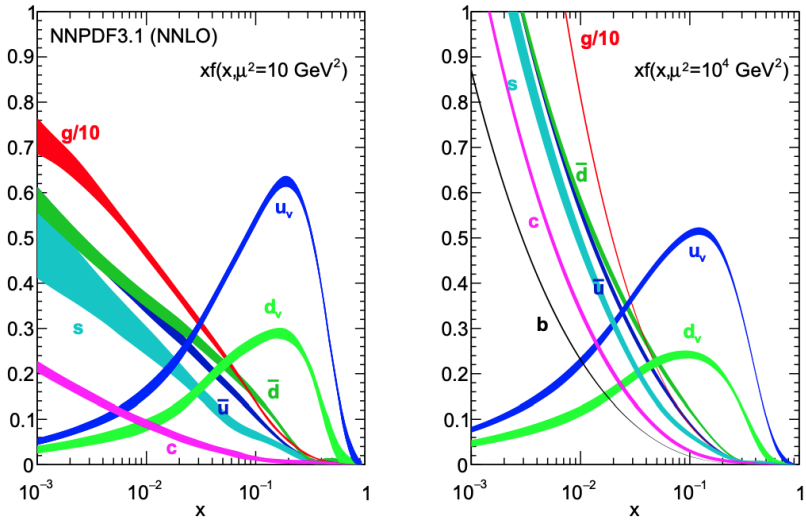

Figure 2.11: The NNPDF 3.1 parton distribution function in $\mu^2 = Q^2 = 10\,\text{GeV}$ (left) and $Q^2 = 10^4\,\text{GeV}$ (right) [12].

2.3 Drell-Yan process

Drell-Yan (DY) process is the process with two leptons in the final state via Z/γ^* exchange from the annihilation of quark and anti-quark at hadron-hardon collisions as shown in Fig. 2.12.

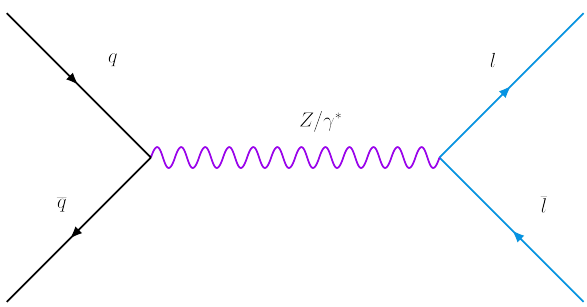

Figure 2.12: The Feynman diagram of the Drell-Yan process at Leading order.

The process was suggested for the first time by Sidney D. Drell and Tung-Mow Yan [19], and the first observation of muon pairs from DY process (in $1 < m_{\mu\mu} < 6.7\,\text{GeV}$ was reported in 1970 at Brookhaven National Laboratory by the experiment colliding protons to fixed uranium targets [20].

The DY process has been widely and extensively studied in high energy physics field for precise tests of QCD and studies for the structure of the proton (PDF).

2.3.1 Drell-Yan cross section

According to the factorization theorem (described in Sec. 2.2.3), the Drell-Yan cross section in proton-proton collision can be expressed in terms of partonic cross sections, which can be calculated in perturbative way, and the PDFs of two colliding protons [7]:

$$\frac{d^2\sigma}{dydQ^2}(y,Q^2,\mu_R^2,\mu_F^2)=\sum_{a,b=q,\bar{q},g}\int_{\tau_1}^1 dx_1 f_a(x_1,\mu_F^2)\int_{\tau_2}^1 dx_2 f_b(x_2,\mu_F^2)\frac{d^2\hat{\sigma_{ab}}}{dydQ^2}(x_1,x_2,y,Q^2,\mu_R^2,\mu_F^2) \tag{2.47}$$

where y and Q^2 are the rapidity and the invariant mass of the dilepton system, and $\tau_{1,2} = \sqrt{\frac{Q^2}{s}}e^{\pm y}$ with the center of mass energy s.

In principle, the physical cross section $d^2\sigma/dydQ^2$ should not depend on the choice of the factorization scale μ_F, but the dependence can appear at a fixed order cross section due to missing higher order effects. To have better convergence at each order and minimize the dependence of the cross section on μ_F, μ_F is conventionally chosen to be Q^2.

Partonic cross section at leading order

The process via γ^* exchange only The cross section of DY process mediated by γ^* only $\sigma(q\bar{q} \to \gamma^* \to \ell^-\ell^+)$ can be easily obtained from the pure

QED cross section of $e^-e^+ \to \mu^-\mu^+$ reaction:

$$\sigma(e^-e^+ \to \mu^-\mu^+) = \frac{4\pi\alpha^2}{3s} \tag{2.48}$$

where α is the electroweak coupling constant, and s is one of the Mandelstam variables defined as $s = (p_1 + p_2)^2$ with the 4-momentum vector of two incoming particles $p_{1,2}$.

To obtain $\sigma(q\bar{q} \to \gamma^* \to \ell^-\ell^+)$, electrons should be switched to quarks. It modifies the cross section $\sigma(e^-e^+ \to \mu^-\mu^+)$ to take into account the electric charge of quarks Q_q, and the average over possible color states in the initial states:

$$\sigma(q\bar{q} \to \ell^-\ell^+) = (\frac{1}{3})(\frac{1}{3})3\sigma(e^-e^+ \to \mu^-\mu^+)Q_q^2 = \frac{4\pi\alpha^2}{9\hat{s}}Q_q^2 \tag{2.49}$$

The first two $\frac{1}{3}$ factors mean the average of (R,G,B) color states for q and $\bar{q}$, and 3 means the sum of color combination R$\bar{\text{R}}$, G$\bar{\text{G}}$ and B$\bar{\text{B}}$. The s is also switched to $\hat{s}$ to distinguish it from the center of mass energy in proton-proton collision $\sqrt{s}$ in DY process.

The process with γ^* and Z exchange To obtain the full cross section of the DY partonic process, the contribution from Z and the interference between γ^* and Z should be taken into account.

If the transition amplitude of γ^* and Z contribution (denoted as M_{γ^*} and M_Z respectively) is constructed using the Feynman rule and calculated the square of the sum of amplitude, i.e:

$$|M_{\gamma^*/Z}|^2 = |M_{\gamma^*} + M_Z|^2 = |M_{\gamma^*}|^2 + |M_Z|^2 + 2Re\,(M_{\gamma^*}M_Z^*) \tag{2.50}$$

The total cross section can be obtained from the amplitude below:

$$\sigma(q\bar{q} \to \ell^-\ell^+) = \frac{4\pi\alpha^2}{9\hat{s}} \left(Q_q^2 - 2Q_q c_{v,q} c_{v,\ell} f_1(\hat{s}) + (c_{v,q}^2 + c_{a,q}^2)(c_{v,\ell}^2 + c_{a,\ell}^2) f_2(\hat{s})\right) \tag{2.51}$$

Here, $c_{v,q(\ell)}$ and $c_{a,q(\ell)}$ mean the vector and axial vector couplings for quarks (leptons), which are defined as

$$\begin{aligned} c_{v,f} &= T_f^3 - 2s_w Q_f \\ c_{a,f} &= T_f^3 \end{aligned} \tag{2.52}$$

with the 3rd component of weak isospin T^3 and the electroweak mixing angle $s_w = \sin\theta_w$. The value of couplings are listed in Table 2.3.

Fermion (f)	Q_f	$C_{a,f} = T_f^3$	$c_{v,f}$
ℓ	-1	-1/2	-1/2 + 2 s_w
u,c,b	2/3	1/2	1/2 - 4/3 s_w
d,s,t	-1/3	-1/2	-1/2 + 2/3 s_w

Table 2.3: Vector and axial vector couplings appeared in partonic DY cross section.

The $f_1(\hat{s})$ and $f_2(\hat{s})$ in 2.51 are given as

$$\begin{aligned} f_1(\hat{s}) &= Re\left(f(\hat{s})\right) = \frac{1}{16c_w^2 s_w^2} \frac{\hat{s}(\hat{s} - M_Z^2)}{(\hat{s} - M_Z^2)^2 + \Gamma_Z^2 M_Z^2} \\ f_2(\hat{s}) &= |f(\hat{s})|^2 = \left(\frac{1}{16c_w^2 s_w^2}\right)^2 \frac{\hat{s}^2}{(\hat{s} - M_Z^2)^2 + \Gamma_Z^2 M_Z^2} \\ &\left(f(\hat{s}) = \frac{1}{16c_w^2 s_w^2} \frac{\hat{s}}{\hat{s} - M_Z^2 + i\Gamma_Z M_Z}\right) \end{aligned} \tag{2.53}$$

with $c_w = \cos\theta_w$ and the mass (width) of Z boson M_Z (Γ_Z).

According to 2.51, the first term obviously comes from γ^* contribution as the form is same with 2.49. The contribution dominates outside of the Z peak region. The last term represents the process with Z exchange by Breit-Wigner from with the peak at M_Z. Finally, the second term represents the interference between Z and γ^*, which vanish as $\hat{s} \to M_Z$. But the contribution becomes larger near the tail of the Breit-Wigner distribution of the Z resonance. At the $\hat{s} \to$ inf limit, the total cross section is proportional to $1/s$, which shows a smoothly falling shape in the high mass region.

2.3.2 Motivation of the DY cross section measurement

The cross section of the DY process has been extensively studied and measured through the history of the particle physics due to much information that can be derived from it including understanding of the perturbative QCD, the structure of the proton, and indirect influence to the search for new physics beyond the standard model. This section introduces the motivation of the measurement of the DY cross section.

Precise test of the perturbative QCD

To enable the precise test of the perturbative QCD, the two conditions should be satisfied: higher precision of the theoretical prediction and the experimental data. The DY cross section measurement is one of the best example to meet the two conditions.

In the theoretical point of view, the cross sections of the DY process are already well understood up to NNLO in QCD, thanks to the simple topology of the process compared to the other processes associated with many interactions or particles. The first paper with the cross section up to $\mathcal{O}(\alpha_s^2)$ order was published in 1991 [21], and the NNLO prediction on the differential cross sec-

tions started to appear in early 2000s [22, 23]. The studies on the higher order electroweak corrections were also followed. As a result of such studies, several public computation programs up to NNLO were made with the functionality to define user-defined requirements on the final state leptons and have been widely used for research including FEWZ [24], DYNNLO [25], and so on. The theoretical efforts for higher order corrections are still ongoing, and the N^{3}LO cross section was recently presented [26] which shows lower scale uncertainty than the the lower order, as seen in Fig. 2.13.

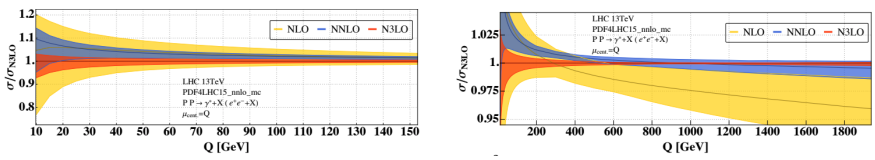

Figure 2.13: The theoretical prediction on the cross section of the DY process as a function of dilepton mass Q with NLO (yellow), NNLO (blue) and N^{3}LO (red) order in QCD. The bands on each prediction is the uncertainty from the dependence on the choice of renormalization and factorization scales.

On the other hand, in the experimental point of view, the DY cross sections are usually measured by using two leptons (electrons and muons) which is easier to obtain high efficiency and resolutions compared to the complicated objects in the collider experiments like jets and missing transverse energy. Also, thanks to higher cross section of DY process than the other processes that produce leptons, the signal yield is sufficient and the result is not limited by statistical uncertainty except for extremely high dilepton mass region over $\mathcal{O}(1\,\mathrm{TeV})$. Therefore, the achievable experimental precision is already below 10% in most of the dilepton mass range, and especially it goes down to about 1% near Z peak region [27].

Due to its high precision of theoretical prediction and experimental mea-

surements, the measurement is also used as one of the "standard candles" to study the detector performance or commissioning, including the lepton efficiency measurement and detector calibrations [28].

With the combined effort to achieve high precision from both theoretical and experimental data, the validity of the perturbative QCD can be extensively tested via DY process by comparing them.

PDF constraints

One of the most important contributions of the measurement is the PDF constraints as the ingredient of the global QCD analyses for PDF determination. In particular, in the case of the cross section near Z peak region, the form of the cross section can be inferred from 2.47 and 2.51:

$$\begin{aligned}\sigma_Z \sim & \left(c_{v,u}^2 + c_{a,u}^2\right)\left[u(x_1)\bar{u}(x_2) + c(x_1)\bar{c}(x_2)\right] \\ & + \left(c_{v,d}^2 + c_{a,d}^2\right)\left[d(x_1)\bar{d}(x_2) + s(x_1)\bar{s}(x_2) + b(x_1)\bar{b}(x_2)\right] + 1 \leftrightarrow 2\end{aligned} \tag{2.54}$$

where x_1 and x_2 means the momentum fraction carried by each parton with respect to the momentum of the two colliding protons. As seen, the contribution of up-type quarks and down-type quarks are different due to the different vector and axial-vector couplings to Z as summarized in Table 2.3. According to 2.54, the precise measurement of the Z production cross section can contribute to the PDF determination for heavy quarks in the x region where the light quarks are sufficiently determined.

In the measurement for the low dilepton mass region, the DY process is dominated by γ^* exchange. The form of the cross section will be like below:

$$\sigma_{\text{lowmass}} \sim \sum_q Q_q^2 \left(q_(x_1)\bar{q}(x_2) + q_(x_2)\bar{q}(x_1)\right) \tag{2.55}$$

The coefficients to each quark flavor is different with Z exchange case in 2.54 and only depends on the electric charge Q_q^2. From the difference of the coefficients, the cross section measurement in the low mass region could give complementary constraint power to the quark flavor composition, especially in the low and intermediate x region. In addition, the low mass measurement with the minimum requirement on the transverse momentum of the leptons in the final state leads larger fraction of DY events with non-zero dilepton transverse momentum, which enables to indirectly probe the DY process with higher order effect in QCD. Therefore, The cross section with the requirement can also contribute to the determination of gluon PDF in low x region as the DY process can happen via gluon-quark scattering in higher order.

Lastly, the measurement in the high mass region above Z peak can probe the quark and anti-quark PDFs in high-x region, which is rather less constrained especially for anti-quark PDFs.

Importance as a main background in searches for new physics

Precisely measured DY cross section can also benefit to the search for new physics beyond the standard model. The lepton channel has been used as one of popular channels for new physics search because the lepton can be detected with high efficiency and resolution, which leads higher chance to find clean signature of the new physics.

In the analysis with the lepton final state, the DY process is one of the main backgrounds due to its large cross section compared to the other processes that produces leptons, as seen in Fig. 2.14.

The representative example of the analyses with DY background is the search for new neutral guage boson Z' decaying into two leptons. As seen in Fig. 2.15, which is the dilepton mass distribution from LHC [29], the dominant

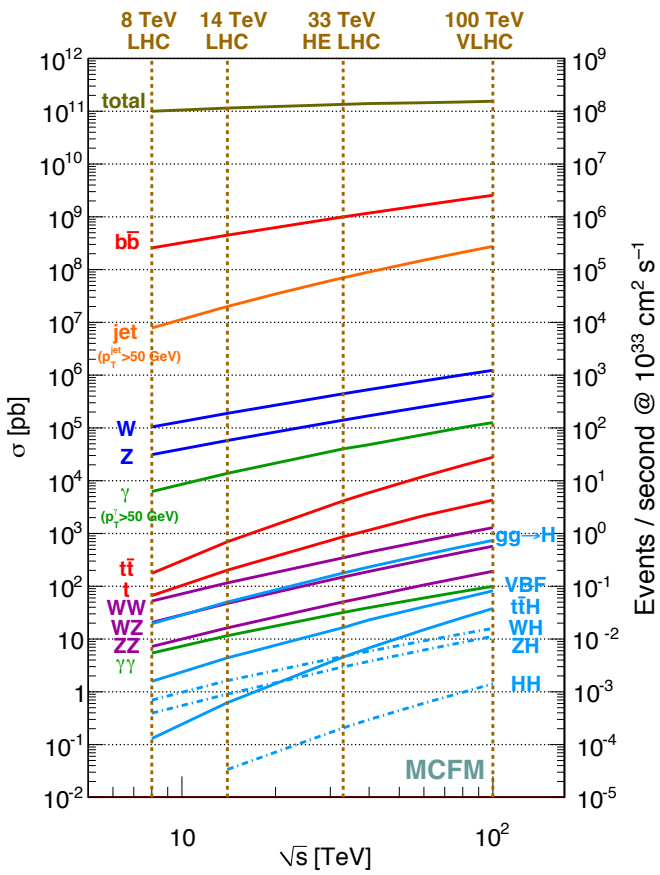

Figure 2.14: The inclusive cross sections of selected processes as a function of the center of mass energy at hardron colliders, calculated by MCFM.

background is the DY process. Therefore, the precise understanding of the differential DY cross section with various observables that can be used for new physics search (as well as the inclusive one) is quite important to increase the sensitivity of the new physics search.

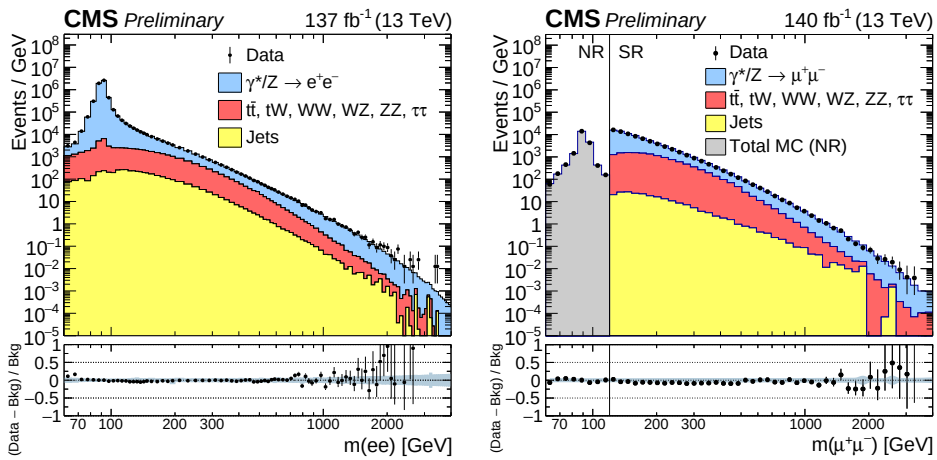

Figure 2.15: The dilepton mass distribution for dielectron (left) and dimuon channel (right) from the $Z' \to \ell\ell$ search with LHC full Run2 data [29].

Chapter 3

Experimental apparatus

In this chapter, the experimental setups used to collect the proton-proton collision data for the analysis is described. The accelerator complex is briefly introduced, and description on the particle detector will be followed with the details on its subsystems.

3.1 Large Hadron Collider

The Large hadron collider (LHC) is the most largest and powerful circular particle accelerator with 26.7 km circumference located underground near Geneva across the border of Switzerland and France, associated with the European Organization for Nuclear Research (CERN) [30]. It is designed to operate with the center of mass energy $\sqrt{s} = 14\,\text{TeV}$ with the instantaneous luminosity near $10^{34}\text{cm}^{-2}\text{s}^{-1}$ for proton-proton collisions. In the real condition, it was operated with $\sqrt{s} = 13\,\text{TeV}$ and $\sim 2 \times 10^{34}\text{cm}^{-2}\text{s}^{-1}$ peak instantaneous luminosity at the latest performance in the Run 2 finished in 2018. The machine can also perform the other type of collisions using heavy ions including ion-ion

collision proton-ion collisions. The Lead nuclei is used for the heavy ion experiments. The total accelerator complex including various intermediate particle accelerators as well as LHC is shown in Fig. 3.1

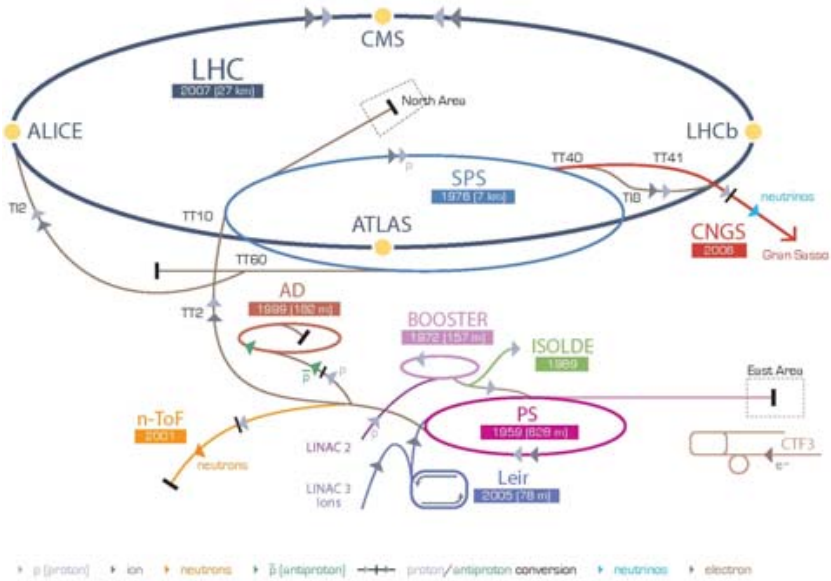

Figure 3.1: The LHC complex [31].

3.1.1 Proton acceleration

The proton source is the nuclei of hydrogen gas by removing the electrons via an electric field. The first acceleration is performed in the linear accelerator LINAC2 (supposed to be succeeded by LINAC4 in 2020) up to the energy of 50 MeV. As a next step, the protons are injected in Proton Synchrotron Booster (PSB) and the energy of electron increases to 1.4 GeV. The next injection is to Super Proton Synchrotron (SPS), which was used in proton-antiproton collider and famous for the discovery of W and Z bosons. The SPS accelerates the proton up to the energy of 450 GeV and inject to LHC ring. The protons are accelerated by a strong magnetic field produced by superconducting magnets

in LHC operated via liquid Helium with about 3K temperature. After about 20 minutes from the injection of the beam from SPS, the proton beam finally reaches to 6.5 TeV and is ready to collisions.

3.1.2 Luminosity

The instantaneous luminosity ($\mathcal{L}$) represents the number of collisions in the collider per a unit area (cm^2) and second so that the number of events per seconds for a given physics process is expressed like below:

$$\frac{dN_{event}}{dt} = \mathcal{L} \times \sigma_{\text{process}} \tag{3.1}$$

where σ_{process} is the cross section of the process. Therefore, it is a measure of how many data can be produced by the machine and considered as one of the important parameter of the particle collider.

The luminosity of the machine is determined by the formula [30]:

$$\mathcal{L} = \frac{N_b^2 n_b f_{\text{rev}} \gamma_{\text{r}}}{4\pi\epsilon_n \beta^*} F \tag{3.2}$$

The numerator is related to the number of collisions. N_b is the number of particles per bunch, and n_b is the number of bunches in each beam. f_{rev} is the revolution frequency determined by the speed of the proton and the circumference, and γ_{r} is the relativistic Lorentz vector.

In the denominator, the parameters are related to the beam characteristic. ϵ_n is the normalized transverse emittance that describes the average of spread of the particle in position-momentum phase space. The lower emittance means that the beam is confined in a small area with similar momentum, which leads to higher luminosity. β^* is the beta function at the interaction point (IP), which is the distance from IP to the point where the width of the beam becomes twice with respect to the width at IP. Therefore, lower β^* beam has more squeezed

and focused shape and it also contributes to the higher luminosity. The last parameter F is the geometric luminosity reduction factor coming from the crossing angle at the IP.

The detail numbers for each parameter is listed in the Fig. 3.2.

Parameter	Design	2012	2016	2017	2018
beam energy [TeV]	7	4	6.5	6.5	6.5
bunch spacing [ns]	25	50	25	25	25
β^* CMS/ATLAS [cm]	55	60	40	40 / 30	30 - 25
crossing angle [μrad]	285	290	370 / 280	300 - 240	320 - 260
bunch population N [10^{11} ppb]	1.15	1.65	1.1	1.15	1.15
normalized emittance ε [μm]	3.75	2.5	2.2	2.2	2.0
number of bunches per ring k	2808	1374	2220	2556	2556
peak luminosity L [10^{34} cm^{-2}s^{-1}]	1	0.75	1.4	2.05	2.01
peak average event pile-up μ	~ 20	~ 35	~ 50	~ 55	~ 60
peak stored energy [MJ]	360	145	270	320	340

Figure 3.2: List of LHC parameters in the operation from 2012 to 2018 compared to its design [32].

3.1.3 Particle detectors at the LHC

The LHC has 4 collision points across the ring, and each points are occupied by particle detectors as seen in Fig. 3.3 with different purpose and design. THe brief introduction to each detector is below:

- CMS (Compact Muon Solenoid): The general purpose particle detector featured by a compact size due to large magnetic field (3.8 T) from the huge solenoid. Its physics program has a wide range from the standard model physics (including the discovery of Higgs boson) and the new physics beyond standard model (BSM) including supersymmetry and dark metter. The details will be followed in the section 3.2.

- ATLAS (A Toroidal LHC Apparatus): Similar to CMS, it is also the multi-purpose particle detector at Point 1 but has different design.

- ALICE (A Large Ion Collider Experiment): The particle detector specialized to the heavy-ion experiments. The main physics process studied is the quark-gluon plasma, which is similar to the state at the beginning of the universe. It provides the unique opportunity to the deep understanding of the strong interaction.

- LHCb (Large Hadron Collider beauty): Another specialized detector to study bottom quark focused in the forward region. The study aims to understand one of the open question in the SM, the matter-antimatter asymmetry.

3.1.4 Data taking

The first beam in LHC was circulated in 2008, and the operation starts from 2010 with the beam energy of 3.5 TeV ($\sqrt{s} = 7\,\text{TeV}$) after fixing a problem in the superconducting magnet found in 2008. After accumulating about 6 fb^{-1} data with $\sqrt{s} = 7\,\text{TeV}$ up to 2011, the center of mass energy increased to 8 TeV in 2012 and collected about 23 fb^{-1}. It is the Run 1 of LHC. The Run 2 starts with about twice higher center of mass energy than before, 13 TeV, in 2015 after long shutdown 1 (LS1). From 2015 to 2018, the total integrated luminosity is close to 140 fb^{-1}, which is about 7 times larger amount of the data than Run 1. The integrated luminosity per each year is summarized in the Fig. 3.4. From 2019, LHC starts another long shutdown (LS2) to prepare for Run 3 and High-luminosity LHC.

3.2 Compact Muon Solenoid detector

The CMS detector is the multi-purpose particle detector to cover a wide range of physics program from SM to search for new BSM physics. The location is

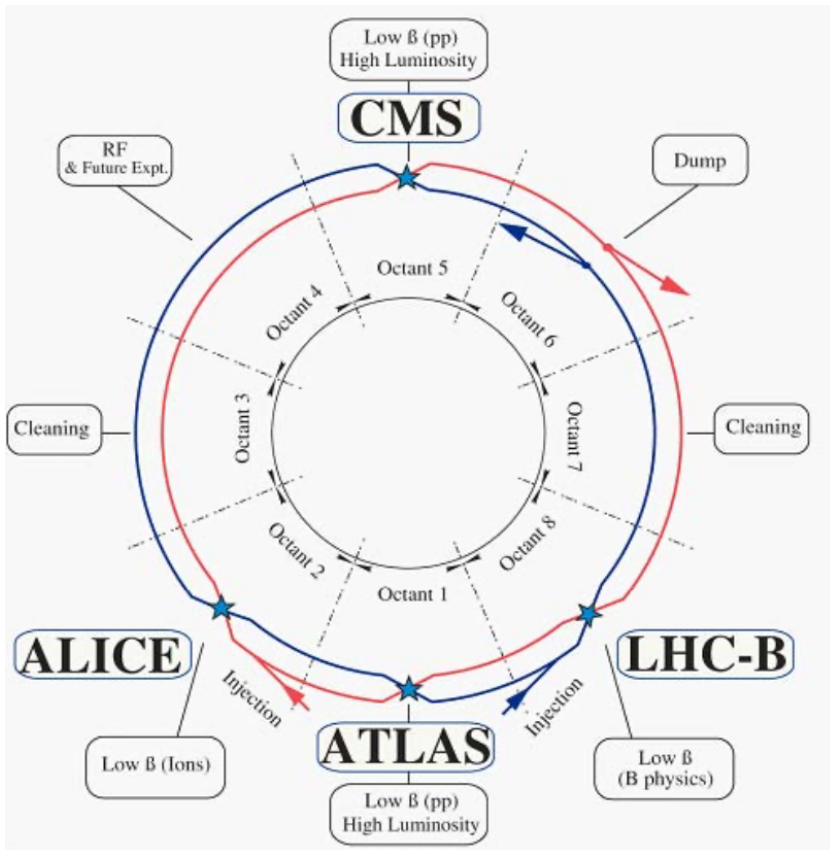

Figure 3.3: The layout of LHC with the experiments located at each collision points [30].

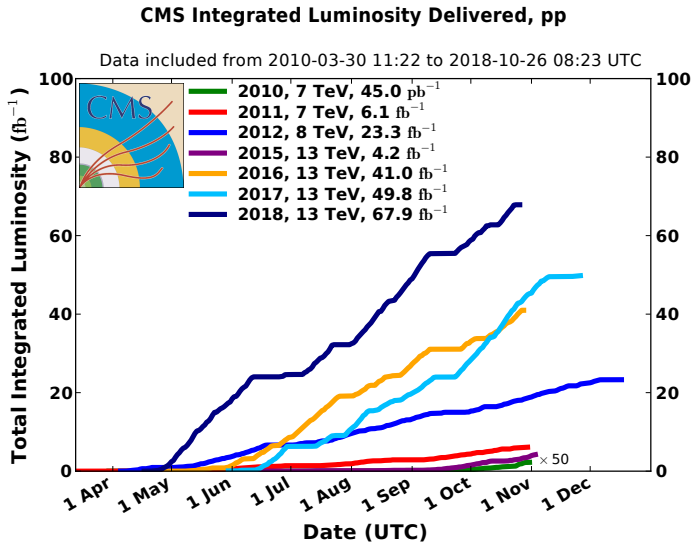

Figure 3.4: The integrated luminosity delivered to CMS by LHC since the operation in 2010.

one of the interaction point in LHC called Point55, underground cavern near Cessy. The detector is overall 28.7 m long and has 15 m diameter with the weights of about 14,000 t. The overall structure can be seen in Fig. 3.5.

The central feature of the detector is a huge superconducting solenoid generating a 3.8 T magnetic field. Inside the solenoid, a silicon pixel and strip detector are placed at the innermost part of the detector near the interaction point. A electromagnetic calorimeter composed of lead tungstate crystals and a brass and scintillator hadron calorimeter are followed. Muon detector embedded in the steel flux-return yoke is placed in the outside of the solenoid, and it is composed of gas-ionization chambers made with various type of techniques. Details on each subdetector is described in the later sections.

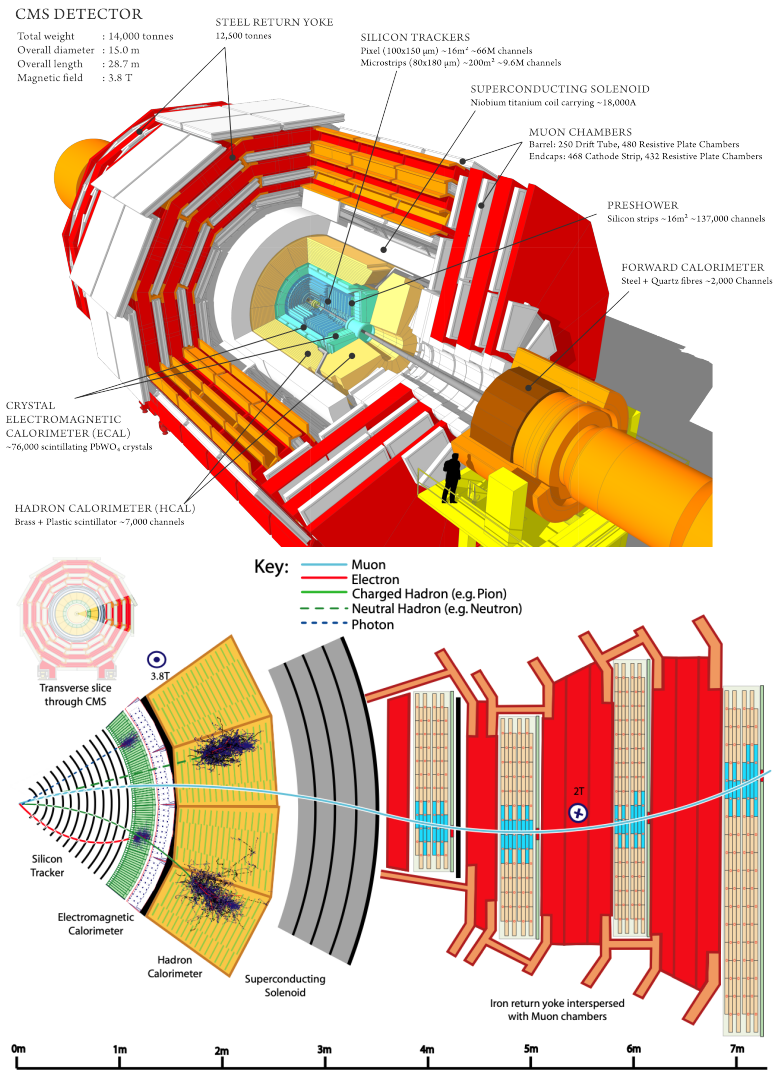

Figure 3.5: The overview (top) and transverse slice (bottom) of the CMS detector.

3.2.1 Coordinate system

The CMS uses the coordinate system shown in Fig. 3.6 to describe the structure of the detector and the particle trajectories. The origin of the system is placed at the interaction point. The direction of x-axis towards the center of the LHC ring, and y-axis points upward. The z-axis, which is decided by x and y axis as it is the right-handed Cartesian coordinate system, points to the counterclockwise direction of the beam.

As the detector has a cylindrical shape, it is convenient to adopt the polar coordinate system. The azimuthal angle ϕ is defined as the angle in (x,y) plane from x-axis. The polar angle θ is measured from z-axis in (r,z) plane and usually expressed in pseudorapidity $\eta = -\ln\tan(\theta/2)$.

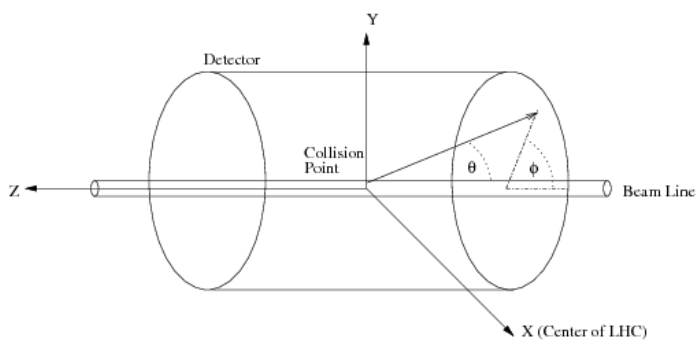

Figure 3.6: CMS Coordinate system [33].

3.2.2 Inner tracking system

The inner tracker is the subdetector located closest to the interaction point with 5.8 m length and 2.5 m diameter, made with silicon pixel and strips. The purpose of the tracker is to precisely measure the trajectory of charged particles with high efficiency, as well as the precise reconstruction of vertices including primary vertices from hard scattering interaction and secondary vertices from

the decay of long-lived particles.

To achieve the goal, it is required to have high granularity and fast response to identify each particle track in multiple proton-proton scattering in a bunch crossing (pileup) with 25ns bunch crossing interval. Also, in order to minimize the interaction of the particles with the materials, it is designed to have minimum amount of materials while it has enough electronics for an efficient cooling system. Finally, as the detector is quite close to the interaction point, the hardness on the radiation damage for a long period is essential for stable operation. To meet the above requirement, the silicon detector is chosen as the ingredient of the tracker.

The tracker system consists of two parts as seen in Fig. 3.7.

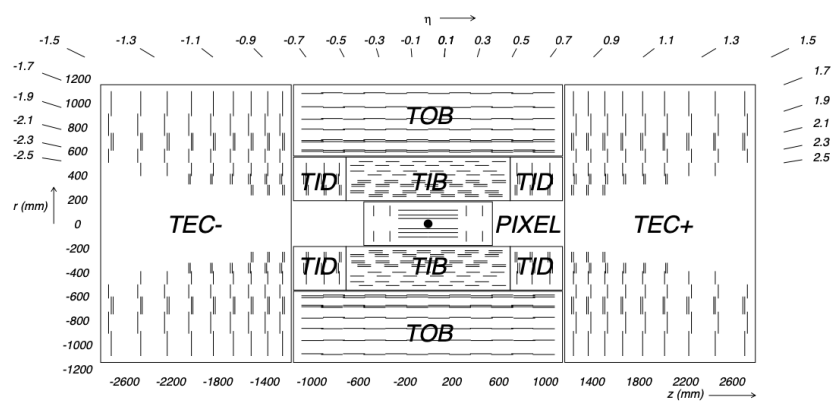

Figure 3.7: The structure of inner tracker in (r,z) plane [34].

Pixel detector

The innermost one is the pixel detector made of silicon pixels with the size of $100 \times 150\,\mu$m. The pixels form three barrel layers (BPix) and two forward disks in endcap (FPix), and each of them are composed of 48 million and 18 million pixels respectively. The three BPix detectors are placed at the radii of 4.4,

7.3 and 10.2 cm. The Two FPix disks are located in z=±34.5 and z=±46.5 cm with varying radius from 6 to 15 cm.

Before 2017 data taking, the pixel detector was upgraded to maintain the high performance at the current and future LHC condition with $\mathcal{L} = 2.0 \times 10^{34}$ cm^{-2} s^{-1} and pileup over 50, which is higher than the expectation aimed by the design of the legacy pixel tracker. The comparison of the new pixel detector with the legacy system is shown in Fig. 3.8. The number of barrel layers increased from 3 to 4, and the innermost layers is closer to the interaction points. In parallel, one more endcap disk is added, and the occupation by materials is also reduced compared to the legacy system.

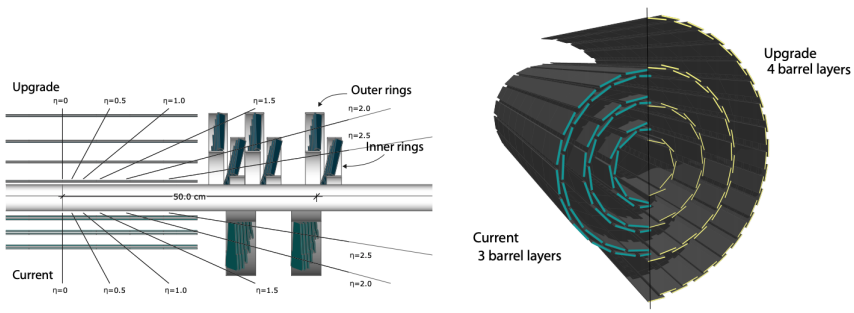

Figure 3.8: The upgraded pixel detector in 2017 [35].

Strip detector

Outside of the pixel detector with the radius from 20 to 116 cm is surrounded by the strip detector made of silicon strip sensors with total 15,148 detector modules corresponding to 9.3 million strips. The strip detector is divided into three subsystems. The Tracker Inner barrel and disks (TIB/TID) with 4 barrel layers and 3 disks cover inner part of the strip detector up to radius of 55 cm. The TIB and TID are surrounded by the tracker outer barrel (TOB) composed of 6 layers with outer radius of 116 cm. Finally, the tracker outer endcaps

(TEC) with 9 disks cover the z range where the other subsystem does not reach, i.e. 124 cm $< |z| <$ 282 cm. Each subsystem delivers different number and kind of measurements on the trajectory depending on its geometry and the number of layers.

Performance

Regarding the performance of the detector, the momentum resolution for single muons with high transverse momentum (p_T) around 100 GeV is 1–2% depending on the η region. The resolution for the transverse and longitudinal impact parameter is about 10 μm and 20–40 μm respectively. The resolution is degraded for a low momentum particle due to the effect from multi scattering. In terms of the efficiency, single muons are detected with $\sim$99% efficiency with p_T above 10 GeV in $|\eta| <\sim$ 2.0 region. In higher $|\eta|$ region, the efficiency starts to drop due to the limited coverage of the forward pixel detector.

3.2.3 Electromagnetic calorimeter

The electromagnetic calorimeter (ECAL) provides the measurement of the electromagnetic object like electrons and photons. This is the homogeneous calorimeter made of lead tungstate ($PbWO_4$) crystals, which have many good characteristics suitable for LHC environment. Thanks to its high density (8.28 g/cm^3) and short radiation length (X_0) (0.89 cm) as well as its good hardness on the radiation damage, the high granularity detector can be made with a compact size. Also, the emission of the scintillation light is fast as about 80% of the light is emitted within 25 ns, which satisfies the requirement on the fast response due to short bunch crossing in LHC. The disadvantage of the crystal, which is the relatively low light output, is compensated by amplifying it using the photodetectors.

Structure

The overall structure of the ECAL is illustrated in Fig. 3.9. The central barrel part covers the pseudorapidity range $|\eta| < 1.479$. It is made of 61,200 crystals that has the area of $22 \times 22\, mm^2$ for the front face and 23 cm long corresponding to $25.8 X_0$. The scintillation lights are collected and amplified by Avalanche photodiodes as the photodetectors.

The endcap detector, which covers $1.479 < |\eta| < 3.0$, is made of 7324 crystals for each two endcaps. The crystal has $28.62 \times 28.62\, mm^2$ area for the front face and the length of 220 mm ($24.7 X_0$). The photodetectors for the endcap is vacuum phototriodes.

ECAL has another subsystem in front of the endcap detector called preshower detector that covers $1.653 < |\eta| < 2.6$. The goal of the detector is to distinguish single photon from two merged photons from decays of neutral pion $\pi^0 \to \gamma\gamma$ in high η region via finer granularity than the ECAL. The first layer generates the electromagnetic shower of incoming particles, and the silicon sensors in the second layer measure the deposit energy and the shower profile.

As the number of emitted photon in the crystal and the performance of photodetector depends on the temperature, it is important to keep the same temperature during the operation. The cooling system in ECAL uses water flow to extract heats in electronics and stays in 18°C within ±0.05°C.

Performance

The resolution of the calorimeter is determined by the formula below [34]:

$$(\sigma/E)^2 = \left(S/\sqrt{E}\right)^2 + (N/E)^2 + C^2 \tag{3.3}$$

S is the stochastic term, which represents the contribution from the fluctuation event by event or photostatistics. N is the noise term, which contains the

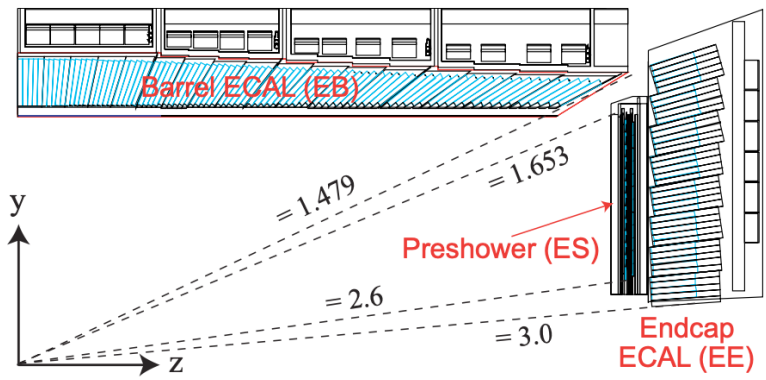

Figure 3.9: Transverse slice of the ECAL [36].

effect from electronics, digitization and pileup noise. Finally, C is the constant term and it comes from non-uniformity of the light, intercalibration errors and the leakage of the energy at the crystal.

From the beam test performed in 2006, the value of each term was obtained below:

$$(\sigma/E)^2 = \left(2.8\%/\sqrt{E}\right)^2 + (0.12/E)^2 + (0.30\%)^2 \tag{3.4}$$

It leads an excellence performance in the energy measurement, e.g. about 0.5% resolution for the electron with the energy of 120 GeV. The details on the ECAL performance can be found in [37].

3.2.4 HCAL

The hadronic calorimeter is designed to measure the energy of hardonic jets. Also it is important to measure missing transverse energy that comes from neutrino or exotic particles in new physics. The HCAL is divided into 4 subsystems as illustrated in Fig. 3.10.

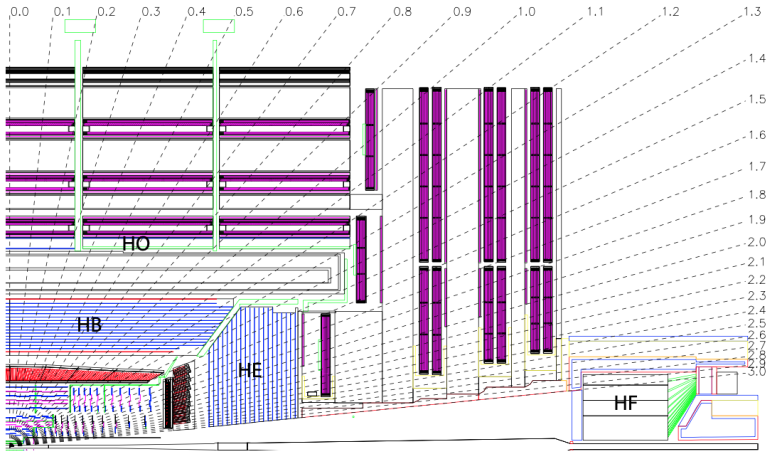

Figure 3.10: Geometry of HCAL [34].

Structure

The barrel of HCAL (HB), located just after the ECAL barrel detector, is a sampling detector that covers $|\eta| < 1.3$. It is composed of successive layers of absorber and scintillator, and a hadronic particle produces many secondary particles ("showers") by going through the multi layers of the absorber. The energy of the hadronic jets are measured by the light collected from the scintillator. For HB, absorber is brass (70% Cu and 30% Zn) with interaction length (λ_I) of 16.42 cm and a plastic scintillator is used. The effective interaction length of HB goes up to about $11\lambda_I$.

Another hadron calorimeter, or called tail catcher, is placed outside the solenoid to compensate HB which has limited interaction length due to the restriction of the space between ECAL and the magnet coil.

The HCAL endcap detector (HE) covers $1.3 < |\eta| < 3$, and it also has a similar concept with HB and consists of brass absorber and scintillator layers. The interaction length of HE is around $10\lambda_I$.

For the very forward region with $3 < |\eta| < 5.2$, the forward hadronic

calorimeter covers and the energy of the forward particles measured here is important for the estimation of missing transverse energy. It measures the energy by capturing the Cherenkov light via quartz fibers, which can stands for hard radiation damage in the very forward region.

Performance

The energy resolution of the hadronic jets is around 10–15% for a 100 GeV jets depending on the η range. The resolution is getting better for the jets with higher energy.

3.2.5 Muon system

The muon system is located in the outermost part of CMS and detects the trajectory of muons that usually go through the inner part of CMS without significant energy loss. The system is composed of gas ionization detectors sandwiched by the layers of steel flux-return yoke. The overview of the muon system is shown in Fig. 3.11.

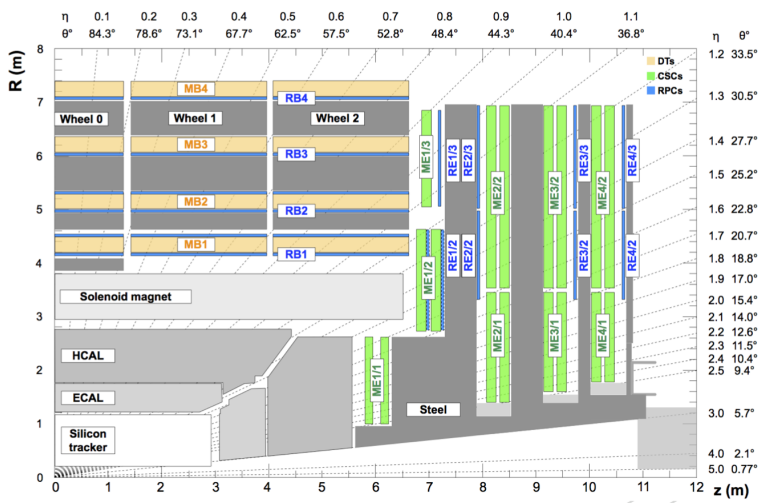

Figure 3.11: The overview of the muon system in (r,z) plane [38].

Structure

The barrel region is composed of drift tube (DT) chambers covering $|\eta| < 1.2$. The smallest unit of the barrel detector is the drift cell, which measures the muon position by the drift time of the electron to its anode wire in the gas made of 85% Ar + 15% CO_2.

4 Layers of drift cell staggered by half a cell is called a superlayer, and a DT chamber consists of 2 or 3 superlayers. Finally, the collection of 8 stations form a station that inserted between the steel yoke (MB1, MB2 and MB3) as seen in Fig. 3.11. In each station, 4 chambers perform the measurement in (r, *phi*) plane and the other 4 chambers do the measurement in z direction. In the last station (MB4), there is no chambers corresponding z measurement.

For the muon detection in the endcap region where higher muon and backgorund rates are expected as well as non-uniform magnetic field, the cathode strip chambers (CSC) are used in $0.9 < |\eta| < 2.4$. It consists of positively charged anode wires and negatively charged cathode strips perpendicular to wires in a gas volume made of 40% Ar + 50% CO_2 + 10% CF_4. Passing through of a muon in the gas volume creates ions, and they move in a electric field made by wires and strips. The position of the muon can be measured by the interpolation of signals. A chamber has a trapezoidal shape composed of 6 layers of the wires in 7 cathode panels, and the number of chambers in each station is 36 or 72 depending on the location.

THe Resistive Plate Chamber (RPC) complements DT and CSC operation in $|\eta| < 1.9$ with a fast timing information in an order of 1 ns, and therefore mainly used for triggering.

Performance

The offline muon reconstruction efficiency reaches to about 99% in most of the region except for the region with a chimney ($|\eta| \sim 0.25$) and the transition region between DT and CSC ($|\eta| \sim 0.8$).

The muon momentum resolution measured by the muon system only is about 9% for the muon with p_T up to 200 GeV, but it increases to 15–40% depending on η for 1 TeV muon due to smaller bending angle. However, the resolution goes down to about 5% in the combination of information in the inner tracker and muon system.

3.2.6 Trigger system

With 25 ns bunch crossing in the collision at LHC, an unprecedented amount of the data is produced with the bunch crossing frequency of about 40 MHz. Storing and processing all of the produced event are not feasible and also not efficient as most of the events collected in such a way are not physically interested in terms of the view of the discovery machine for new physics. Therefore, a significant amount of the event rate is necessary for the operation and the trigger system plays such a role by analyzing the events in real time and selecting potentially interesting events in physics point of view. In contrast to offline reconstruction, the data loss from a failure in the trigger system cannot be recovered. The stable operation is essential for the system as well as its fast processing ability.

The trigger system is divided into two parts. The first system is L1 trigger. It is made of programmable custom-made hardware chips (FPGA) that ensures fast processing (within 4 μs) than usual software based one. Based on coarse measurements from the calorimeter and muon detector, L1 trigger reduced the rate from about 40 MHz to the order of 100 kHz.

The overall structure of L1 trigger is illustrated in Fig. 3.12. The calorimeter based objects (e.g. electron, photon, jet, tau, missing transverse energy) are reconstructed in the Global Calorimeter Trigger (GCT) based on the information from Regional Calorimeter Trigger that connected to ECAL, HCAL and HF via Trigger Primitive Generators. For the muon trigger, muon candidates are made in each muon system (DT, CSC and RPC) and they are sent to Global Muon Trigger (GMT), which determines best 4 muon candidates. In the Global Trigger, it makes trigger decisions for maximum 128 trigger paths based on the information from GMT and GCT.

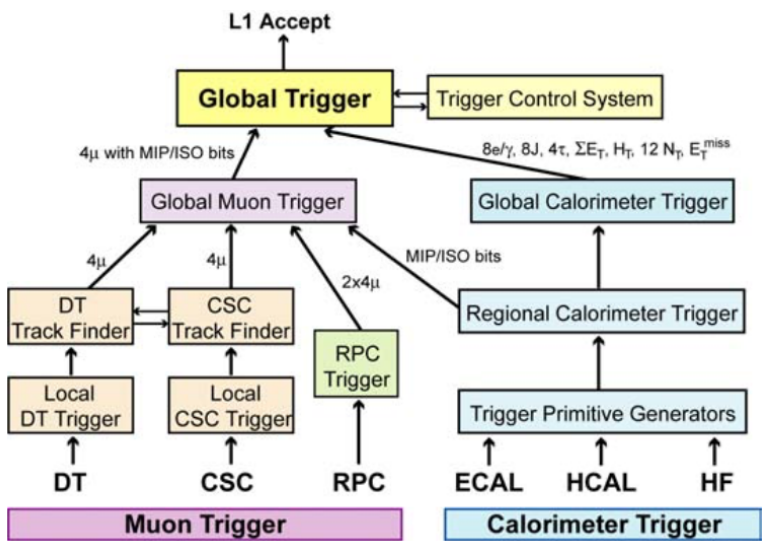

Figure 3.12: Overview of the L1 trigger system in Run 1.

At the early stage of Run2 (2016), L1 trigger system is upgraded to maintain the performance in smaller bunch crossing time and higher luminosity as well as pileup compared to Run 1 [39]. In includes the upgrade of electronics and improved algorithm in calorimeter triggers. Muon trigger is also upgraded from the track reconstruction in each subsystem (DT and CSC track finders)

to the region-based reconstruction (barrel, overlap and endcap track finders) to take into account the overlap between subsystems.

The next step is the high level trigger (HLT) operated in the collection of commercial processors ("HLT farm") using the same software used in the offline reconstruction. However, the reconstruction algorithm of the physics objects can be slightly different with the offline and optimized to match the strict requirement in HLT including efficiency, rate, and calculation time. As HLT is software based, the HLT menu has high flexibility that makes it easy to frequently update during the data taking (usually between fills) to obtain higher performance or include a new trigger aiming a specific physics topology. However, any change in HLT should be proven not to violate the HLT requirements mentioned above before the implementation. HLT accesses the whole event information (including inner tracker information which is not available in L1) and can perform more complicated analysis than L1 step. It enables HLT to reduce the rate further from 100 kHz to the order of 1 kHz, which is acceptable amount of the data for Tier-0, the computing infrastructure at CERN, to be transferred to the permanent storage.

3.2.7 Data acquisition system

The Data Acquisition system (DAQ) is designed to collect and analyze the data via interplay with the trigger system. It should be able to take the order of 100 kHz from L1 trigger with ~ 60 GByte/s data flow, and also provide the enough computing resource for event filtering in HLT.

The brief overview of the DAQ system is shown in Fig. 3.13. During the data taking, front-end systems (FES) continuously stores the data in connected buffers. If Timing, Trigger and Control (TTC) system send a L1 trigger signal, Front-End Drivers (FEDs) send the data saved in the buffers of FES to DAQ

system. The event builder collects the event fragments assigned to same L1 from all FEDs and build a complete event, which is sent to the Event Filter for analyzing. To protect the DAQ system from the back pressure, which could lead buffer overflow and loss of data or out of time synchronization, The Trigger-Throttling System (TTS) is used and avoid the overflow by fast feedback between subdetector's front-end and the Global Trigger Processor (GTP).

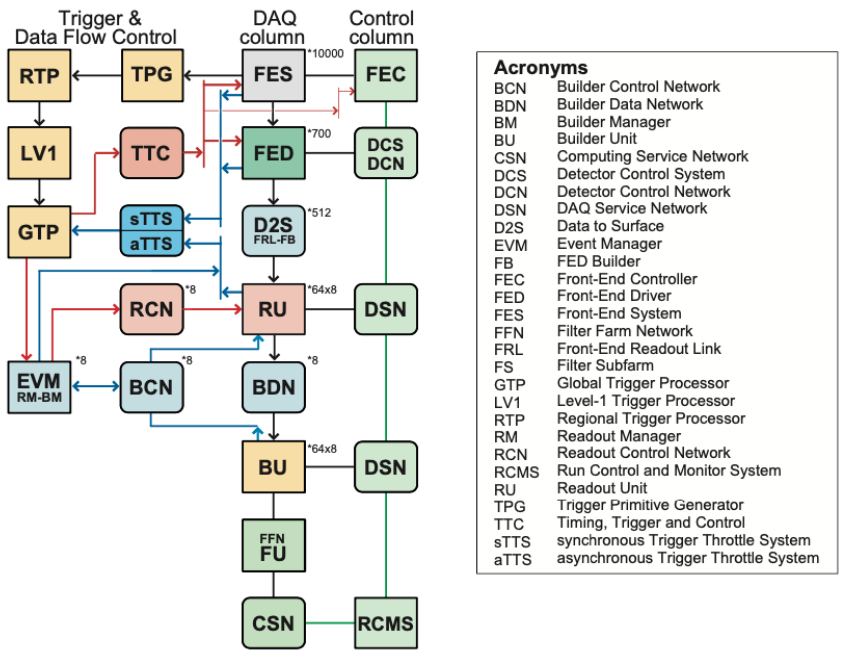

Figure 3.13: The overview of the DAQ system [34].

Chapter 4

Physics object reconstruction

From the detector responses (hits, energy deposits, etc) produced by the particles passing through the detector, the physics objects are reconstructed to be used in physics analyses. The reconstructed object and its identification used in the analysis should be carefully chosen with understanding of its advantage and limitation, and therefore the knowledge on the reconstruction algorithm is important for physics analyses to obtain reliable results. In this section, the reconstruction method of each physics object is discussed. After the description on the global event reconstruction algorithm, the details on the muon, electron, jet and missing transverse energy will be followed.

4.1 Global event reconstruction: Particle flow algorithm

The "particle flow" (PF) algorithm [40] is the reconstruction algorithm to reconstruct physics objects by combining the information from all subdetectors so called global event reconstruction. Traditionally, the object reconstruction

at hadron colliders is performed relying on a relevant subdetector. Jets, which is a energy deposit produced by the hadronization of a quark or gluon in a small cone, are reconstructed by clustering the energy measured in the calorimeter without any separation of individual particles inside of jets. The missing transverse energy (MET) also reconstructed based on the calorimeter information only. The reconstruction of leptons also mainly relies on corresponding subdetectors (muon detectors for muons and ECAL for electrons and photons). The tracker contributes to tagging of jets to identify them from hadronic τ decay or b-quark hadronization.

However, thanks to the fine granularity of the CMS detector enough to provide good separation between individual particles, the PF algorithm can be implemented in the object reconstruction and it significantly improves the particle identification and the measurement of the particle properties (e.g. direction, energy momentum) compared to the traditional approach. For example, the connection of the tracker and calorimeter information leads better measurements on jets. The charged hadrons can be separated from the jets by identifying them via matching between a track in inner tracker and energy deposit in the calorimeter. Their momentum and direction can be updated with the measurement from the inner tracker with superior resolution. If no matched track is found, the object is assigned to neutral hadron or photon, and they are further separated based on the energy deposit in ECAL and HCAL. The measurement of energy can be improved by the energy calibration depending on photon or hadron hypothesis. The electrons and muons, identified by the connection between tracker and ECAL (electrons) or muon detector (muons), are not included in the jet reconstruction, which also helpful to obtain the genuine quark or gluons momentum from jet. The effect from pileup interactions, which was one of the major concern to implement the PF algo-

rithm in hadron collider experiments, is reduced by several pileup mitigation methods and under control.

The PF algorithm starts from the reconstruction of PF elements consists of 1) tracks for charged particles including dedicated one for electrons and muons and 2) calorimeter clusters in the preshower, the ECAL, and the HCAL. The physics objects from PF algorithm ("PF candidate") are reconstructed by linking the PF elements.

4.2 Muon reconstruction

The muon reconstruction [38] is based on the information from the inner tracker and the muon system. There are three types of muons depending on how it is reconstructed.

The "standalone muon" is reconstructed using the information from muon system only. The seeds of the muon track are made by DT or CSC segments, and the tracks are built by the Kalman Filter (KF) technique using the hits in each subsystem. It has a worse resolution compared to the other two types followed later, and is contaminated by cosmic muons as no information in the inner track is used.

The "global muon" is reconstructed by combining the standalone muon track and inner track by geometrically matching after propagating to a common surface. Once the matched track pairs are found, a combined fit is performed using KF technique. The global muon has advantage in reducing the contribution from the hadrons that reach the muon system (innermost layer only in most of cases) called "punch through", which can be misidentified as muons. Also, for the high p_T muons with $p_T > 200\,\text{GeV}$, the momentum resolution is better than the one from inner tracker only.

The last type is "tracker muon", which is reconstructed by loosely matching

between a inner track and the segement in the muon system. The inner tracks with $p_T > 0.5\,\mathrm{GeV}$ and $p > 2.5\,\mathrm{GeV}$ is used for the extrapolation to the muon system. It contributes to the increase of the efficiency for low p_T muon below around 10 GeV which is hard to leave a signature through multilayers in the muon system. The muon efficiency of global or tracker muon reach about 99% within the acceptance of the muon system.

4.3 Electron and photon reconstruction

The reconstruction of e/γ objects is performed using the combined information form the inner tracker and the energy deposit in ECAL. In the case of the photons, the photon does not leave any signals in the inner tracker. Thus, the seed of the photon is just the supercluster in ECAL with $E_T > 10\,\mathrm{GeV}$ *without* links to inner tracks, and distinguish further from the electrons using the variables related to the size and shape of the energy deposit [41].

For the electron reconstruction [42], there are two ways to create electron seeds in the tracker. The ECAL-based approach starts from ECAL clusters with the energy deposit larger than 4 GeV. To take into account the energy deposit from the emitted bremsstrahlung photons from the electron, the deposits are summed in a group of clusters ("supercluster") that has small η window and extended ϕ window, which takes into account the bending of electrons in azimuthal direction under the magnetic field. For the seeds, the hits in the innermost tracker layer is selected if their directions are compatible with the direction of the superclusters.

However, the seeds from ECAL-based approach has a limited performance to reconstruct electrons inside of jets, which leads large overlap of energy deposits and hits around the electrons. Also, it does not work well either for the low-p_T electrons which have large bending angle and make the supercluster

hard to contain the all spread energy deposit in ϕ direction. To compensate the loss of electrons in ECAL-based approach, the tracker-based approach is developed in the context of the PF algorithm. It starts from the tracks made in the iterative tracking made by KF technique for charged particle tracks. If a KF track is well geometrically matched and also its momentum is compatible with the energy in corresponding PF cluster, its seed is selected as the electron seed. For the KF tracks with small number of hits or large χ^2, which could result from a substantial energy loss by emitting bremsstrahlung photons, they are fitted again using Gaussian-sum filter (GSF) [43] to take into account such energy loss. They are selected as electron seeds based on the booted-decision-tree classifier trained with various KF and GSF track parameters and the geometrical and energy matching to ECAL. This approach is also helpful to identify e^-e^+ pairs from conversions using the inner track information.

In the track reconstruction step, the seeds from ECAL-based and tracker-based approaches are merged together. The track building is performed via combinatorial KF technique and the energy loss is modeled by a Bethe–Heitler function. The track parameters are estimated by GSF fitting among the collected hits.

The electrons have high probability to radiate a photon (bremsstrahlung) in the tracker material, and a usual tracks from iterative tracking with KF method can fail to reconstruct the electron tracks appropriately. Therefore, a dedicated approach for electron track reconstruction is implemented via . After selecting the tracks made by KF method with small number of hits or large χ^2, which could result from a substantial energy loss by emitting bremsstrahlung photons, they are fitted again using GSF to take into account such energy loss. Also, in order to reduce the misreconstructed tracks, a requirement is imposed at the final step on the score of each track from a booted-decision-tree classifier

trained with various track parameters and the spatial relation with ECAL.

The electron candidates finally made with the association between a reconstructed inner track and corresponding ECAL energy deposit, which is used in creating seeds.

4.4 Jet reconstruction

The jets, produced by the hadronization of a quark or gluon, are reconstructed by clustering the PF elements such as hadrons and non-isolated photons. They are reconstructed in PF algorithm after the reconstruction of muon, electron and isolated photons.

Within the tracker acceptance ($|\eta| < 2.5$), The ECAL clsuters and HCAL clusters without links to the inner tracks are considered as photons and neutral hadrons, respectively. However, over the tracker acceptance where the charged hadron and neutral hadron cannot be separated, the ECAL clusters linked to HCAL cluster are interpreted as the contribution from charged and neutral hadrons, and the ECAL clusters without links are considered as photons.

If the ECAL and HCAL clusters are linked to inner tracks, the sum of the energy (strictly speaking, the calibrated energy described in [40]) and the sum of the momentum of associated inner tracks are compared. In the case when the calorimeter energy is larger than the sum of track momentum, the excessive energy is considered as the contribution from neutral hadrons or photons. The remaining energy are assigned to charged hadrons.

Once the PF elements are reconstructed, the clustering of them is performed by anti-k_T algorithm [44]. It starts with the definition of the distance between i and jth entries d_ij such that:

$$d_{ij} = \min(k_{ti}^{2p}, k_{tj}^{2p}) \frac{\Delta_{ij}^2}{R^2} \tag{4.1}$$

where k_{ti}^{2p} and k_{tj}^{2p} is the transverse momentum of i and j entries respectively, and $\Delta_{ij}^2 = (y_i - y_j)^2 + (\phi_i - \phi_j)^2$ represents the spatial distance between entries with the rapidity y and azimuthal angle ϕ. The R is a user defined cone size, and 0.4 is widely used in CMS. The $p = 1$ and $p = 0$ correspond to k_T and Cambridge/Aachen algorithms respectively, and the anti-k_T algorithm uses $p = -1$. With the above distance d_{ij}, the smallest distance is calculated among entries. If it is d_{ij}, the entry i and j are combined into one single entry. If it is $d_{iB} = k_{ti}^{2p}$, it is removed from the entry. The procedure is repeated until there is no remaining entry.

Once the jets are reconstructed, the jet energy corrections (JEC) are applied to both data and MC in order to match the reconstructed energy to the true value. For the MC, additional correction is applied called jet energy resolution (JER) that smear the jet energy in MC to match the worse energy resolution in the data. The details on both corrections can be found in [45].

4.5 Missing transverse energy reconstruction

In the collision at LHC, the sum of the transverse momentum should be zero in an ideal condition due to the momentum conservation. However, if particles that are not interect with detectors like neutrinos or hypothetical particles expected in BSM makes a missing transverse energy are produced after the collision, their transverse energy can be inferred from the deviation of the sum of transverse momentum from zero.

Therefore, the missing transverse energy (MET, $\vec{p_T}^{miss}$) is defined of the negative vector sum of the all reconstructed particles by PF algorithm as below:

$$\vec{p_T}^{miss} = -\sum_{i}^{N_{PF}} \vec{p_{T,i}} \tag{4.2}$$

The correction term can be added in above expression after taking into account JER for PF jets with $p_T > 10\,\text{GeV}$ in the sum:

$$\vec{p_T}^{miss} = -\sum_{i}^{N_{PF}} \vec{p_{T,i}} - \sum_{i}^{N_{PFJets}} \left(\vec{p_{T,i}^{corr.}} - \vec{p_{T,i}}\right) \tag{4.3}$$

The correction reduces the bias on the MET from the minimun energy threshold of the calorimeters, inefficiencies in the tracker, and so on.

Further correction can be considered to mitigate the effect from the pileup interactions. The induced MET from pileup are estimated by the vector sum of the charged particles from a plieup vertex ($\vec{v}$) using the parametrization with the form:

$$f(\vec{v}) = c_1(1.0 + \text{erf}(-c_2|\vec{v}|^{c_3})) \tag{4.4}$$

where the efficients c_1, c_2 and c_3 are determined by the study on the simulated events with exactly one pp collsion. To obtain the pileup-mitigated MET, the contribution of induced MET from the pilup are subtracted as below:

$$\vec{p_T}^{miss}(\text{mitigated}) = \vec{p_T}^{miss} - \sum_{PU} f(\vec{v})\vec{v} \tag{4.5}$$

The details on the MET reconstruction can be found in [46].

Chapter 5

Event selection and background estimation

From this chapter, the analysis for the measurement of the differential Drell-Yan cross section will be described. The contents are based on the results published in a journal [47].

5.1 Analysis overview

The goal of the analysis is to measure the differential crosss sections of DY process with respect to the dilepton mass m, $d\sigma/dm$. The mass range is from 15 GeV to 3000 GeV whose upper limit is extended to the higher value compared to the previous analyses [48, 49, 50] thanks to the increase of center of mass energy. The coverage of the longitudinal momentum fraction of interacting parton x is around $10^{-4} < \mathrm{x} < 1.0$ with the mass range.

The binning of the dilepton mass consists of 43 bins with the edges below.

$$
\begin{aligned}
&15,\ 20,\ 25,\ 30,\ 35,\ 40,\ 45,\ 50,\ 55,\ 60,\\
&64,\ 68,\ 72,\ 76,\ 81,\ 86,\ 91,\ 96,\ 101,\ 106,\\
&110,\ 115,\ 120,\ 126,\ 133,\ 141,\ 150,\ 160,\ 171,\ 185,\\
&200,\ 220,\ 243,\ 273,\ 320,\ 380,\ 440,\ 510,\ 600,\ 700,\\
&830,\ 1000,\ 1500,\ 3000\ \text{GeV}
\end{aligned}
\tag{5.1}
$$

It is identical with the one used in the previous analysis [50] except for the upper limit and 830 GeV bin edge.

The cross section of ith mass bin is calculated by the fomula below:

$$
\sigma_i = \frac{N_i}{A_i\,\varepsilon_i\,\rho_i\,L}, \tag{5.2}
$$

The number of observed signal yield N_i is corrected by the acceptance A_i and efficinecy ε_i, and additional scale factor ρ_i is applied to correct the efficiency difference between the data and simulation. Finally, the value is normalized by the total integrated luminosity of the data L.

The summary of the analysis procedure is shown in the Fig. 5.1. The first step is the event selection where the events expected to have leptons from DY process are selected by looking for two prompt and isolated leptons. Basic corrections for pileup reweighting to MC and muon (electron) momentum (energy) scale and resolution are also applied in this step.

The next step is the estimation of the backgrounds coming from SM processes with genuine or misidentified leptons. The backgrounds are estimated from the data itself or MC simulation depending on the characteristic of each physics process.

After the backgrounds are estimated and subtracted from the data, various corrections are applied. The first correction is applied by unfolding technique

to correct migration effects between bins originated from the momentum or energy resolution of leptons. After the unfolding, the acceptance and efficiency corrections are applied to compensate lost signals due to the kinematic acceptance of the detector or the reconstruction and identification procedure. The efficiency scale factor, the ratio of the efficiency between the data and simulation, is also taken into account to correct the difference between the data and simulation. The final correction is another unfolding step to correct bin migration effect due to lost momentum of leptons from the Final State Radiation (FSR) effect.

Once all corrections are applied and the central values of the cross sections are obtained, the uncertainties, originated from various steps in the analysis procedure, are estimated.

Finally, the cross section values associated with estimated uncertainties are obtained and compared to the theoretical prediction at NLO and NNLO accuracy. The combination of the two channels is also performed after checking the compatibility of the cross section results between two channels. Details on each procedure will be discussed later one by one.

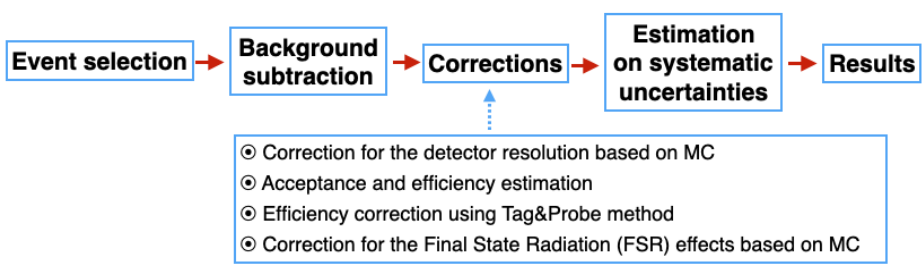

Figure 5.1: Analysis procedure for the DY $d\sigma/dm$ measurement.

5.2 Data and MC samples

5.2.1 Data

The measurement is based on the proton-proton collision data at $\sqrt{s} = 13$ TeV collected with the CMS detector at the LHC in 2015. Only the luminosity sections certified as good for physics analyses are used, which correspond to an integrated luminosity of 2.8 fb^{-1} and 2.3 fb^{-1} for the dimuon and dielectron channel respectively. The events for the dimuon channel are triggered by an isolated muon with $p_{\text{T}} > 20\,\text{GeV}$ and $|\eta| < 2.4$. For the dielectron channel, the events are triggered by an isolated electron passing a loose identification criteria with $p_{\text{T}} > 23\,\text{GeV}$ and $|\eta| < 2.5$.

5.2.2 MC samples

Various MC samples are used for the analysis to estimate backgrounds and derive various corrections including the acceptance, efficiency, efficiency scale factors and the unfolding corrections. The list of the used MC samples is summarized in Table 5.1 with the generator for each sample.

Process	Generator
$\text{Z}/\gamma^* \to \ell\ell$ $(10 < m(\ell\ell) < 3000\,\text{GeV})$	MadGraph5_aMC@NLO v2.2.2 [51]
W+jets	MadGraph5_aMC@NLO v2.2.2
$\text{t}\bar{\text{t}}$	POWHEG v2.0 [52, 53, 54, 55]
tW and $\bar{\text{t}}\text{W}$	POWHEG v1.0 [56]
WW, WZ and ZZ	PYTHIA v8.212 [57]

Table 5.1: List of MC samples for the measurement.

All samples are produced with NNPDF3.0 PDF set [58, 59]. The PYTHIA

generator with the underlying event tune CUETP8M1 [60] is used for hadronization and parton shower simulation for all samples.

For the cross sections of each physics process, which is used for normalization of MC events to the integrated luminosity of the data, the values with the highest accuracy available are used. The cross section of DY process is at NLO accuracy calculated by MadGraph5_aMC@NLO. The $t\bar{t}$ cross section is at NNLO+NNLL (next-to-next-to-leading logarithm) accuracy [61]. tW, $\bar{t}$W and diboson events are normalized using the cross section at NLO accuracy [62, 63].

The detector response is simulated using Geant4 [64] in all samples. Simulated events are reconstructed using the same software used for the real data. Minimum bias events are superimposed in each MC event to mimic the pileup effect in the data with average value of 11. All MC samples are reweighted to have the same pileup distribution with the data.

5.3 Event selection

The event selection procedure aims to select two prompt and isolated leptons originated from the DY process.

5.3.1 Dimuon channel

Regarding the restriction on the kinematic variables, the offline muon candidates are required to be within the acceptance of the CMS detector, $|\eta| < 2.4$. Also, the leading muon should have $p_{\mathrm{T}} > 22\,\mathrm{GeV}$ to ensure that it is in the plateau region of the trigger efficiency. The requirement on the p_{T} of the training muon is $p_{\mathrm{T}} > 10\,\mathrm{GeV}$.

To select muon candidates, the standard CMS muon identification criteria optimized for the high-p_{T} muons ($p_{\mathrm{T}} > 200\,\mathrm{GeV}$) is used, which includes

various requirements on the information from the inner tracker and the muon system. The muon should be reconstructed as a global muon, which is made by a global fit from a track in the inner tracker and another track in the muon system. In addition, the number of the valid pixel hits and the tracker layer should be larger than 0 and 5, respectively. The transverse and longitudinal impact parameter with respect to the primary vertex should be smaller than 2 and 5 mm. This requirement helps to suppress the muons from decay in flight similar to the requirement on the number of pixel hits and tracker layer. Furthermore, there should be at least one hit in the muon system and two muon stations with muon segments. These requirements suppress misidentified muons originated from hadronic events with high energy enough to leave hits in the muon system (punch-through). Finally, the relative p_{T} error should be smaller than 30% to keep only muons with reliable p_{T} measurements.

To further suppress nonprompt muons from heavy flavor decays, the muon is required to have isolation smaller than 10% with respect to its p_{T}. The isolation is calculated by the p_{T} sum of the tracks in the inner tracker around the muon within $\Delta R < 0.3$ where $\Delta R = \sqrt{(\Delta\eta)^2 + (\Delta\phi)^2}$.

To select the dimuon candidates, the two muons should have opposite charge, and at least one muon should be matched to a object triggering the event. The opening angle between two muons is required to slightly differ from π by at least 5 mrad to suppress muons from cosmic ray going through regions near interaction point, which can appear as back-to-back dimuon event in the offline reconstruction. Also, the dimuon vertex χ^2 should be smaller than 20 to ensure that the dimuon events come from same vertex and reject dimuons made by arbitrary combination of muons from kaon or pion decays. If there are multiple dimuon pairs satisfying all conditions in a event, the pair with smallest vertex χ^2 is selected.

Details on the muon reconstruction, identification procedure and their performances can be found in Ref. [38].

The summary of the event selection in the dimuon channel is shown in Table 5.2.

Type	Requirements
Kinematic variable	$p_{\mathrm{T}} > 22, 10\,\mathrm{GeV}$ and $\lvert\eta\rvert < 2.4$
Muon candidate	Global muon $N_{\mathrm{pixelhits}} > 0$ and $N_{\mathrm{trackerlayer}} > 5$ $d_{\mathrm{xy}} < 2\,\mathrm{mm}$ and $d_{\mathrm{z}} < 5\,\mathrm{mm}$ $N_{\mathrm{muonhit}} > 0$ and $N_{\mathrm{station}} > 2$ $\sigma(p_{\mathrm{T}})/p_{\mathrm{T}} < 0.3$
Dimuon candidate	Opposite sign at least 1 muon matched to a trigger object $\mathrm{Angle}(\mu_1, \mu_2) < \pi - 0.005$ (rad) Dimuon vertex $\chi^2 < 20$

Table 5.2: Summary of the event selection in the dimuon channel.

The kinematic distributions of muons (p_{T}, η) after the event seletion are shown in Fig. 5.2.

5.3.2 Dielectron channel

The requirement on the kinematic variables is $|\eta| < 2.5$ with excluding the transition region between barrel and endcap detector in ECAL ($1.444 < |\eta| < 1.566$) to be within the acceptance of CMS detector. With the same reason with the dimuon channel, the leading electron is required to have p_{T} larger than 30 GeV. The p_{T} requirement on the trailing electron is $p_{\mathrm{T}} > 10\,\mathrm{GeV}$,

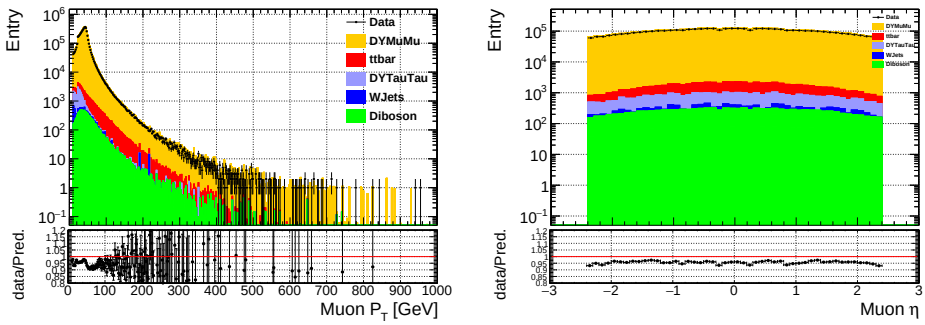

Figure 5.2: The distribution of muon p_{T} and η after the event selection.

synchronized with dimuon channel.

The dielectron channel uses the standard CMS identification criteria that aims to about 80% efficiency per electron to select electron candidates. The variables used for the identification is explained below, and the exact criteria is summarized in Table 5.3.

- $\sigma_{i\eta i\eta}$: the width of the shape of the energy deposit along the η direction. It helps to distinguish genuine electrons from misidentified electrons coming from jets with large electromagnatic showers because electromagnatic showers usually have narrower shape than hadronic showers.

- H/E: The ratio of the energy deposit at the HCAL and ECAL. Genuine electron is expected to have small ratio compared to jets misidentified as electrons.

- $|\Delta\eta_{\mathrm{In}}|$ and $|\Delta\phi_{\mathrm{In}}|$: The η and ϕ difference between the track at the inner tracker propagated to the super cluster at ECAL and the position of the cluster itself.

- $1/E - 1/P$: The difference of energy deposited in ECAL and the momentum measured by the curvature of the track.

- d_{xy} and d_z: transverse and longitudinal impact parameter from the primary vertex.

- $N_{missinghits}$: expected number of missing hits. It is used to suppress electrons from photon conversion that have higher probability to have missing hits.

- Conversion veto: Boolean defined by several conditions to reject electrons from conversion [65, 66].

- PFIso/p_T: isolation requirement relative to electron p_T to suppress non-prompt electrons similar to muons. The isolation is calculated by the energy sum of photons, charged hardon and neutral hadrons around the electron within $\Delta R < 0.3$ reconstructed by the PF algorithm [67].

For the dielectron candidate, at least one electron should be matched to a trigger object. Only the events that have exact 2 electrons satisfying the above identification are used. No requirement on opposite sign or vertex χ^2 is used to minimize the signal efficiency loss.

More details on the electron reconstruction, identification can be found in Refs. [65, 66] with their performance.

The kinematic distributions of electrons (p_T, η) after the event seletion are shown in Fig. 5.3.

5.4 Momentum scale and resolution correction

The momentum or energy of the reconstructed leptons can be imperfectly measured due to the effects from detector misalignments or conditions, which affects in the dilepton mass distribution. The resolution and scale corrections are applied to each lepton candidate in the dimuon channel [68] and dielectron

Variable	Barrel	Endcap
$\sigma_{i\eta i\eta} <$	0.0101	0.0283
$H/E <$	0.0876	0.0678
$\lvert\Delta\eta_{\mathrm{In}}\rvert <$	0.0103	0.00733
$\lvert\Delta\phi_{\mathrm{In}}\rvert <$	0.0336	0.114
$1/E - 1/P <$	0.0174	0.0898
$d_{\mathrm{xy}} <$	0.0118	0.0739
$d_{\mathrm{z}} <$	0.373	0.602
$N_{\mathrm{missinghits}} \leq$	2	1
Conversion veto	yes	yes
$PFIso/p_{\mathrm{T}} <$	0.0766	0.0678

Table 5.3: Summary of the criteria on the variables in the electron identification.

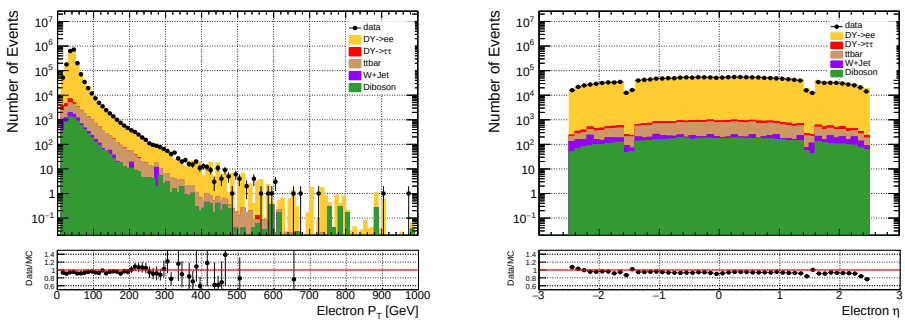

Figure 5.3: The distribution of electron p_{T} and η after the event selection.

channel [65, 66] respectively using the methods widely used in CMS. The effect of the corrections on the dilepton mass distribution near Z boson mass is shown in Fig. 5.4 in each channel. The corrections lead better agreement between data and simulation.

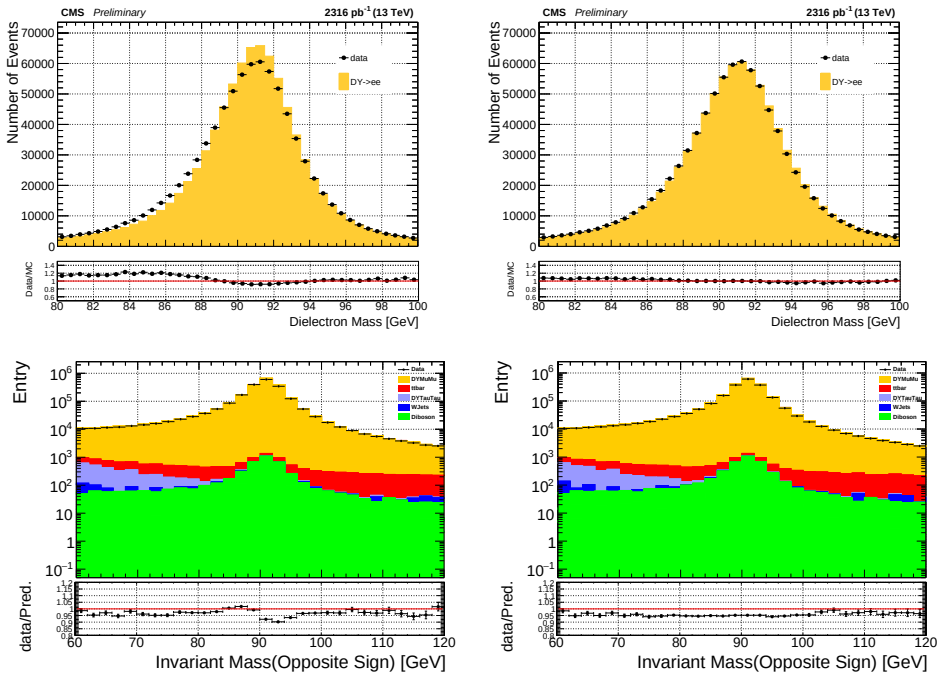

Figure 5.4: The dilepton mass distribution before (left) and after (right) applying resoluion and scale correction in the dielectron (top) and dimuon (bottom) channels.

5.5 Background estimation

The major background events in the measurement are top-quark associated events ($t\bar{t}$, tW and $\bar{t}W$). The dilepton events from QCD multijets and W+jets process are prominent in the low mass region below Z peak. The dimuon or dielectron pair from the decay of τ in $Z/\gamma^* \rightarrow \tau\tau$ process is one of the dominant

source near Z peak region, with the contribution of the leptons from diboson process.

The number of background events are estimated from the data itself whenever feasible to reduce the uncertainty associated with the simulation of the background processes. The remaining background events are estimated using the prediction from MC simulation.

5.5.1 Dimuon channel

eμ method

Major backgrounds with 2 genuine leptons in the final state ($t\bar{t}$, tW and $\bar{t}W$, WW and $Z/\gamma^* \to \tau\tau$) are estimated by so called eμ method, which exploits eμ data control sample and the branching ratio between eμ and $\mu\mu$ final state. The basic idea to estimate the background from a given process by eμ method is shown in (5.3).

$$N_{\text{est.}}^{\ell\ell} = N_{\text{data}}^{e\mu} \cdot \frac{N_{\text{MC}}^{\ell\ell}}{N_{\text{MC}}^{e\mu}} \tag{5.3}$$

The number of background events in the same flavor final state $N_{\text{est.}}^{\ell\ell}$ is estimated by multiplying the number of data events in eμ final state $N_{\text{data}}^{e\mu}$ and the branching fraction between $e\mu$ and $\ell\ell$ final state $N_{\text{MC}}^{\ell\ell}/N_{\text{MC}}^{e\mu}$. The fraction for $e\mu$ to $\ell\ell$ is expected to 2 in principle, but it can be differ from 2 due to various factors originated from the difference between e and μ in realistic condition, including acceptance, efficiency and FSR effect. Therefore, the fraction is estimated by MC simulation.

To obtain eμ events from the data, the data sample triggered by at least one isolated muon with $p_{\text{T}} > 20\,\text{GeV}$ (same trigger for dimuon channel) is used. The leading lepton between e and μ is required to have p_{T} larger than 22 GeV, and the trailing lepton should have $p_{\text{T}} > 10\,\text{GeV}$. The same identification

criteria with the one for the event selection is used for the electron and muon, respectively. The final eμ pair is selected if angle(e, μ) $< \pi - 0.005$ (rad) and eμ vertex $\chi^2 < 20$ to have consistent requirement with the dimuon candidates in the dimuon channel. The comparison of the data and prediction in selected eμ mass distribution is shown in Fig. 5.5.

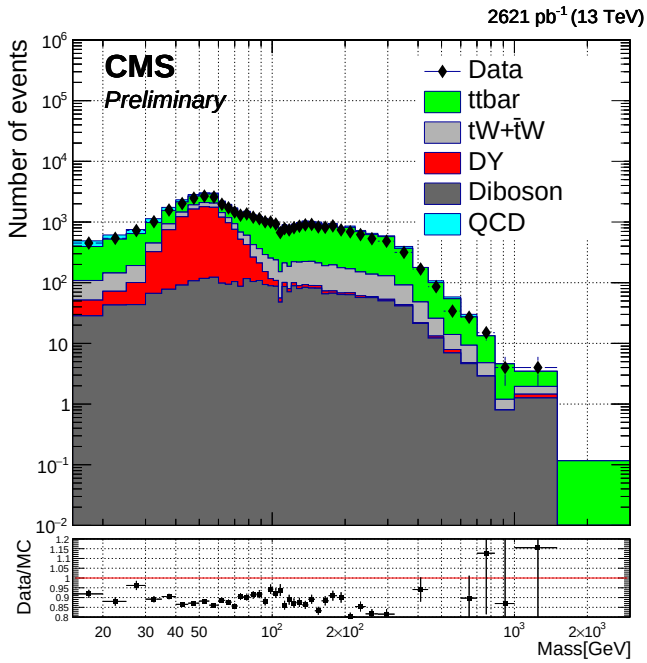

Figure 5.5: eμ mass distribution used for the background estimation in dimuon channel. The black point is the data, and filled colors are the MC prediction from each process except for QCD. The contribution from QCD is estimated by a data driven method.

The predictions in Fig. 5.5 come from MC simulation except for QCD, which is estimated by data driven technique used in [69]. The $e\mu$ events from QCD is basically from the decay of b quarks, and the ratio of the same sign to opposite sign $e\mu$ events R is a constant value 0.57 predicted by b mixing

probability. Therefore, the number of events with opposite sign is calculated by (5.4). $N_{data}^{\mu^{\pm}\mu^{\pm}}$ represents the eμ data events with same sign after subtracting the contribution from electroweak processes by MC simulation.

$$R = \frac{N^{\mu^{\pm}\mu^{\pm}}}{N^{\mu^{\pm}\mu^{\mp}}} \rightarrow N_{data}^{\mu^{\pm}\mu^{\mp}} = \frac{N_{data}^{\mu^{\pm}\mu^{\pm}}}{R} \tag{5.4}$$

The entire mass range is dominated by $\mathrm{t\bar{t}}$ process (green), followed by tW and $\bar{\mathrm{t}}$W events (gray). The contribution from $\mathrm{Z}\gamma^{*} \rightarrow \tau\tau$ (red) is prominent near 60 GeV. In general, the data and prediction agree within 10 to 20% level.

To estimate the number of background from each process, the amount of the eμ data events from a given process $N_{data,process}^{e\mu}$ is estimated by multiplying the fraction of the number of MC events from the process with respect to the total MC. For example, the number of $\mathrm{t\bar{t}}$ events are computed like below:

$$N_{data,\mathrm{t\bar{t}}}^{e\mu} = N_{data}^{e\mu} \times \frac{N_{MC,\mathrm{t\bar{t}}}^{e\mu}}{N_{MC,total}^{e\mu}} \tag{5.5}$$

The contribution in the dimuon channel from $\mathrm{t\bar{t}}$ events are estimated by applying (5.3):

$$N_{data,\mathrm{t\bar{t}}}^{\mu\mu} = N_{data,\mathrm{t\bar{t}}}^{e\mu} \times \frac{N_{\mathrm{MC}}^{\mu\mu}}{N_{\mathrm{MC}}^{e\mu}} \tag{5.6}$$

The estimated number of backgrounds from each process by eμ method is shown in Fig. 5.6 with the comparison to MC simulation.

Fake rate method

Instead of backgrounds with two prompt leptons (estimated by eμ method), other type of the backgrounds including at least one object misidentified as prompt lepton (W+jets and QCD) are estimated by "fake rate" method that uses the misidentification rate of single leptons ("fake rate"). The fake rate

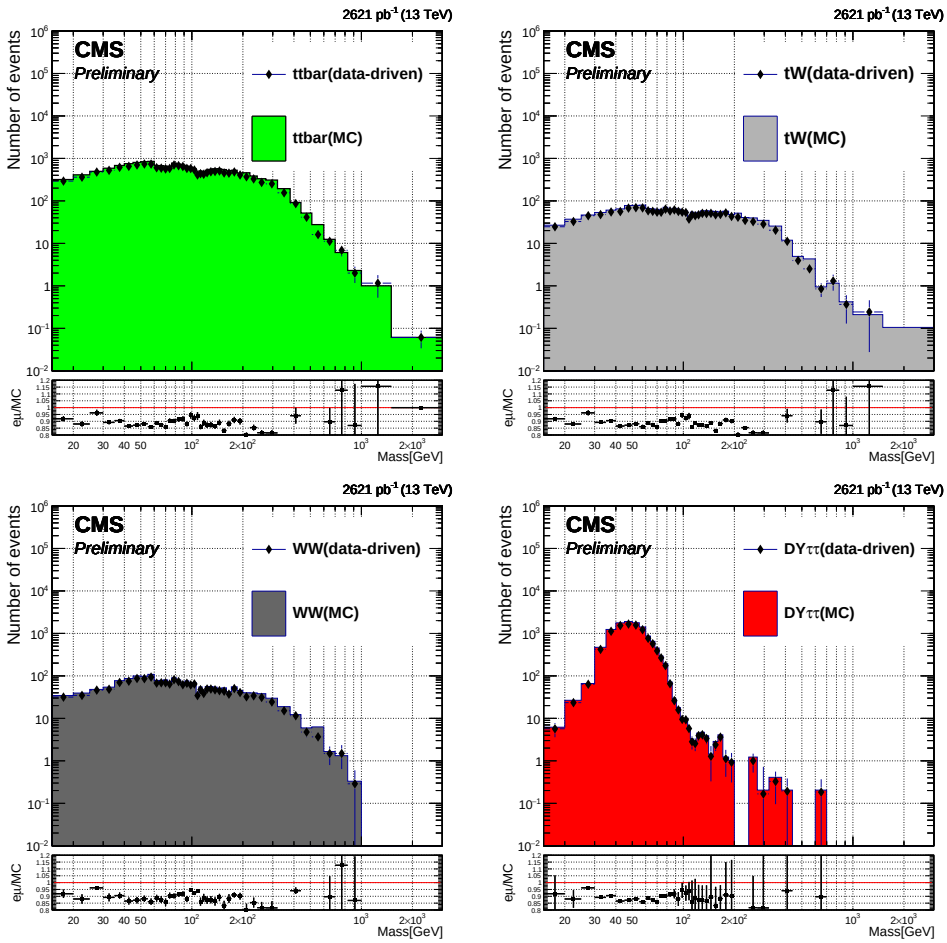

Figure 5.6: The dilepton mass distribution estimated by eμ method for background processes ($t\bar{t}$ on top left, tW and $\bar{t}$W on top right, WW on bottom left and $Z\gamma^* \rightarrow \tau\tau$ on bottom right). Each distribution is compared to the MC simulation. The difference between estimated number of events and MC simulation is assigned as one of the systematic uncertainty sources.

is derived from a data control sample and defined as the probability of the misidentified lepton passing the lepton identification criteria. To estimate the backgrounds from fakes, a weight based on the estimated fake rate is applied to a fake-dominated data sample to convert them to the number of events passing the event selection criteria.

The fake rate in the dimuon channel is estimated by the fraction of muons from QCD passing the muon identification criteria (Section 5.3) with respect to the number of QCD muons passing loose isolation criteria in the data.

The main difficulty of the fake rate measurement is to extract QCD muons in the data because the data sample satisfying the denominator (loose isolation) and numerator (full selection) is largely contaminated by electroweak processes including Z/γ^*, top-quark and diboson processes and also the fake leptons are not described well by MC simulation.

The two methods are considered to extract QCD muons. The first method is called "ratio method" based on the assumption that MC simulation describes (at least) the fraction of QCD muons in the data well. The number of QCD muons in data ($N_{data}^{\mu,QCD}$) is estimated by multiplying the fraction of number of QCD muons from MC ($N_{MC}^{\mu,QCD}$) with respect to total MC muons ($N_{MC}^{\mu,total}$) to the number of total number of leptons in data ($N_{data}^{\mu,total}$):

$$N_{data}^{\mu,QCD} = N_{data}^{\mu,total} \times \frac{N_{MC}^{\mu,QCD}}{N_{MC}^{\mu,total}} \tag{5.7}$$

The second method is called "template fitting" which directly fit the data using the template shape obtained from MC, and the fraction of QCD in the data is extracted from the fit results. The isolation distribution is used for the template fitting as the shape is distinguishable between QCD and the other electroweak processes.

The second method is selected as the primary method to estimate the fake

rate because it provides more reliable estimation of QCD fraction by directly fitting to the data. The difference with the fake rate estimated by ratio method is used as the systematic uncertainty.

The fake rate parametrized in muon p_{T} in barrel and endcap is shown in Fig. 5.7.

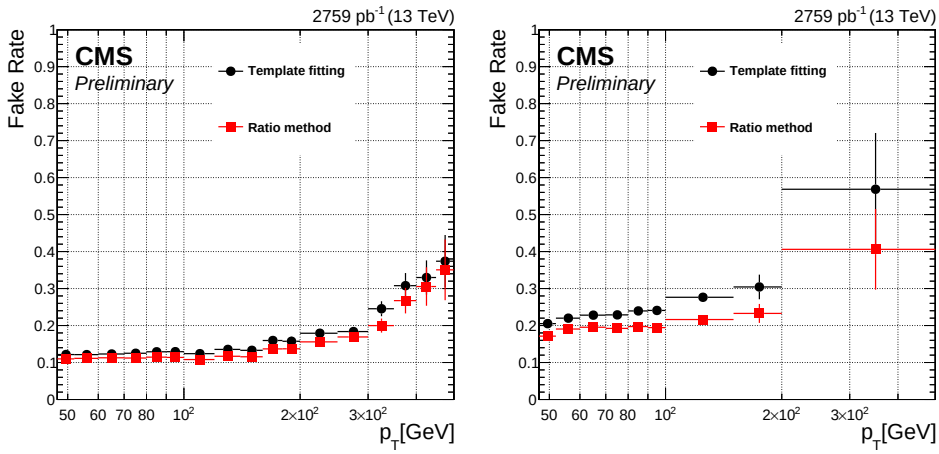

Figure 5.7: The muon fake rate as a function of muon p_{T} in the barrel (left) and endcap (right). The results estimated by the template fitting (nominal method) and ratio method (alternative method for systematic uncertainty) are presented.

To estimate the backgrounds with two misidentified prompt muons (QCD dijets), the data events with two leptons failing the isolation requirement are selected and weights are applied based on fake rate per muons (fake rate / 1-fake rate) to convert the number of events from the fake dominant region (two muons failing isolation requirement) to the signal region (two muons passing isolation requirement). Small contamination by electroweak processes are subtracted by MC simulation.

For the backgrounds with only one misidentified prompt muons (W+jets),

the procedure is similar with QCD dijet case. The difference is that the control data sample requires only 1 muon failing isolation, not 2 muons. The weight is also applied only 1 muon (failing isolation requirement) per event. However, as the control data sample includes 1 muon passing isolation requirement, the contribution from the electroweak processes is larger than QCD dijet case and the simple subtraction of them by MC simulation doesn't work. To subtract the contribution properly, a template fitting is performed on the dilepton mass distribution. The template shapes for the electroweak processes are obtained from MC simulation. For W+jet template, the shape of the distribution obtained from the data with same sign requirement between two muons are used after subtracting other contributions by MC simulation. The QCD template, obtained in the data driven way as discussed above, is also considered in the template fitting to avoid double counting.

The estimated dilepton mass distribution from QCD and W+jets by the fake rate method is shown in Fig. 5.8.

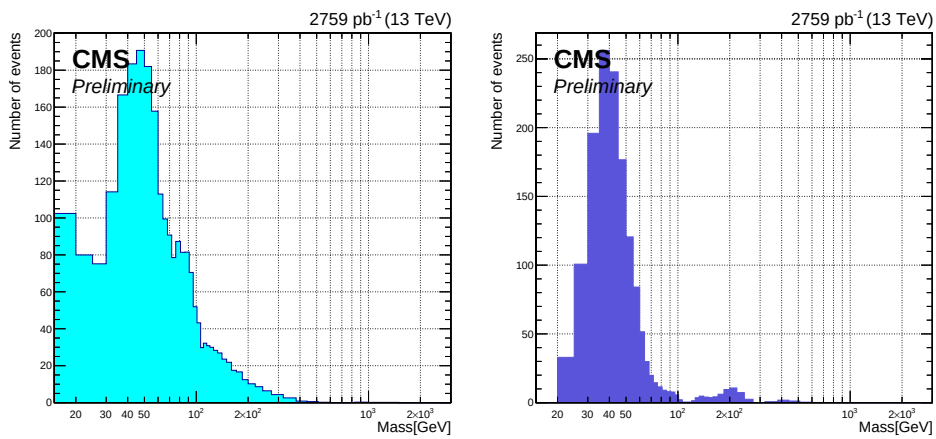

Figure 5.8: The dilepton mass distribution from QCD (left) and W+jet (right) events estimated by fake rate method.

MC prediction

The minor backgrounds not considered in data driven methods (WZ and ZZ) are estimated by MC simulation after taking into account the efficiency scale factor. The dilepton mass distribution from the two processes normalized to the integrated luminosity of the data are shown in Fig.5.9.

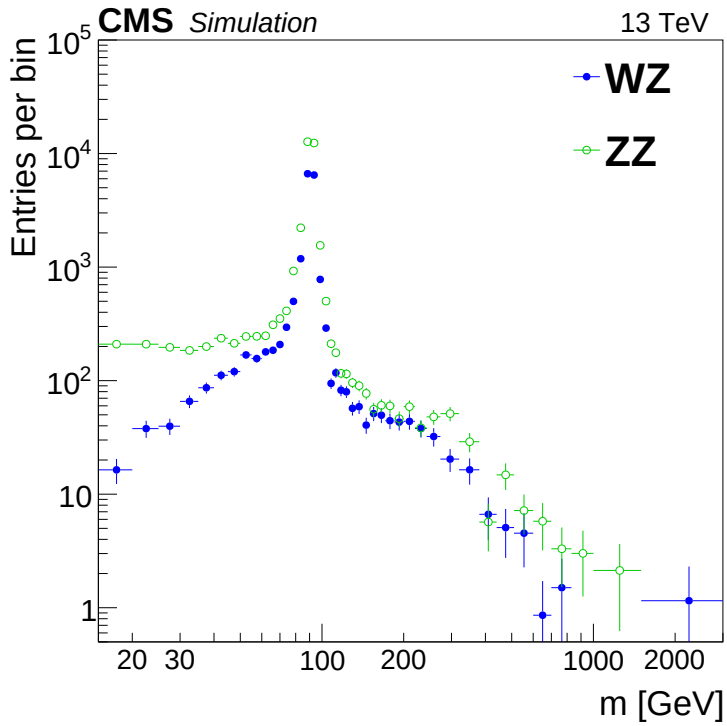

Figure 5.9: The dilepton mass distribution of the backgrounds estimated by MC simulation (WZ and ZZ). The efficiency scale factor is applied, and the distribution is normalized to the integrated luminosity of the data.

5.5.2 Dielectron channel

The background estimation in the dielectron channel is quite similar with dimuon channel as the estimation method is universal for muon and elec-

tron case. The background processes with two true electrons ($t\bar{t}$, tW and $\bar{t}W$, WW and $Z/\gamma^* \to \tau\tau$) are estimated by eμ method, and the other backgrounds with misidentified electrons (W+jets and QCD) are estimated by fake rate method. MC simulation is used to estimate small remaining backgrounds (WZ and ZZ).

eμ method

The basic idea is exactly same with the dimuon channel, which uses the branching fraction of the ee to $e\mu$ final state. To obtain the $e\mu$ data distribution, the data sample is collected by the trigger with an electron with $p_{\mathrm{T}} > 17\,\mathrm{GeV}$ satisfying a loose identification and isolation criteria and an isolated muon with $p_{\mathrm{T}} > 8\,\mathrm{GeV}$. The p_{T} criteria on the offline reconstructed leptons are 25 and 15 GeV for electron and muon respectively to ensure to be in the plateau region of the trigger efficiency. Similar event selection is used with the dielectron channel but switching an electron to a muon with a tight identification criteria [38] and and requirement on the particle flow based isolation.

The dilepton mass distribution in eμ final state is shown in Fig. 5.10. Data and MC simulation agrees well within a few % in general.

The eμ dilepton mass distribution is converted to the distribution in the dielectron channel using the branching fraction (5.3) and Fig. 5.11 shows the estimated distribution with the comparison to MC simulation. The difference with the simulation is assigned as the systematic uncertainty on the estimated number of backgrounds as same with the dimuon channel.

fake rate method

To estimate the backgrounds with objects misidentified as electron (QCD and W+jets), fake rate method is used as same with dimuon channel. In the di-

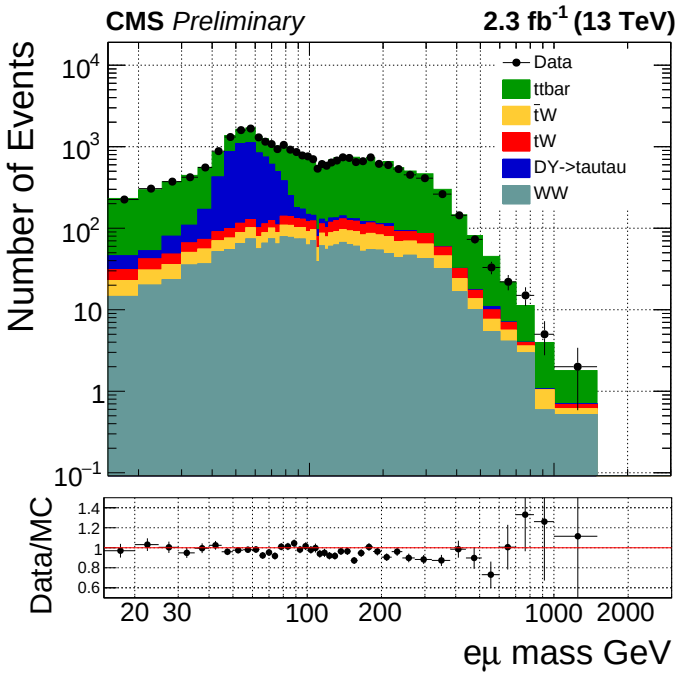

Figure 5.10: eμ dilepton mass distribution for the background estimation by eμ method in the dielectron channel.

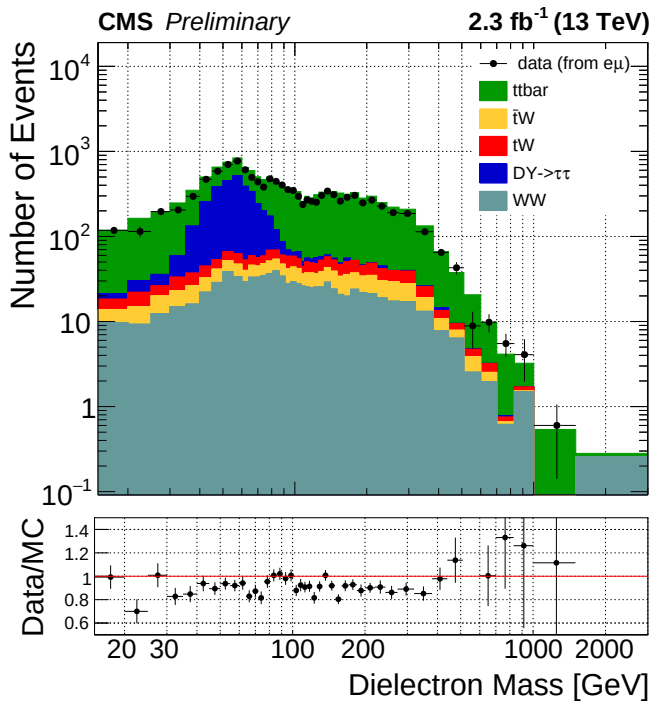

Figure 5.11: The background events estimated by eμ method in the dielectron channel (black dots) with the comparison to MC simulation.

electron channel, the major contribution of the misidentified electron comes from a jet (with electromagnatic energy deposit in ECAL), and therefore the definition of the fake rate is slightly different with the dimuon channel, which is the probability of a jet passing the electron identification criteria used in the analysis. To estimate the fake rate, a data sample collected by single photon triggers is used. To reduce the contamination from electroweak processes, no more than 1 electron satisfying the electron identification criteria is allowed (to reject Z/γ^* process) and the missing transverse energy should be smaller than 20 GeV (to reject W+jets). A few more requirements are imposed to reject events with true photons. Remaining small contamination by electroweak processes are subtracted by MC simulation.

The estimated fake rate is shown in Fig. 5.12 as a function of electron p_{T} in the barrel and endcap region respectively.

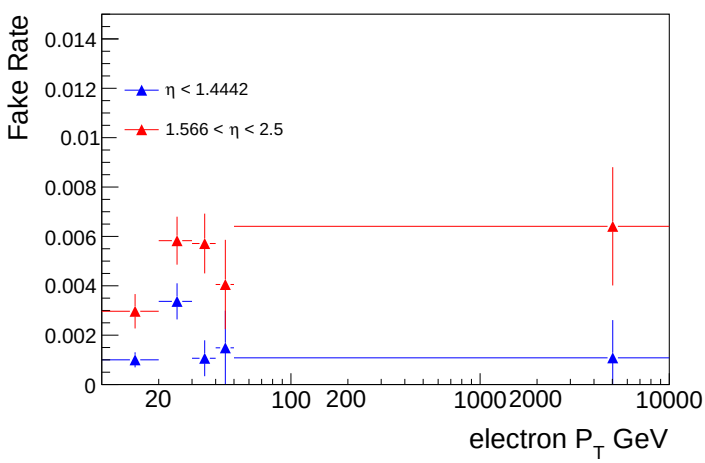

Figure 5.12: Electron fake rate as a function of electron p_{T} in the barrel and endcap.

Based on the fake rate, the backgrounds with two misidentified electrons

(from QCD dijet) are estimated by applying weights per electrons on top of the data sample collected with two electrons failing the electron identification criteria used in the dielectron channel. Similarly, the backgrounds with one prompt electron and one misidentified electron (from W+jets) are estimated using another data control sample with 1 passing and 1 failing electrons for the identification criteria. In both cases, the contamination from electroweak process in the data control samples is subtracted by MC simulation.

The estimated QCD and W+jets background events are shown in Fig. 5.13.

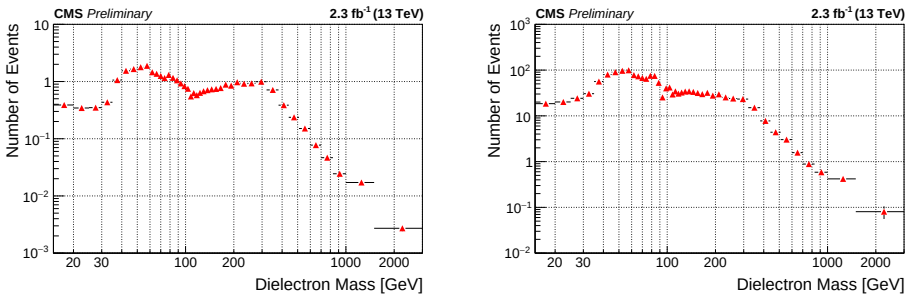

Figure 5.13: The dilepton mass distribution estimated by the fake rate method for QCD (left) and W+jets (right) processes.

MC prediction

Remaining backgrounds not estimated by data driven methods (WZ and ZZ) have small contribution compared to the other backgrounds. They are estimated by MC simulation same as the dimuon channel, and Fig. 5.14 shows their dielectron mass distribution. Efficiency scale factor is applied.

The dilepton mass distributions with estimated backgrounds in each channel are shown in Fig. 5.15 and the fraction of the background events with respect to the total data events is presented in Fig. 5.16 as a function of dilepton mass. The DY events dominates over the entire mass range in both channels.

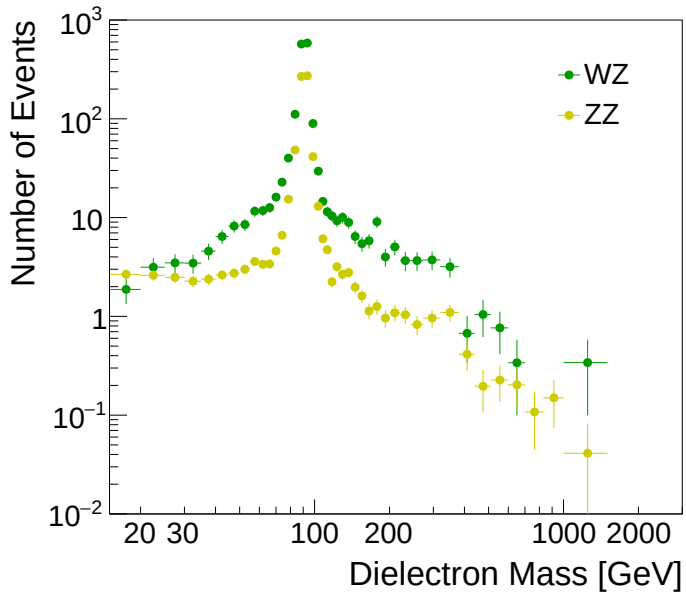

Figure 5.14: The dielectron mass distribution for the background events estimated by MC simulation. Efficiency scale factor is applied, and the distribution is normalized to the integrated luminosity of the data.

The dominant backgrounds is top-quark processes ($t\bar{t}$, tW and $\bar{t}W$) whose fraction goes up to about 30% above Z peak region. The contribution from misidentification (QCD and W+jets) and Electroweak processes ($Z/\gamma^* \rightarrow \tau\tau$ and diboson processes) is prominent in the low mass region below Z peak. Overall, the prediction described the data well within 10% level in most of the mass range except for the high mass region with statistical fluctuations.

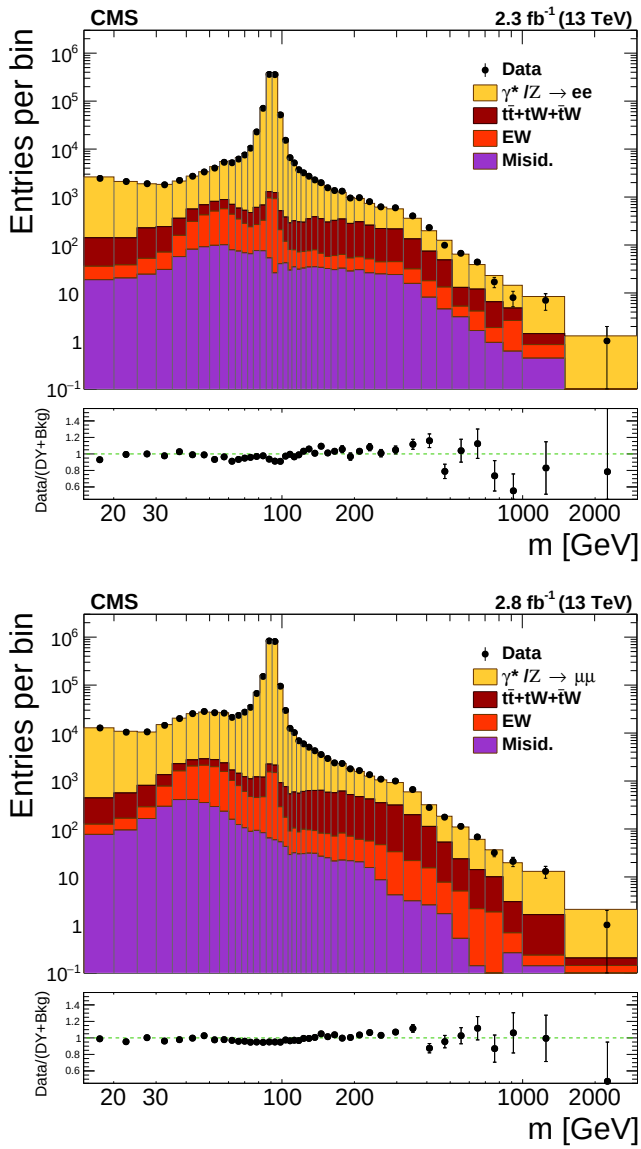

Figure 5.15: The dilepton mass distributions of the data compared to the predicted number of signal and backgrounds in dielectron (top) and dimuon channel (bottom). The data is presented as black dots, and filled colors are the predictions from data driven method or MC simulation.

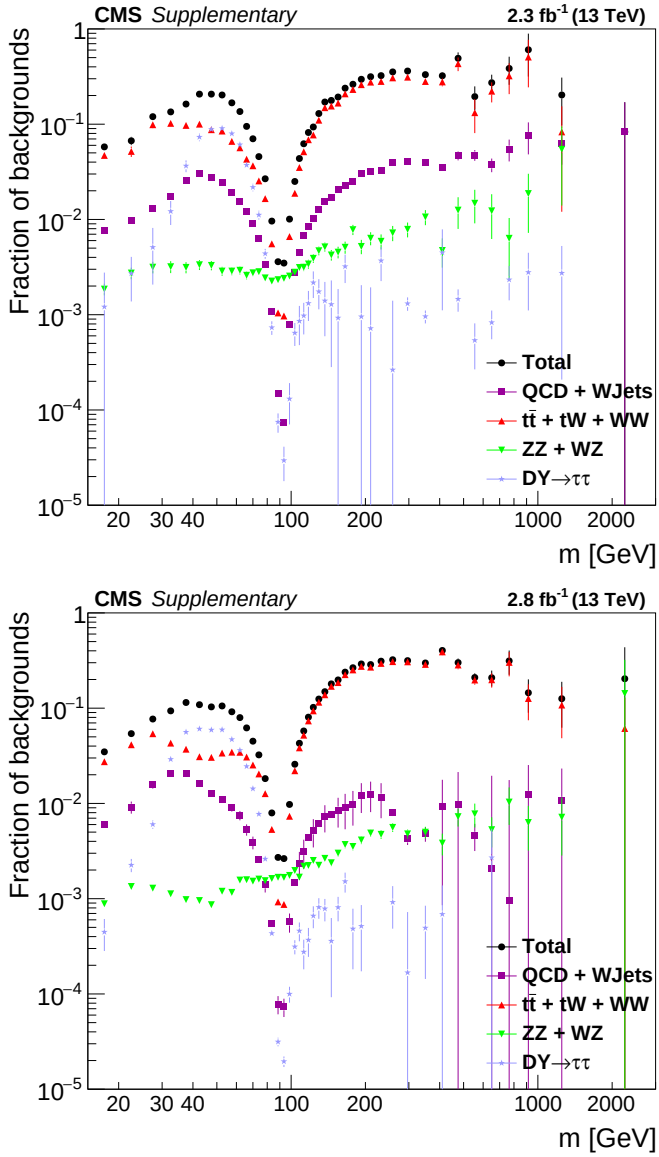

Figure 5.16: The fraction of the number of estimated background events with respect to the total number of data events observed per mass bin in the di-electron (top) and dimuon (bottom) channels. Black color is the total number of backgrounds, and the other colors presents the contribution from individual background processes.

Chapter 6

Corrections

6.1 Unfolding for the detector resolution

The resolution of dilepton mass leads the migration between mass bins. The migration effect becomes large depending on the relative size of the mass bin with respect to the mass resolution. The migration effect should be corrected to obtain the differential cross section without the detector effect. It is performed by unfolding technique, which "unfold" the observed distribution to the true dilepton distribution using the information of the map between true and reconstructed dilepton mass so called response matrix.

The i, k component of response matrix T_{ik} used in the analysis is defined as the fraction of the number of events in kth bin of the true lepton distribution after FSR effect ($N_{\text{true},k}$) but moves to ith bin in the reconstructed distribution ($N_{\text{reco.},i}$) such that

$$N_{\text{reco.},i} = \sum_k T_{ik} N_{\text{true},k}. \tag{6.1}$$

i and k is always identical in the ideal resolution scenario, but in the realistic case, there are some $i \neq k$ components (off-diagonal terms) that mean the bin migration from ith bin to kth bin.

The response matrices from DY MC simulation for dimuon and dielectron channel are presented in Fig. 6.1.

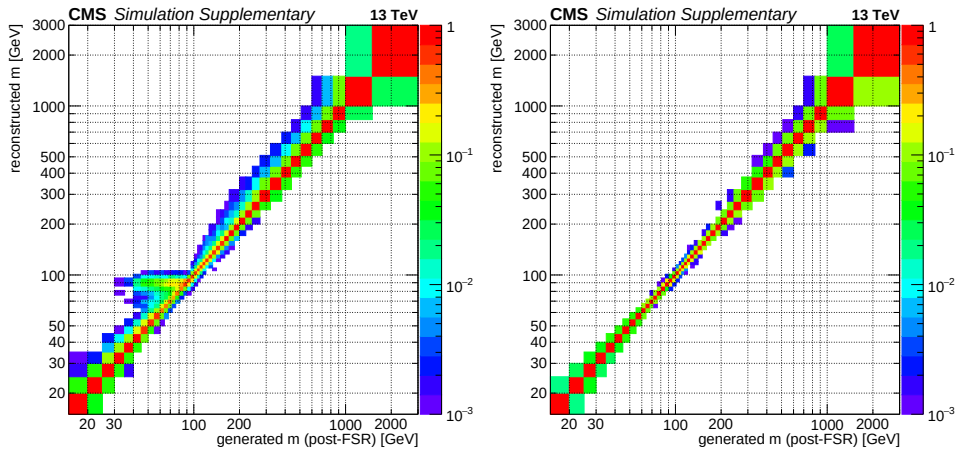

Figure 6.1: Response matrix for the detector resolution in the dielectron (left) and dimuon channel (right).

In both channels, most of the events (about 90%) are placed in the diagonal terms in general. The migration effect is prominent near Z peak region due to small size of the bins (4-5 GeV). The reason of larger migration in the dielectron channel than the dimuon channel is larger FSR effect of electron.

The true dilepton distribution is obtained by using iterative D'Agostini method [70] with the response matrices.

6.2 Acceptance and efficiency

Some of DY events produced in pp collision are lost in the detection procedure due to the kinematic and geometrical acceptance of the detector or the recon-

struction the identification procedure. To compensate the lost signal events, the correction factors called Acceptance (A) and Efficiency (ϵ) defined in 6.2 are caclulated:

$$A \times \epsilon \equiv \frac{N^A}{N^{\text{gen}}} \cdot \frac{N^\epsilon}{N^A} = \frac{N^\epsilon}{N^{\text{gen}}} \tag{6.2}$$

where N^{gen} is the number of total generated signal events, N^A is the number of events satisfying the acceptance criteria (p_{T} and η requirement), and N^ϵ is the number of reconstructed events passing all event selection criteria.

The acceptance and efficiency are estimated by DY MC simulation for each mass bin as shown in Fig.6.2.

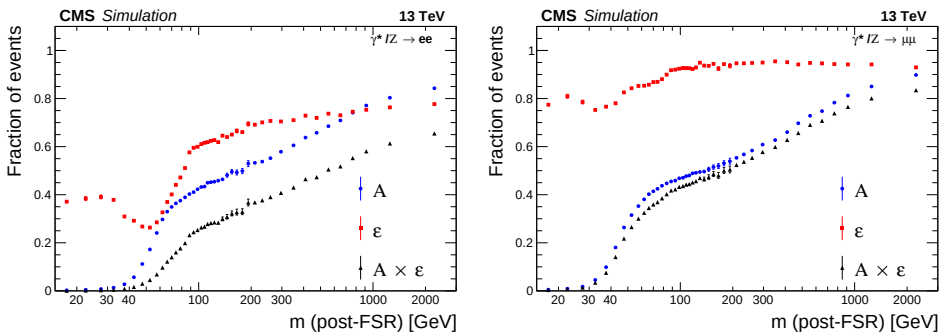

Figure 6.2: Acceptance and efficiency as a function of dilepton mass in the dielectron (left) and dimuon (right) channel. The blue and red color correspond to the acceptance and efficiency, repectively. Their multiplication is presented as black color.

In both channels, the acceptance is quite small below 1% in the lowest mass bin due to p_{T} requirements on each lepton, but it gradually increases in higher mass region up to about 80%. The efficiency is from 30 to 70% for the dielectron channel and 80 to 90% for the dimuon channel.

6.3 Efficiency scale factor

The efficiency shown in Fig. 6.2 is estimated by MC simulation, but the lepton reconstruction, identification and trigger efficiency can be different between simulation and data. Therefore, the efficiency scale factor, the ratio of the efficiency of the data to MC, is applied to correct the difference of the efficiency. To obtain the lepton efficiencies from simulation and data used for the scale factor, the "tag-and-probe method" [28] is used.

In the method, dilepton events with their invariant mass near Z boson is selected if a lepton satisfies a tight identification criteria ("tag"). The dilepton mass distribution is split into two parts depending on whether the lepton on the other side ("probe") satisfies a given criteria or not. Each distribution is fit to obtain the number of probe leptons after subtracting backgrounds not coming from Z boson, and the efficiency of the criteria is estimated by the fraction of the number of probes satisfying the criteria with respect to the total number of probes.

To take into account the dependence of the efficiency with respect to the kinematics of the leptons, the efficiency is parametrized in p_{T} and η of the leptons. The single lepton efficiency is independently measured in each step (reconstruction and identification including isolation) and the overall efficiency of dilepton events is computed by multiplying all efficiencies as shown below:

$$\varepsilon_{\text{event}} = \varepsilon_{\ell_1} \times \varepsilon_{\ell_2} \times \varepsilon_{\text{event, trig}} \tag{6.3}$$

where $\varepsilon_{\ell_{1,2}}$ are the efficiency of single leptons in a dilepton event and $\varepsilon_{\text{event, trig}}$ the event efficiency for the trigger taking into account the probability that either of two leptons can trigger the event [49, 50]. The detail procedure and value of the tag-and-probe efficiency as a function of lepton p_{T}

and η are shown in Section A.

The conversion of the efficiency scale factor per event ($\varepsilon_{\text{event,data}}/\varepsilon_{\text{event,MC}}$) to the scale factor per mass bin for the cross section in (5.2) is done by recomputing the efficiency as a function of dilepton mass after applying the scale factor per event with simulation. The ratio of the efficiency with and without efficiency scale factor per mass bin is used as the scale factor per mass bin.

The efficiency scale factor per dilepton mass bin is shown in Fig. 6.3 in each channel. There are two scale factor results for the dimuon channel because the data efficiency is measured separately after splitting the dataset into two parts with resepct to an update in the isolation algorithm of the trigger. The amount of the data before (HLT menu version 4.2) and after update (version 4.3) is $843\,pb^{-1}$ and $1916\,pb^{-1}$ respectively. After the update, the trigger efficiency increased especially near the the p_{T} threshold of the trigger (20 GeV) and it leads better agreement with MC. This is the reason why the efficiency scale factor per mass bin changed from about 93% to 96% below Z peak region after the update, but there is almost no impact in the higher mass region. On the other hand, the scale factor for the dielectron channel is around 96% in general.

6.4 Unfolding correction for final state radiation effect

The leptons can emit photons by FSR, which can shift the observed dilepton mass to a lower value due to lost momentum carried by photons. The bin migration due to the shift should be corrected to combine two channels as the FSR effect is diffent for e and μ. it also makes easier to compare with the theoretical prediction.

As a representative of leptons with the compensation of lost momentum,

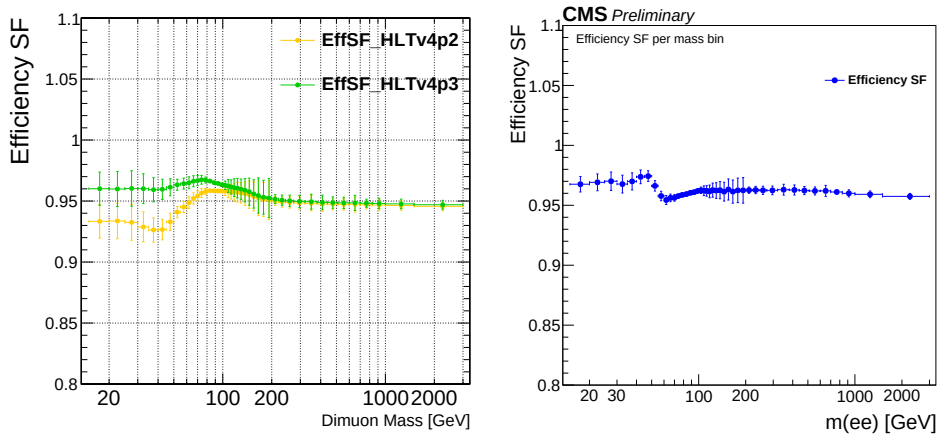

Figure 6.3: The efficiency scale factor per dilepton mass bin for the dimuon channel (left) and dielectron channel (right).

"dressed lepton" concept is used. The momentum of dressed lepton is defined by adding momentum of photons near the lepton after FSR effect (post–FSR) within $\Delta R(\ell, \gamma) < 0.1$ to the momentum of the post–FSR lepton itself:

$$p_\ell^{\text{dressed}} = p_\ell^{\text{post–FSR}} + \sum_{\Delta R<0.1} p_\gamma \tag{6.4}$$

To correct the effect, another unfolding procedure is performed to unfold post FSR distribution to the distribution with dressed lepton. The response matrices from DY MC simulation is shown in Fig. 6.4.

The off-diagonal terms are placed in the lower side with respect to the diagonal term as the FSR effect always makes the dilepton mass lower. The migration is larger in the dielectron channel due to larger FSR effect of electron.

The dressed distribution is obtained by using iterative D'Agostini method [70] again for the dielectron channel and simple matrix inversion for the dimuon channel, with the response matrices.

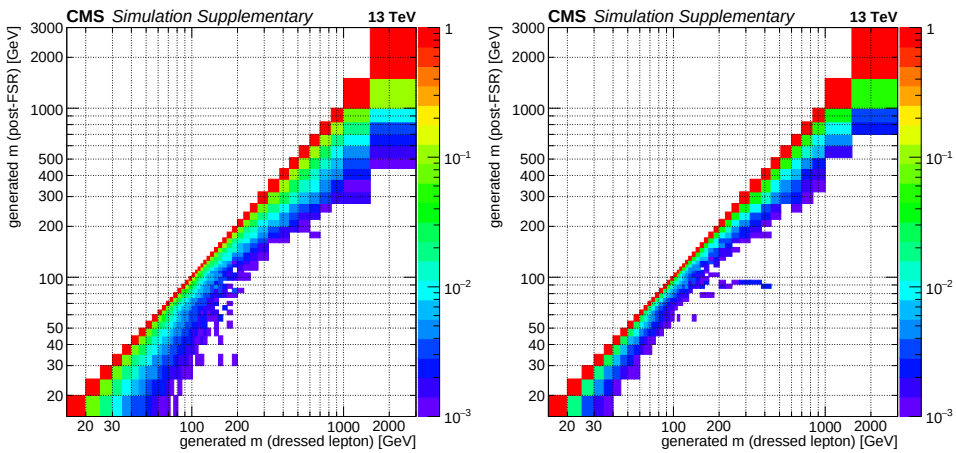

Figure 6.4: Response matrix for FSR effect in the dielectron (left) and dimuon channel (right).

Chapter 7

Systematic uncertainties

In the chapter, the methods to estimate the systematic uncertainty is discussed for each source, following the order of analysis procedure.

7.1 Background estimation

The uncertainty sources are different for the backgrounds estimated by data-driven technique (eμ method and fake rate method) and MC simulation. For the data-driven backgrounds, two uncertainty sources are taken into account:

1. Statistical uncertainty due to the limited statistics of the data used (treated as systematic)

2. Difference between data-driven estimation and MC simulation

The first source is the uncertainty on the estimated backgrounds propagated from the statistical uncertainty in the eμ data control sample in the case of the backgrounds estimated by $e\mu$ method. For the ones from fake rate method, the uncertainty propagated from the statistical uncertainty on the

fake rate itself is used. In addition, the difference of the fake rate between template fitting and ratio method is also considered.

For the backgrounds from MC simulation, below sources are considered:

1. Statistical uncertainty due to the limited statistics of MC simulation (treated as systematic)

2. Uncertainty of the cross section used for the normalization to the integrated luminosity of the data

To convert the uncertainty on the number of the background events to the uncertainty on the cross section, a dedicated method is used instead of simple uncertainty propagation bin by bin, to take into account the correlation between bins. For a given background process, 1000 background histograms are made by randomizing the number of background events within the uncertainty assigned to each mass bin, and 1000 smeared cross section results are computed from each randomized background histogram. The standard deviation of the gaussian fit to the distribution of the relative difference between the nominal cross section and the smeared cross sections is assigned as the uncertainty on the cross section per mass bin. The final uncertainty from the background estimation is calculated by the quadrature sum of the uncertainties from each background process.

7.2 Detector resolution

The uncertainty on the detector resolution is composed of two sources: uncertainty from the electron (muon) energy (momentum) scale correction and the uncertainty from the unfolding for the detector resolution.

7.2.1 Muon momentum scale correction

The muon momentum scale correction, separately applied for the simulation and data, has its uncertainty originated from its derivation procedure [68]. To estimate the uncertainty on the cross section, the method used in the background estimation is used. In the case of MC correction, the correction is smeared within its uncertainty and 500 response matrices for the detector resolution unfolding are computed with the smeared corrections. 500 smeared cross sections are obtained from each response matrix, and the standard deviation of the relative difference distribution between the nominal cross section and smeared cross sections is assigned as the uncertainty per mass bin. For the data correction, the procedure is same but computes the dimuon mass distribution of the data instead of the response matrix. The final uncertainty from the correction is computed by the quadrature sum of the uncertainties from MC and data corrections.

7.2.2 Electron energy scale and smearing correction

The uncertainty is estimated in the way similar with the muon momentum scale correction. The corrections for the electron energy scale and resolution is smeared within its uncertainty and 100 response matrices are produced with the smeared correction. 100 cross sections are produced by propagating the response matrices, and the standard deviation of the relative difference distribution between the cross sections with and without smearing is assigned as the uncertainty.

7.2.3 Unfolding for the detector resolution

The two sources are considered for the uncertainty from the unfolding correction:

1. Statistical uncertainty due to the limited statistics of the MC simulation used in computing the response matrix

2. Dependence on MC modeling

The second source is estimated by taking the difference with the cross section results computed from another response matrix computed with an alternative MC generator. In the dimuon channel, the MC simulation generated by Madgraph at LO (dimuon mass $< 50\,\text{GeV}$) and POWHEG (dimuon mass $> 50\,\text{GeV}$) is used as the alternative generator. In the dielectron channel, the main signal sample (MADGRAPH5_aMC@NLO) is reweighted with the distribution from FEWZ and used to produce different response matrix.

7.3 Acceptance and PDF

The uncertainty on the acceptance and PDF comes from theoretical sources. The 3 uncertainty sources are considered below:

1. Imperfect knowledge on PDF

2. Dependence on the strong coupling constant α_S

3. Effect of higher order corrections on the acceptance

The first source is estimated by FEWZ using the error sets in NNPDF 3.0 at NNLO accuracy. For the second source, the acceptance is recomputed using the PDF set with $\alpha_S = 0.117$ $\alpha_S = 0.119$ which are deviated from the central α_S value (0.118). The maximum difference of the acceptance with the nominal value is assigned as the uncertainty from α_S. To estimate the uncertainty from the last source, the acceptance with NNLO prediction is computed using FEWZ package. The difference between the nominal value (estimated by

MadGraph5_aMC@NLO DY sample at NLO accuracy) and NNLO value is assigned as the uncertainty bin by bin. To avoid statistical fluctuations, each acceptance shape as a function of dilepton mass is fit and the difference is taken from the fit functions.

The final uncertainty from the acceptance and PDF are computed by the quadrature sum of the uncertainties from all sources.

7.4 Efficiency scale factor

The uncertainty from the efficiency scale factor comes from the uncertainty on the tag-and-probe efficiency measurement. In the dimuon channel, below sources are considered for the tag-and-probe efficiency:

- Statistical uncertainty on the efficiency (treated as systematic)
- Alternative signal and background shape
- Alternative mass range
- Alternative number of mass bins
- Alternative p_{T} requirement on tag muons (that controls the level of backgrounds in tag and probe mass distribution)
- Alternative p_{T}–η bins

Similarly, dielectron channel considered below sources for the tag-and-probe efficiency:

- Statistical uncertainty on the efficiency (treated as systematic)
- Alternative signal and background shape
- Alternative p_{T} requirement on tag electrons

- Alternative MC sample (for MC efficiency only)

In both channels, the uncertainty coming from alternative signal and background shape is dominant in most of p_{T}–η bins.

To propagate the uncertainty on the tag-and-probe efficiency to the uncertainty on the cross section, randomized maps are used as the similar approach for the estimation of the uncertainty from the background estimation or scale corrections. For a given uncertainty source, 500 p_{T}–η randomized efficiency maps are produced by smearing the nominal efficiencies within the uncertainty. Each randomized map is used to calcuate the efficiency scale factor and the final cross section. The standard deviation of the relative difference between the nominal value and alternative values from the randomized efficiency maps are assigned as the uncertainty on the cross section from the given uncertainty. The final uncertianty from the efficiency scale factor on the cross section is the quadrature sum of all uncertianties from each source.

7.5 FSR

The uncertainty source is same with the unfolding correction for the detector resolution as both of them are based on the unfolding technique. To estimate the uncertainty from MC modeling, the different generator for FSR effect with PYTHIA is chosen, PHOTOS 3.56 [71]. The difference with the cross section from the response matrix based on PHOTOS sample is assigned as the uncertainty.

7.6 Integrated luminosity

The integrated luminosity was mainly masured using the pixel detector with Pixel Cluster Counting (PCC) method. The absolute calibrations were performed by Van der Meer Scan (VdM). The luminosity uncertainty includes

the uncertainty sources from PCC and VdM and the size of the uncertainty is 2.3% [72].

The uncertainty on the cross section is shown for each source in Fig. 7.1 in both channels. The tables with exact numbers are available in Section B.

In general, the systematic uncertainty is dominant below dilepton mass $< 400\,\text{GeV}$. In the low mass region below Z peak, the dominant uncertainty source is Acceptance+PDF that goes up to about 10% due to the large impact of higher order corrections on the acceptance in this region. Experimentally, the uncertainty from the efficiency scale factor is dominant with 2–3% level in both channels. Near Z peak region, the total systematic uncertainty goes down to the similar level of luminosity uncertainty. In the higher mass region, the uncertainty from the background estimation starts to dominant with the statistical uncertainty due to the lack of statistics in the data.

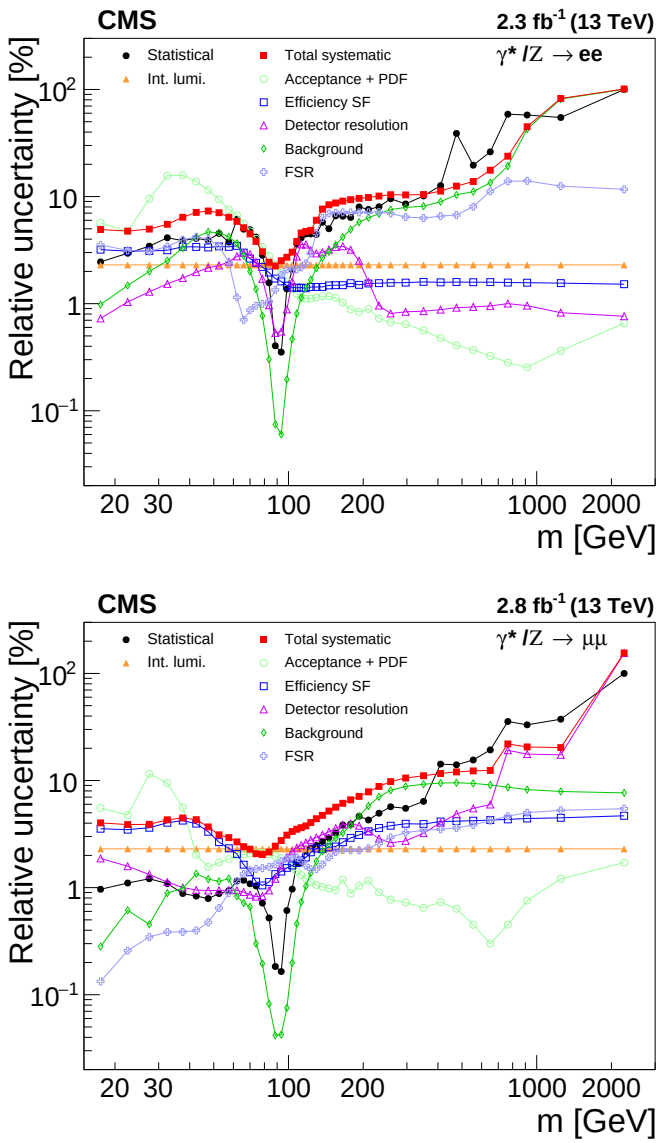

Figure 7.1: The uncertainty on the differential cross section per each source in the dielectron (top) and dimuon (bottom) channels. "Total systematic" represents the quadrature sum of all uncertainties except for statistical, luminosity and acceptance+PDF. The tables with exact numbers are available in Section B.

Chapter 8

Results

8.1 Results from individual channels

The differential DY cross section $d\sigma/dm$ with all corrections is presented in Fig. 8.1. The experimental result is compared to theoretical predictions based on NNPDF 3.0 PDF set by MadGraph5_aMC@NLO at NLO accuracy and FEWZ at NNLO accuracy. The FEWZ prediction also includes higher order EW corrections (NLO). In general, the experimental result shows good agreement with the theoretical predictions within uncertainties. The cross section values in the dimuon and dielectron channels are summarized from the Table D.1 to D.4 in Section D.

In addition, the fiducial cross sections without acceptance and FSR corrections are also measured. Without them, the theoretical input to the measurement is minimized and the uncertainty associated to the result is reduced. The result is shown in Fig. 8.2 with the comparison to the theoretical prediction by MadGraph5_aMC@NLO. The difference with the result in the full phase space

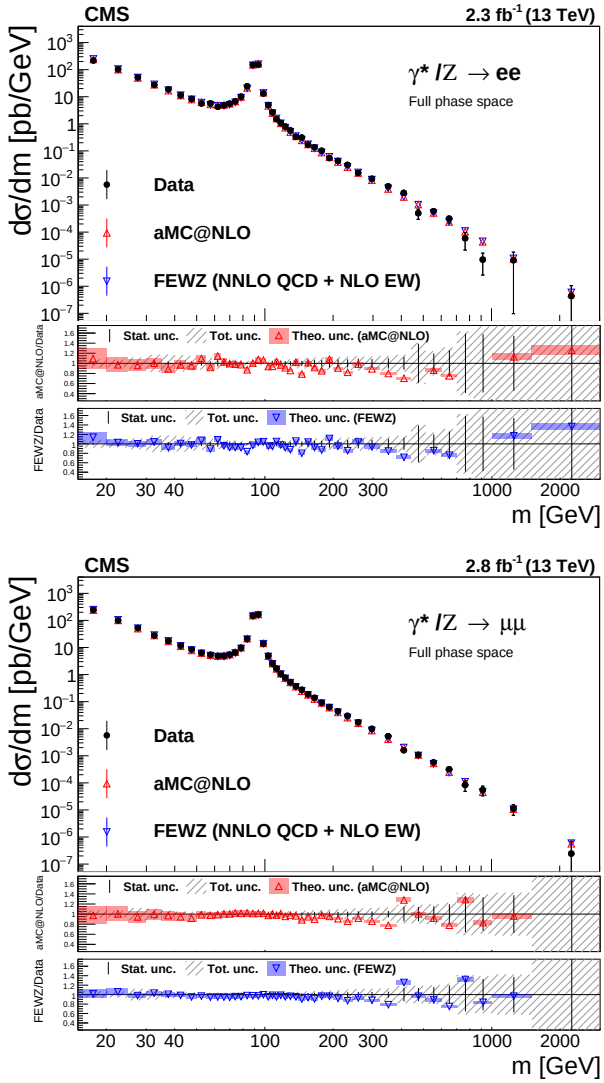

Figure 8.1: The differential DY cross section $d\sigma/dm$ in the full phase space with FSR correction from dielectron (top) and dimuon channel (bottom). The experimental result is shown in black color, and it is compared to the theoretical predictions by MadGraph5_aMC@NLO at NLO accuracy (red) and FEWZ at NNLO QCD and NLO EW accuracy (blue). The ratio between theoretical prediction and experimental result is shown in the bottom panel.

(Fig. 8.1) is prominent in the low mass region where the acceptance correction is quite large as shown in Fig. 6.2. The data and theory have good agreement within uncertainties in general. Table D.5-D.6 and D.7-D.8 show the summary of the fiducial cross sections in the dimuon and dielectron channel respectively.

8.2 Combination between two channels

The differential cross sections in the dielectron and dimuon channel show good agreement each other and therefore the results are combined by exploiting the lepton universality to have higher precision. The combination of two channels is done by the same procedure used in [73]. The central value of the combined result per mass bin is determined by the average of the cross sections in each channel weighted by the inverse of squared associated uncertainty. The weighted mean makes the combined result closer to the measurement with lower uncertainty between two channels. The uncertainty associated to the combined result is extracted from the diagonal elements of the covariance matrix for the combined result, which is constructed using the covariance matrices of individual channels and the weights used in the combination of the central value. The details on the treatment of the correlation and the estimation of the covariance matrices can be found in Section C.

The differential cross section of the combined results is shown in Fig. 8.3 with the comparison to the theoretical prediction by FEWZ. The summary of the combined result is shown in Table D.9-D.10. The abscissas of the data points are adjusted using the Eq. (6) in Ref. [74]. Fig. 8.4 shows the magnified ratio between the combined result and the theoretical prediction for low ($m < 200\,\mathrm{GeV}$) and high ($m > 200\,\mathrm{GeV}$) mass region. The theoretical prediction taking into account the photon induced contribution is calculated by FEWZ with the LUXqed PDF set and added in the comparison for the high mass

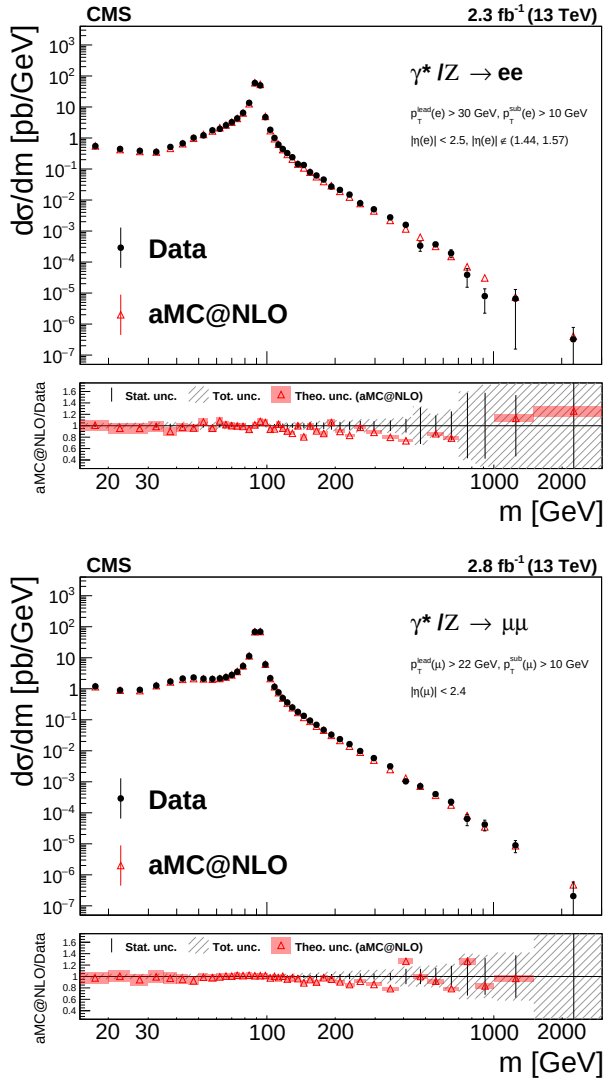

Figure 8.2: The differential DY cross section $d\sigma/dm$ in the fiducial region without FSR correction from dielectron (top) and dimuon channel (bottom). The experimental result is shown in black color, and it is compared to the theoretical prediction by MadGraph5_aMC@NLO at NLO accuracy (red) The ratio between theoretical prediction and experimental result is shown in the bottom panel.

region where contribution from the photon induced process is expected to be high. In general, the experimental results show good agreement with the theoretical prediction.

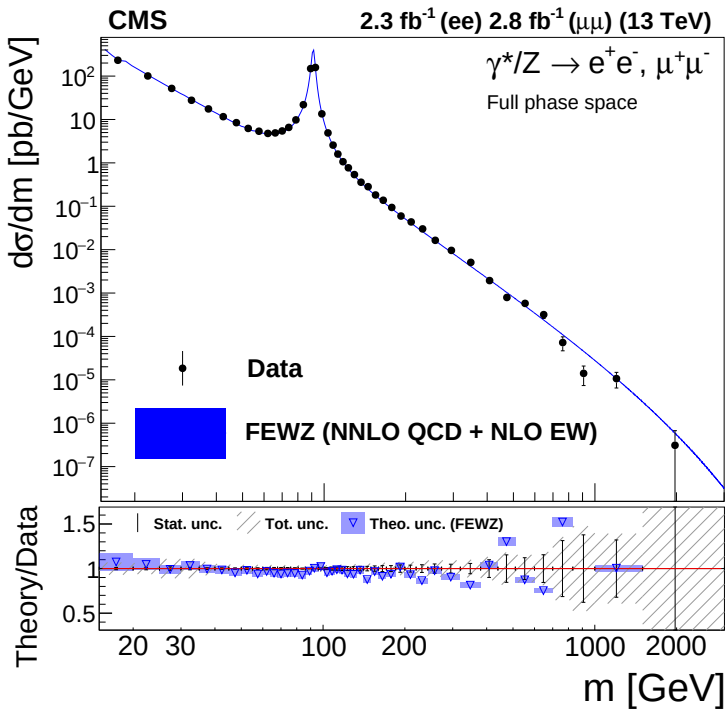

Figure 8.3: The differential cross section $d\sigma/dm$ by the combination between two channels. The result is compared to the theoretical prediction by FEWZ at NNLO QCD and NLO EW accuracy with the NNPDF 3.0 PDF set.

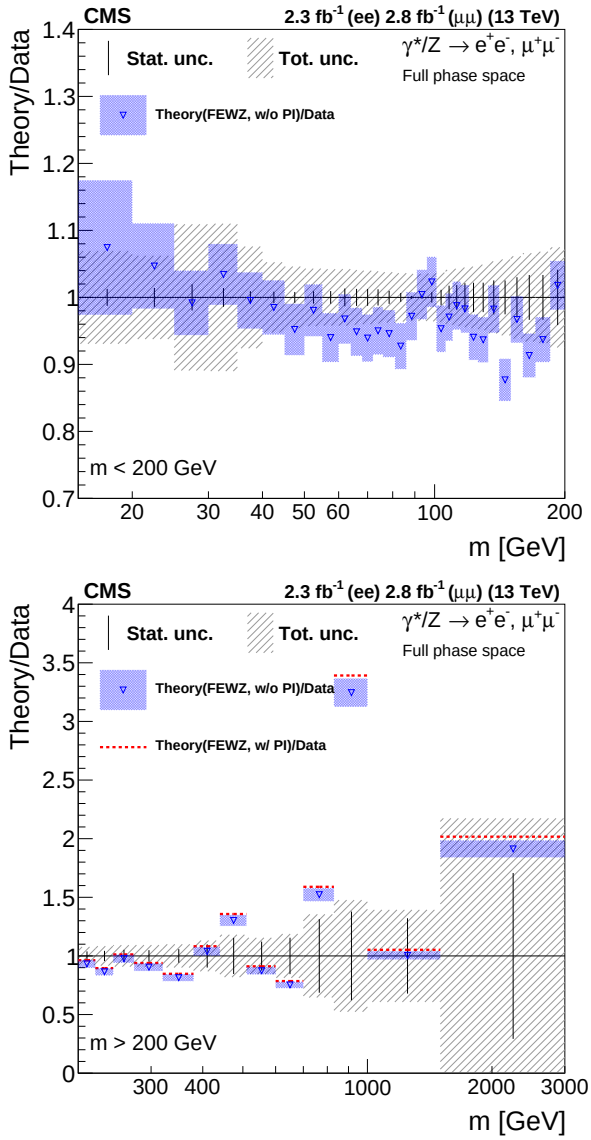

Figure 8.4: The magnified ratio between experimental result and the theoretical prediction shown in the bottom panel of Fig. 8.3 for the mass range below (left) and above (right) 200 GeV. The additional prediction for the photon induced contribution by FEWZ with LUXqed PDF set on top of DY is added in the high mass region as the red color.

Chapter 9

Summary and Conclusion

The standard model (SM) is one of the most successful theories to describe the physics of the fundamental particles and their interactions. The recent and famous triumph of the SM is the discovery of Higgs bosons by LHC experiments in 2012, which was predicted in 1960s to explain the mass of the fundamental particles. However, still there are many open questions not explained by the SM including the dark matter, the non-zero neutrino mass, asymmetry of matter and anti-matter, and so on.

Therefore, precise measurements of physics quantities predicted by the SM are considered as one of the important physics programs for the modern particle physics to test the validity of the SM. In addition, the precise understanding of the SM is the basis of the searches for new physics beyond the SM (BSM) that could explain the unsolved problems. In particular, the information on the proton structure, encoded in the parton distribution function (PDF), is essential to interpret the data from the hadron collider experiments at the frontier for BSM searches. However, the PDFs cannot be computed in a

perturbative quantum chromodynamics (QCD) and therefore it is determined in a global QCD analysis by fitting many experimental data provided from various precision measurements.

In this context, the measurement of the differential Drell-Yan (DY) cross section with respect to the dilepton mass $d\sigma/dm$ is performed. The cross section is theoretically well understood up to next-to-next-to-leading order (NNLO) in perturbative QCD, and experimentally its cross section can be precisely measured thanks to the high efficiency and resolution of leptons in the final state. Therefore, the measurement can provide the precise test of the SM. For PDF, the measurement in the mass region up to Z resonance can provide complementary information of the quark distribution as well as gluon via higher order effect from perturbative QCD, and the result in the high mass region is expected to contribute to the constraint of the light anti-quark distribution. The improvement of the sensitivity to new physics searches with lepton final state is also expected as the DY process is one of the major backgrounds in such analyses.

The differential cross sections are measured over a wide dilepton mass range from 15 GeV to 3000 GeV divided by 43 bins in the dimuon and dielectron channels. They are based on the proton-proton collisions at the center of mass energy of 13 TeV collected by the Compact Muon Solenoid detector at Large Hadron Collider, and the corresponding integrated luminosity is 2.3 (2.8)fb^{-1} for the dimuon (dielectron) channel. The results in the individual channels are corrected up to the full phase space with the final state radiation (FSR) effect taken into account. The other results without acceptance and FSR correction, which minimize the theoretical inputs and have lower uncertainty, are also presented. To achieve better precision, the full phase space results in two channels are combined after taking into account the correlation between channels and

measurement bins. The presented results are compared to the NLO and NNLO predictions at perturbative QCD calculated by MadGraph5_aMC@NLO and FEWZ respectively with NNPDF 3.0 PDF, and the experimental result shows good agreement with the theoretical prediction within uncertainties.

Bibliography

[1] *Wikipedia: Standard Model*. https://en.wikipedia.org/wiki/Standard_Model. Accessed: 2020-06-27.

[2] F. Halzen and Alan D. Martin. *QUARKS AND LEPTONS: AN INTRODUCTORY COURSE IN MODERN PARTICLE PHYSICS*. Jan. 1984. ISBN: 978-0-471-88741-6.

[3] V. E. Barnes et al. "Observation of a Hyperon with Strangeness Minus Three". In: *Phys. Rev. Lett.* 12 (8 Feb. 1964), pp. 204–206. DOI: 10.1103/PhysRevLett.12.204.

[4] J. D. Bjorken. "Asymptotic Sum Rules at Infinite Momentum". In: *Phys. Rev.* 179 (5 Mar. 1969), pp. 1547–1553. DOI: 10.1103/PhysRev.179.1547.

[5] A. Bodek et al. "Comparisons of Deep-Inelastic $e-p$ and $e-n$ Cross Sections". In: *Phys. Rev. Lett.* 30 (21 May 1973), pp. 1087–1091. DOI: 10.1103/PhysRevLett.30.1087.

[6] D. J. Fox et al. "Early Tests of Scale Invariance in High-Energy Muon Scattering". In: *Phys. Rev. Lett.* 33 (25 Dec. 1974), pp. 1504–1507. DOI: 10.1103/PhysRevLett.33.1504.

[7] Jun Gao, Lucian Harland-Lang, and Juan Rojo. "The structure of the proton in the LHC precision era". In: *Physics Reports* 742 (2018). The Structure of the Proton in the LHC Precision Era, pp. 1–121. ISSN: 0370-1573. DOI: https://doi.org/10.1016/j.physrep.2018.03.002.

[8] G. Altarelli and G. Parisi. "Asymptotic freedom in parton language". In: *Nuclear Physics B* 126.2 (1977), pp. 298–318. ISSN: 0550-3213. DOI: https://doi.org/10.1016/0550-3213(77)90384-4.

[9] V.N. Gribov and L.N. Lipatov. "Deep inelastic e p scattering in perturbation theory". In: *Sov. J. Nucl. Phys.* 15 (1972), pp. 438–450.

[10] Yuri L. Dokshitzer. "Calculation of the Structure Functions for Deep Inelastic Scattering and e+ e- Annihilation by Perturbation Theory in Quantum Chromodynamics." In: *Sov. Phys. JETP* 46 (1977), pp. 641–653.

[11] L.N. Lipatov. "The parton model and perturbation theory". In: *Sov. J. Nucl. Phys.* 20 (1975), pp. 94–102.

[12] NNPDF Collaboration. "Parton distributions from high-precision collider data". In: *The European Physical Journal C* 77 (Oct. 2017). DOI: 10.1140/epjc/s10052-017-5199-5.

[13] Tie-Jiun Hou et al. "New CTEQ global analysis of quantum chromodynamics with high-precision data from the LHC". In: (Dec. 2019). arXiv: 1912.10053 [hep-ph].

[14] L.A. Harland-Lang et al. "Parton distributions in the LHC era: MMHT 2014 PDFs". In: *Eur. Phys. J. C* 75.5 (2015), p. 204. DOI: 10.1140/epjc/s10052-015-3397-6. arXiv: 1412.3989 [hep-ph].

[15] S. Alekhin, J. Blumlein, and S. Moch. "The ABM parton distributions tuned to LHC data". In: *Phys. Rev. D* 89.5 (2014), p. 054028. DOI: 10.1103/PhysRevD.89.054028. arXiv: 1310.3059 [hep-ph].

[16] Jorge G. Morfin and Wu-Ki Tung. "Parton distributions from a global QCD analysis of deep inelastic scattering and lepton pair production". In: *Z. Phys. C* 52 (1991), pp. 13–30. DOI: 10.1007/BF01412323.

[17] Sayipjamal Dulat et al. "New parton distribution functions from a global analysis of quantum chromodynamics". In: *Phys. Rev. D* 93.3 (2016), p. 033006. DOI: 10.1103/PhysRevD.93.033006. arXiv: 1506.07443 [hep-ph].

[18] Stefano Forte et al. "Neural network parametrization of deep inelastic structure functions". In: *JHEP* 05 (2002), p. 062. DOI: 10.1088/1126-6708/2002/05/062. arXiv: hep-ph/0204232.

[19] S.D. Drell and Tung-Mow Yan. "Massive Lepton Pair Production in Hadron-Hadron Collisions at High-Energies". In: *Phys. Rev. Lett.* 25 (1970). [Erratum: Phys.Rev.Lett. 25, 902 (1970)], pp. 316–320. DOI: 10.1103/PhysRevLett.25.316.

[20] J. H. Christenson et al. "Observation of Massive Muon Pairs in Hadron Collisions". In: *Phys. Rev. Lett.* 25 (21 Nov. 1970), pp. 1523–1526. DOI: 10.1103/PhysRevLett.25.1523.

[21] R. Hamberg, W. L. van Neerven, and T. Matsuura. "A complete calculation of the order α_s^2 correction to the Drell–Yan K-factor". In: *Nucl. Phys. B* 359 (1991). Erratum: 10.1016/S0550-3213(02)00814-3, p. 343. DOI: 10.1016/0550-3213(91)90064-5.

[22] Charalampos Anastasiou et al. "Dilepton Rapidity Distribution in the Drell-Yan Process at Next-to-Next-to-Leading Order in QCD". In: *Phys.*

Rev. Lett. 91 (18 Oct. 2003), p. 182002. DOI: 10.1103/PhysRevLett.91.182002.

[23] Charalampos Anastasiou et al. "High-precision QCD at hadron colliders: Electroweak gauge boson rapidity distributions at next-to-next-to leading order". In: *Phys. Rev. D* 69 (9 May 2004), p. 094008. DOI: 10.1103/PhysRevD.69.094008.

[24] Ye Li and Frank Petriello. "Combining QCD and electroweak corrections to dilepton production in the framework of the FEWZ simulation code". In: *Phys. Rev. D* 86 (9 Nov. 2012), p. 094034. DOI: 10.1103/PhysRevD.86.094034.

[25] Stefano Catani et al. "Vector Boson Production at Hadron Colliders: A Fully Exclusive QCD Calculation at Next-to-Next-to-Leading Order". In: *Phys. Rev. Lett.* 103 (8 Aug. 2009), p. 082001. DOI: 10.1103/PhysRevLett.103.082001.

[26] Claude Duhr, Falko Dulat, and Bernhard Mistlberger. "The Drell-Yan cross section to third order in the strong coupling constant". In: (Jan. 2020). arXiv: 2001.07717 [hep-ph].

[27] CMS Collaboration. "Measurement of differential and double-differential Drell–Yan cross sections in proton-proton collisions at $\sqrt{s} = 8\,\text{TeV}$". In: *Eur. Phys. J. C* 75 (2015), p. 147. DOI: 10.1140/epjc/s10052-015-3364-2. arXiv: 1412.1115 [hep-ex].

[28] CMS Collaboration. "Measurement of the inclusive W and Z production cross sections in pp collisions at $\sqrt{s} = 7\,\text{TeV}$ with the CMS experiment". In: *JHEP* 10 (2011), p. 132. DOI: 10.1007/JHEP10(2011)132. arXiv: 1107.4789 [hep-ex].

[29] CMS Collaboration. "Search for a narrow resonance in high-mass dilepton final states in proton-proton collisions using 140 fb^{-1} of data at $\sqrt{s}$=13 TeV". In: CMS-PAS-EXO-19-019 (Aug. 2019). URL: https://cds.cern.ch/record/2684757.

[30] Lyndon Evans and Philip Bryant. "LHC Machine". In: *Journal of Instrumentation* 3.08 (Aug. 2008), S08001–S08001. DOI: 10.1088/1748-0221/3/08/s08001.

[31] R Garoby. "PLANS for upgrading the CERN proton accelerator complex". In: *Journal of Physics: Conference Series* 110.11 (May 2008), p. 112003. DOI: 10.1088/1742-6596/110/11/112003.

[32] Jorg Wenninger. "LHC status and performance". In: *PoS* CHARGED2018 (2019), p. 001. DOI: 10.22323/1.339.0001.

[33] Matthias Schott and Monica Dunford. "Review of single vector boson production in pp collisions at $\sqrt{s}$ = 7 TeV". In: *Eur. Phys. J. C* 74 (2014), p. 2916. DOI: 10.1140/epjc/s10052-014-2916-1. arXiv: 1405.1160 [hep-ex].

[34] CMS Collaboration. "The CMS experiment at the CERN LHC". In: *JINST* 3 (2008), S08004. DOI: 10.1088/1748-0221/3/08/S08004.

[35] CMS Collaboration. "CMS Technical Design Report for the Pixel Detector Upgrade". In: (Sept. 2012). DOI: 10.2172/1151650.

[36] CMS Collaboration. "CMS Physics: Technical Design Report Volume 1: Detector Performance and Software". In: (2006).

[37] CMS Collaboration. "Energy Calibration and Resolution of the CMS Electromagnetic Calorimeter in *pp* Collisions at $\sqrt{s}$ = 7 TeV". In: *JINST* 8 (2013), p. 9009. DOI: 10.1088/1748-0221/8/09/P09009. arXiv: 1306.2016 [hep-ex].

[38] CMS Collaboration. "Performance of the CMS muon detector and muon reconstruction with proton-proton collisions at $\sqrt{s} = 13\,\text{TeV}$". In: *JINST* 13 (2018), P06015. DOI: 10.1088/1748-0221/13/06/P06015. arXiv: 1804.04528 [physics.ins-det].

[39] CMS Collaboration. "The upgrade of the CMS trigger system". In: *JINST* 9 (2014), p. C08002. DOI: 10.1088/1748-0221/9/08/C08002.

[40] CMS Collaboration. "Particle-flow reconstruction and global event description with the CMS detector". In: *JINST* 12.10 (2017), P10003. DOI: 10.1088/1748-0221/12/10/P10003. arXiv: 1706.04965 [physics.ins-det].

[41] CMS Collaboration. "Performance of Photon Reconstruction and Identification with the CMS Detector in Proton-Proton Collisions at sqrt(s) = 8 TeV". In: *JINST* 10.08 (2015), P08010. DOI: 10.1088/1748-0221/10/08/P08010. arXiv: 1502.02702 [physics.ins-det].

[42] CMS Collaboration. "Performance of Electron Reconstruction and Selection with the CMS Detector in Proton-Proton Collisions at $\sqrt{\text{s}} = 8$ TeV". In: *JINST* 10.06 (2015), P06005. DOI: 10.1088/1748-0221/10/06/P06005. arXiv: 1502.02701 [physics.ins-det].

[43] W Adam et al. "Reconstruction of electrons with the Gaussian-sum filter in the CMS tracker at the LHC". In: *Journal of Physics G: Nuclear and Particle Physics* 31.9 (July 2005), N9–N20. DOI: 10.1088/0954-3899/31/9/n01.

[44] Matteo Cacciari, Gavin P. Salam, and Gregory Soyez. "The anti-k_t jet clustering algorithm". In: *JHEP* 04 (2008), p. 063. DOI: 10.1088/1126-6708/2008/04/063. arXiv: 0802.1189 [hep-ph].

[45] CMS Collaboration. "Jet energy scale and resolution in the CMS experiment in pp collisions at 8 TeV". In: *JINST* 12.02 (2017), P02014. DOI: 10.1088/1748-0221/12/02/P02014. arXiv: 1607.03663 [hep-ex].

[46] CMS Collaboration. "Performance of the CMS missing transverse momentum reconstruction in pp data at $\sqrt{s} = 8$ TeV". In: *JINST* 10.02 (2015), P02006. DOI: 10.1088/1748-0221/10/02/P02006. arXiv: 1411.0511 [physics.ins-det].

[47] CMS Collaboration. "Measurement of the differential Drell-Yan cross section in proton-proton collisions at $\sqrt{\mathrm{s}} = 13$ TeV". In: *JHEP* 12 (2019), p. 059. DOI: 10.1007/JHEP12(2019)059. arXiv: 1812.10529 [hep-ex].

[48] CMS Collaboration. "Measurement of the Drell–Yan Cross Section in pp Collisions at $\sqrt{s} = 7\,\mathrm{TeV}$". In: *JHEP* 10 (2011), p. 007. DOI: 10.1007/JHEP10(2011)007. arXiv: 1108.0566 [hep-ex].

[49] CMS Collaboration. "Measurement of the differential and double-differential Drell–Yan cross sections in proton-proton collisions at $\sqrt{s} = 7\,\mathrm{TeV}$". In: *JHEP* 12 (2013), p. 030. DOI: 10.1007/JHEP12(2013)030. arXiv: 1310.7291 [hep-ex].

[50] CMS Collaboration. "Measurement of differential and double-differential Drell–Yan cross sections in proton-proton collisions at $\sqrt{s} = 8\,\mathrm{TeV}$". In: *Eur. Phys. J. C* 75 (2015), p. 147. DOI: 10.1140/epjc/s10052-015-3364-2. arXiv: 1412.1115 [hep-ex].

[51] J. Alwall et al. "The automated computation of tree-level and next-to-leading order differential cross sections, and their matching to parton shower simulations". In: *JHEP* 07 (2014), p. 079. DOI: 10.1007/JHEP07(2014)079. arXiv: 1405.0301 [hep-ph].

[52] Paolo Nason. "A New Method for Combining NLO QCD with Shower Monte Carlo Algorithms". In: *JHEP* 11 (2004), p. 040. DOI: 10.1088/1126-6708/2004/11/040. arXiv: hep-ph/0409146 [hep-ph].

[53] Stefano Frixione, Paolo Nason, and Carlo Oleari. "Matching NLO QCD computations with parton shower simulations: the POWHEG method". In: *JHEP* 11 (2007), p. 070. DOI: 10.1088/1126-6708/2007/11/070. arXiv: 0709.2092 [hep-ph].

[54] Simone Alioli et al. "A General Framework for Implementing NLO Calculations in Shower Monte Carlo Programs: the POWHEG BOX". In: *JHEP* 06 (2010), p. 043. DOI: 10.1007/JHEP06(2010)043. arXiv: 1002.2581 [hep-ph].

[55] Stefano Frixione, Paolo Nason, and Giovanni Ridolfi. "A Positive-Weight Next-to-Leading-Order Monte Carlo for Heavy Flavour Hadroproduction". In: *JHEP* 09 (2007), p. 126. DOI: 10.1088/1126-6708/2007/09/126. arXiv: 0707.3088 [hep-ph].

[56] Emanuele Re. "Single-top Wt-channel production matched with parton showers using the POWHEG method". In: *Eur. Phys. J. C* 71 (2011), p. 1547. DOI: 10.1140/epjc/s10052-011-1547-z. arXiv: 1009.2450 [hep-ph].

[57] Torbjörn Sjöstrand et al. "An Introduction to PYTHIA 8.2". In: *Comput. Phys. Commun.* 191 (2015), p. 159. DOI: 10.1016/j.cpc.2015.01.024. arXiv: 1410.3012 [hep-ph].

[58] NNPDF Collaboration. "A first unbiased global NLO determination of parton distributions and their uncertainties". In: *Nucl. Phys. B* 838 (2010), p. 136. DOI: 10.1016/j.nuclphysb.2010.05.008. arXiv: 1002.4407 [hep-ph].

[59] NNPDF Collaboration. "Parton distributions for the LHC Run II". In: *JHEP* 04 (2015), p. 040. DOI: 10.1007/JHEP04(2015)040. arXiv: 1410.8849 [hep-ph].

[60] CMS Collaboration. "Event generator tunes obtained from underlying event and multiparton scattering measurements". In: *Eur. Phys. J. C* 76 (2016), p. 155. DOI: 10.1140/epjc/s10052-016-3988-x. arXiv: 1512.00815 [hep-ex].

[61] Michal Czakon and Alexander Mitov. "Top++: A program for the calculation of the top-pair cross-section at hadron colliders". In: *Comput. Phys. Commun.* 185 (2014), p. 2930. DOI: 10.1016/j.cpc.2014.06.021. arXiv: 1112.5675 [hep-ph].

[62] Tom Melia et al. "W^+W^-, WZ and ZZ production in the POWHEG BOX". In: *JHEP* 11 (2011), p. 078. DOI: 10.1007/JHEP11(2011)078. arXiv: 1107.5051 [hep-ph].

[63] John M. Campbell, R. Keith Ellis, and Ciaran Williams. "Vector boson pair production at the LHC". In: *JHEP* 07 (2011), p. 018. DOI: 10.1007/JHEP07(2011)018. arXiv: 1105.0020 [hep-ph].

[64] S. Agostinelli et al. "GEANT4 — a simulation toolkit". In: *Nucl. Instrum. Meth. A* 506 (2003), p. 250. DOI: 10.1016/S0168-9002(03)01368-8.

[65] CMS Collaboration. "Energy calibration and resolution of the CMS electromagnetic calorimeter in pp collisions at $\sqrt{s} = 7\,\text{TeV}$". In: *JINST* 8 (2013), P09009. DOI: 10.1088/1748-0221/8/09/P09009. arXiv: 1306.2016 [hep-ex].

[66] CMS Collaboration. "Performance of electron reconstruction and selection with the CMS detector in proton-proton collisions at $\sqrt{s} = 8\,\text{TeV}$".

In: *JINST* 10 (2015), P06005. DOI: 10.1088/1748-0221/10/06/P06005. arXiv: 1502.02701 [physics.ins-det].

[67] CMS Collaboration. "Particle-flow reconstruction and global event description with the CMS detector". In: *JINST* 12 (2017), P10003. DOI: 10.1088/1748-0221/12/10/P10003. arXiv: 1706.04965 [hep-ex].

[68] A. Bodek et al. "Extracting muon momentum scale corrections for hadron collider experiments". In: *Eur. Phys. J. C* 72 (2012), p. 2194. DOI: 10.1140/epjc/s10052-012-2194-8. arXiv: 1208.3710 [hep-ex].

[69] CMS Collaboration. "Angular coefficients of Z bosons produced in pp collisions at $\sqrt{s} = 8$ TeV and decaying to $\mu^+\mu^-$ as a function of transverse momentum and rapidity". In: *Phys. Lett. B* 750 (2015), pp. 154–175. DOI: 10.1016/j.physletb.2015.08.061. arXiv: 1504.03512 [hep-ex].

[70] G. D'Agostini. "A multidimensional unfolding method based on Bayes' theorem". In: *Nucl. Instrum. Meth. A* 362 (1995), p. 487. DOI: 10.1016/0168-9002(95)00274-X.

[71] Piotr Golonka and Zbigniew Was. "PHOTOS Monte Carlo: a precision tool for QED corrections in Z and W decays". In: *Eur. Phys. J. C* 45 (2006), p. 97. DOI: 10.1140/epjc/s2005-02396-4. arXiv: hep-ph/0506026 [hep-ph].

[72] CMS Collaboration. "CMS Luminosity Measurement for the 2015 Data Taking Period". In: CMS-PAS-LUM-15-001 (Mar. 2016). URL: https://cds.cern.ch/record/2138682.

[73] CMS Collaboration. "Measurements of differential production cross sections for a Z boson in association with jets in pp collisions at $\sqrt{s} =$

8 TeV". In: *JHEP* 04 (2017), p. 022. DOI: 10.1007/JHEP04(2017)022. arXiv: 1611.03844 [hep-ex].

[74] G. D. Lafferty and T. R. Wyatt. "Where to stick your data points: The treatment of measurements within wide bins". In: *Nucl. Instrum. Meth. A* 355 (1995), p. 541. DOI: 10.1016/0168-9002(94)01112-5.

Appendix A

Tag-and-probe Efficiency

A.1 Dimuon channel

The efficiency of muons are parametrized in muon p_{T} and η following the binning below:

- p_{T}: 10, 22, 40, 70, 250 GeV
- η: -2.4, -1.2, -0.3, 0.3, 1.2, 2.4

The fitting on the tag and probe dimuon mass distribution is performed to subtract the contribution from the backgrounds not coming from Z boson events. For the fitting, Double Voigtian and exponential functions are used for the signal and background shape respectively. The example of the fit result is shown in Fig. A.1.

The offline selection efficiency of single muon ε_μ is factorized in following way:

$$\varepsilon_\mu = \varepsilon_{reco+id} \cdot \varepsilon_{iso} \tag{A.1}$$

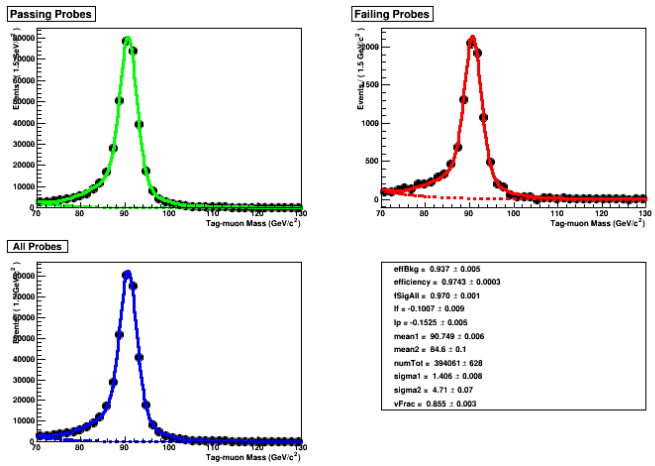

Figure A.1: Example of fit result in the muon tag-and-probe method.

where $\varepsilon_{reco+id}$ is the reconstruction and identification efficiency and ε_{iso} is the isolation efficiency. $\varepsilon_{reco+id}$ is defined as the fraction of muons passing the ID used in the analysis (high-p_{T} muon ID) with respect to the general tracks. Similarly, ε_{iso} is defined as the fraction of muons passing the tracker-based isolation with respect to the muons passing high-p_{T} muon ID (numerator of $\varepsilon_{reco+id}$).

Finally, the efficiency of a dimuon event $\varepsilon_{\mathrm{event}}$ can be obtained by the formula below:

$$\varepsilon_{\mathrm{event}} = \varepsilon_{\ell_1} \times \varepsilon_{\ell_2} \times \varepsilon_{\mathrm{event,\ trig}} \tag{A.2}$$

where $\varepsilon_{\ell_{1,2}}$ is the offline selection efficiency of two muons, and $\varepsilon_{\mathrm{event,\ trig}}$ is the event trigger efficiency. As the single muon trigger is used in the analysis, $\varepsilon_{\mathrm{event,\ trig}}$ can be obtained by factorizing into the single muon trigger efficiencies for each muon $\varepsilon_{\mu,\mathrm{trig}}$, defined as the fraction of muons matched to a trigger object with respect to the offline muons passing ID and isolation condition (numerator of ε_{iso}):

$$\begin{aligned}\varepsilon(\text{event}, \text{trig}) &= 1 - P(\text{both muons}, \text{failed}) \\ &= 1 - (1 - \varepsilon(\mu_1, \text{trig})) \cdot (1 - \varepsilon(\mu_2, \text{trig})) \\ &= \varepsilon(\mu_1, \text{trig}) + \varepsilon(\mu_2, \text{trig}) - \varepsilon(\mu_1, \text{trig}) \cdot \varepsilon(\mu_2, \text{trig}),\end{aligned} \tag{A.3}$$

It reflects the fact that the event is fired unless both muons fail to fire the single muon trigger.

In the analysis, there was a dedicated treatment on the trigger efficiency in the dimuon channel. During the 2015 data taking, the working point for the isolation in the isolated single muon trigger was tuned, and it leads the improvement of the trigger efficiency. Therefore, the trigger efficiency is measured separately for the data before the isolation update (HLT configuration version 4.2 with run$\leq$ 257932 or denoted as HLT v4.2) and after the update (HLT v4.3 with with run$\geq$ 257933). The scale factor is computed and applied separately to each subset of the data.

The efficiency results obtained by tag-and-probe method are shown in Fig. A.2 ($\varepsilon_{reco+id}$), Fig. A.3 (ε_{iso}), Fig. A.4 ($\varepsilon_{\mu,\text{trig}}$ for HLT v4.2 data) and Fig. A.5 ($\varepsilon_{\mu,\text{trig}}$ for HLT v4.3 data).

A.2 Dielectron channel

The electron efficiency is parametrized in electron p_T and η following the binning below:

- p_T: 10, 20, 30, 40, 50, 200 GeV
- η: -2.5, -2.0, -1.566, -1.4442, -0.8, 0, 0.8, 1.4442, 1.566, 2.0, 2.5

The efficiency values in the gap between the barrel and endcap of ECAL ($1.4442 < |\eta| < 1.566$) is shown just as a demonstration purpose and they are

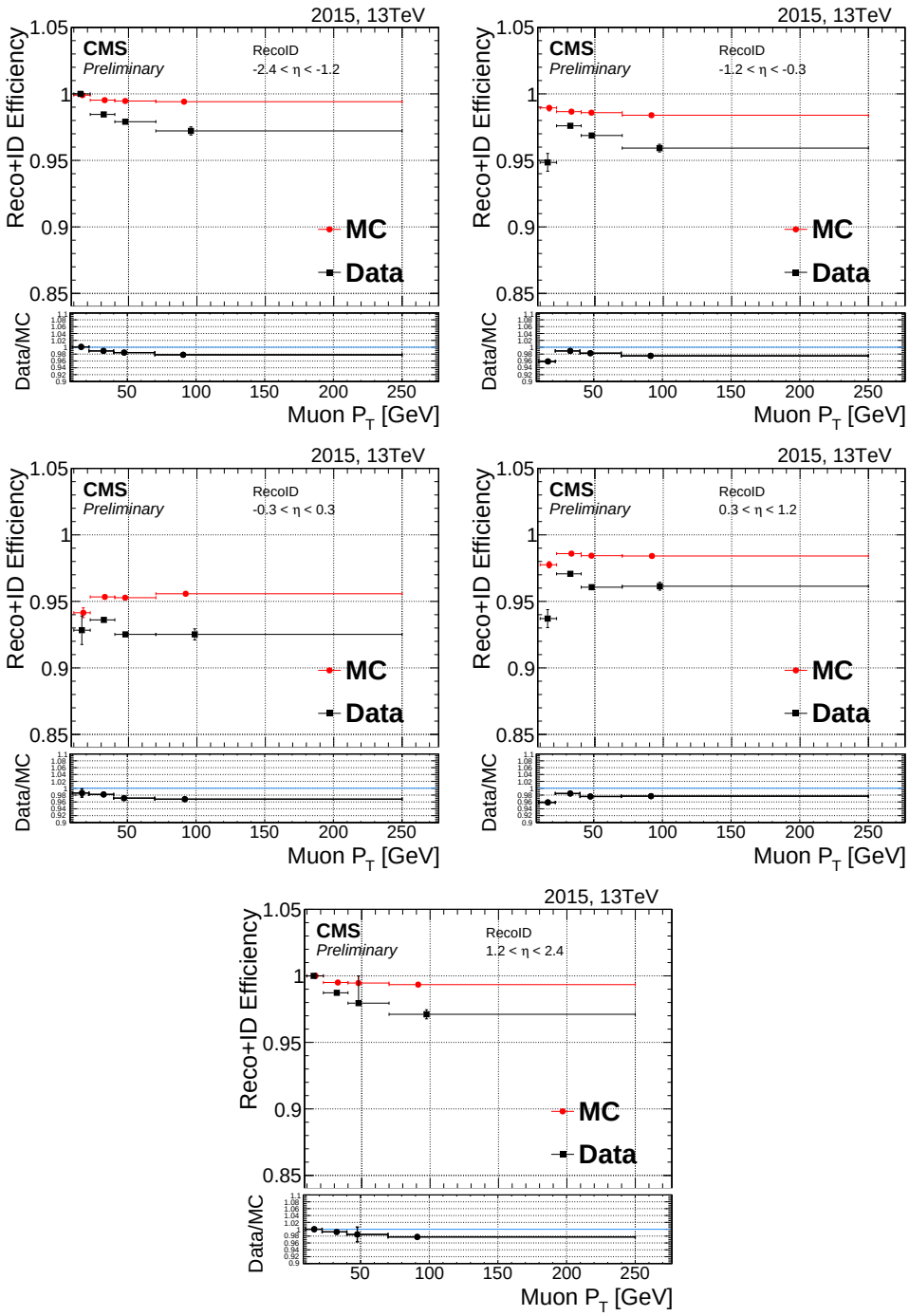

Figure A.2: Muon reconstruction and identification efficiency as a function of p_{T} obtained from the tag-and-probe method for each eta region.

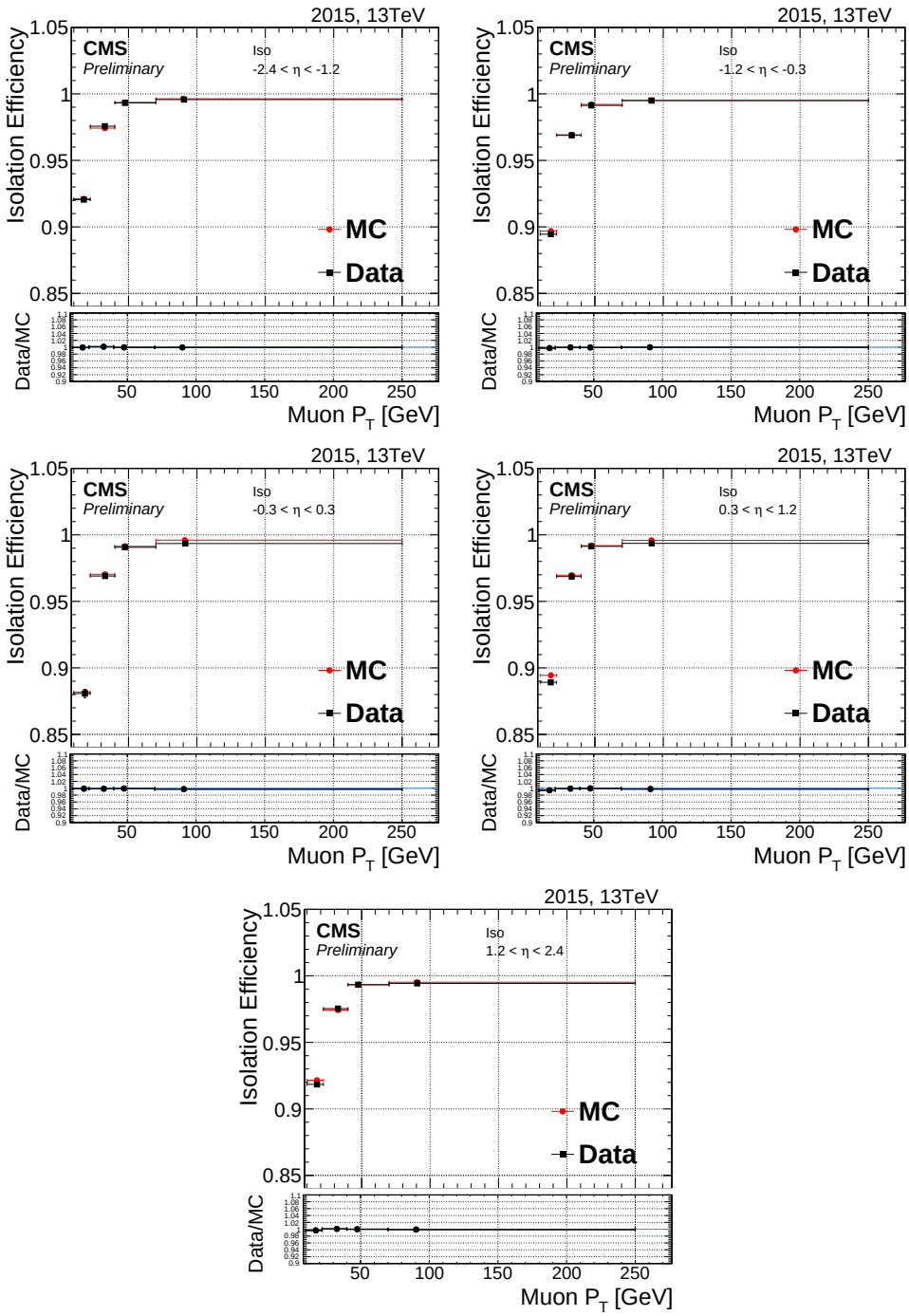

Figure A.3: Muon isolation efficiency as a function of p_{T} obtained from the tag-and-probe method for each eta region.

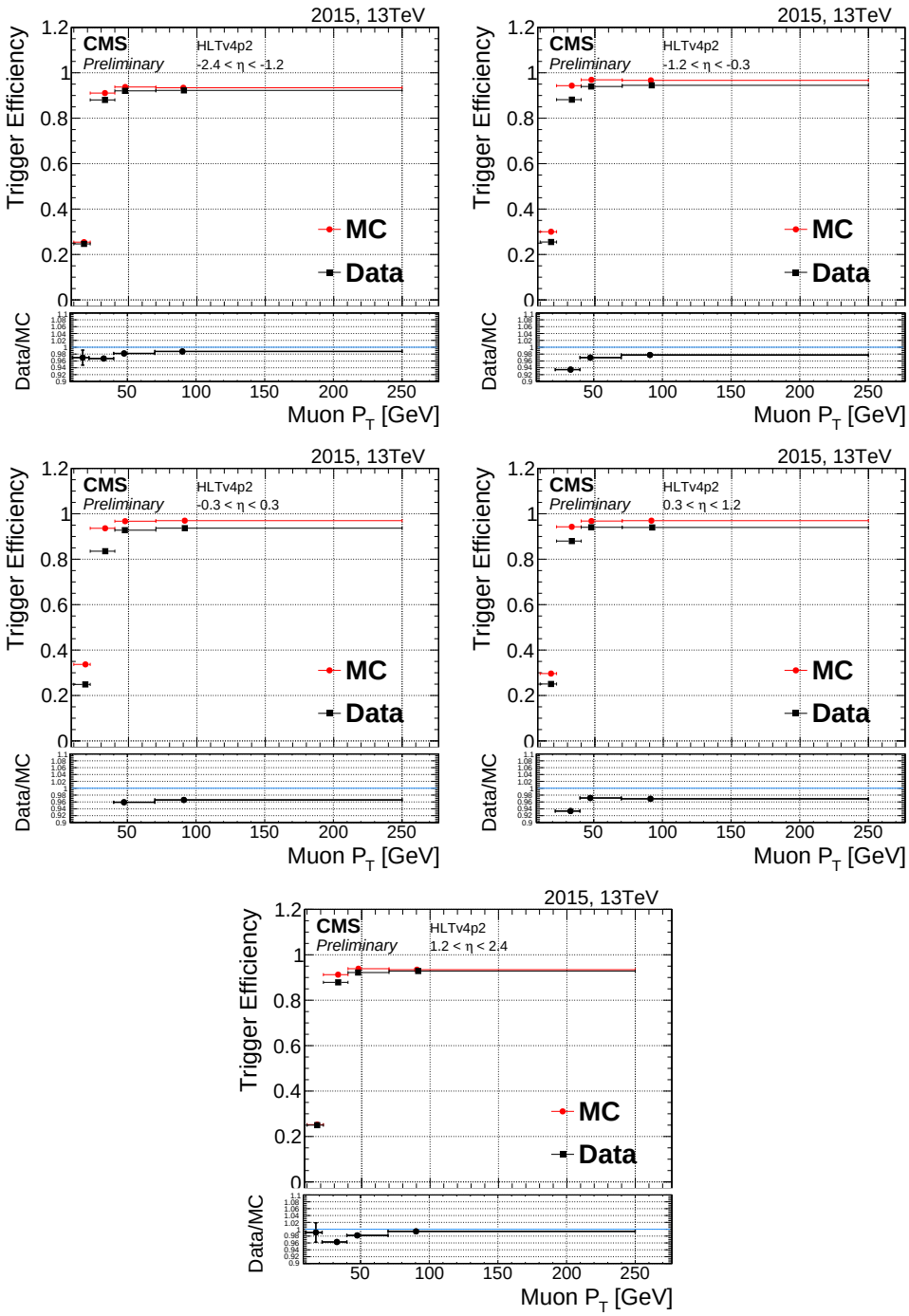

Figure A.4: Muon trigger efficiency (HLT v4.2 data) as a function of p_{T} obtained from the tag-and-probe method for each eta region.

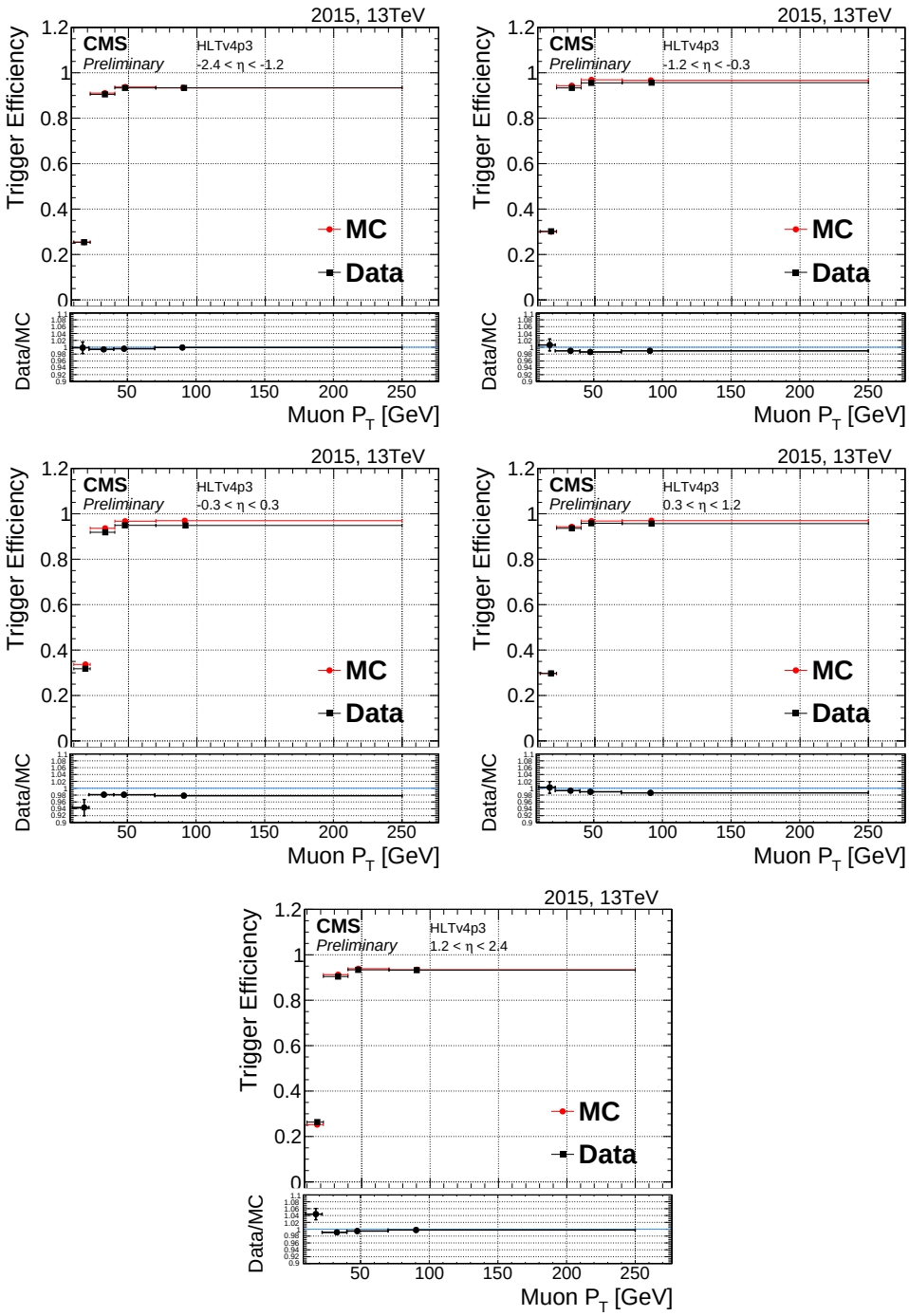

Figure A.5: Muon trigger efficiency (HLT v4.3 data) as a function of p_{T} obtained from the tag-and-probe method for each eta region.

not used in the analysis. The electrons in the gap are excluded in the event selection procedure as described in Section 5.3.2.

Similar to the dimuon channel, the fitting is performed on the dielectron mass distribution to subtract the backgrounds. However, simple counting is used for the trigger efficiency measurement without fitting because the contribution from the backgrounds is negligible due to the tight conditions on the probe. To fit the data distribution, the shape of the dielectron mass distribution near Z resonance is taken from the Z$\rightarrow \ell\ell$ MC sample (MC template) bin by bin and used in the fitting with the Gaussian smearing to describe resolution effects. For the background shape, the combination of exponential and error function ("CMS shape") is used.

The factorization of the offline selection efficiency for electron is slightly different with the muon case:

$$\varepsilon_e = \varepsilon_{reco} \cdot \varepsilon_{id+iso} \tag{A.4}$$

where ε_{reco} is the electron reconstruction efficiency and ε_{id+iso} is the identification and isolation efficiency. ε_{reco} is defined as the fraction of reconstructed electrons over total number of supercluster. ε_{id+iso} is defined as the fraction of electrons passing ID and isolation requirement used in the analysis with respect to total reconstructed electrons.

Finally, the event efficiency is computed following the same way used in the dimuon channel with (A.2) and (A.3).

The efficiency results for the electrons are shown in Fig. A.6 (ε_{reco}), Fig. A.7 (ε_{id+iso}) and Fig. A.8 ($\varepsilon_{\mathrm{e,\ trig}}$).

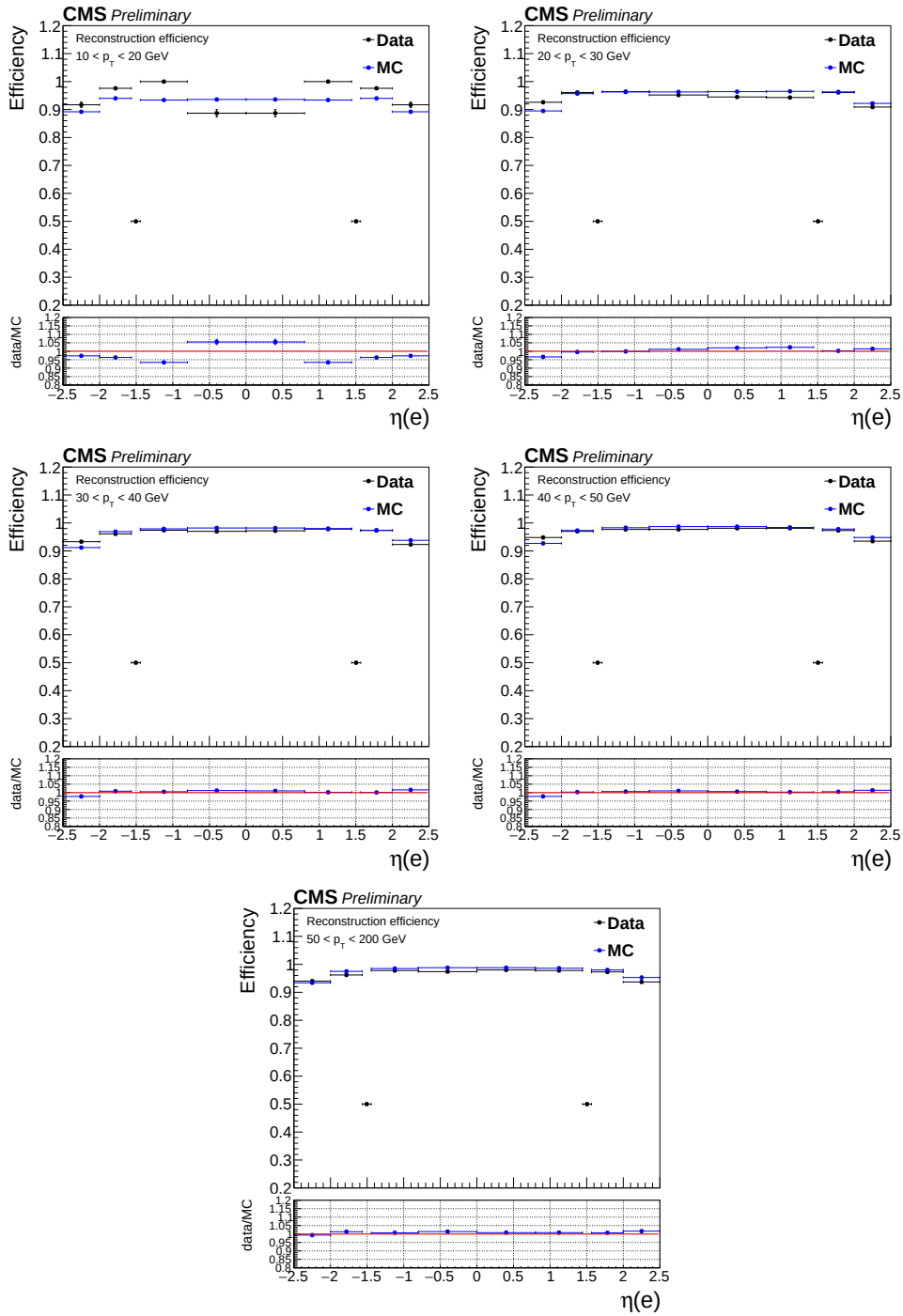

Figure A.6: Electron reconstruction efficiency as a function of η obtained from the tag-and-probe method for each p_{T} region.

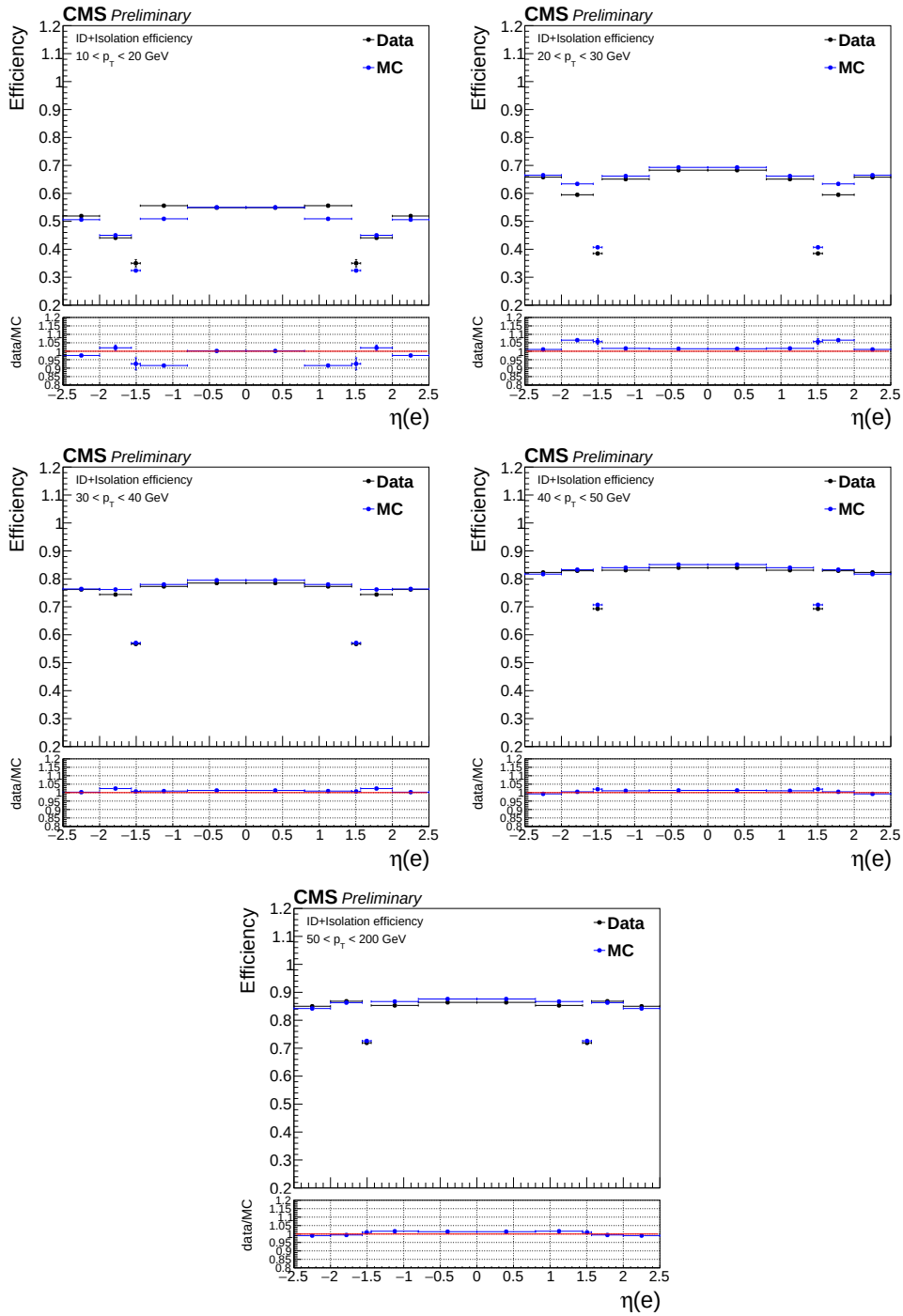

Figure A.7: Electron ID and isolation efficiency as a function of η obtained from the tag-and-probe method for each p_{T} region.

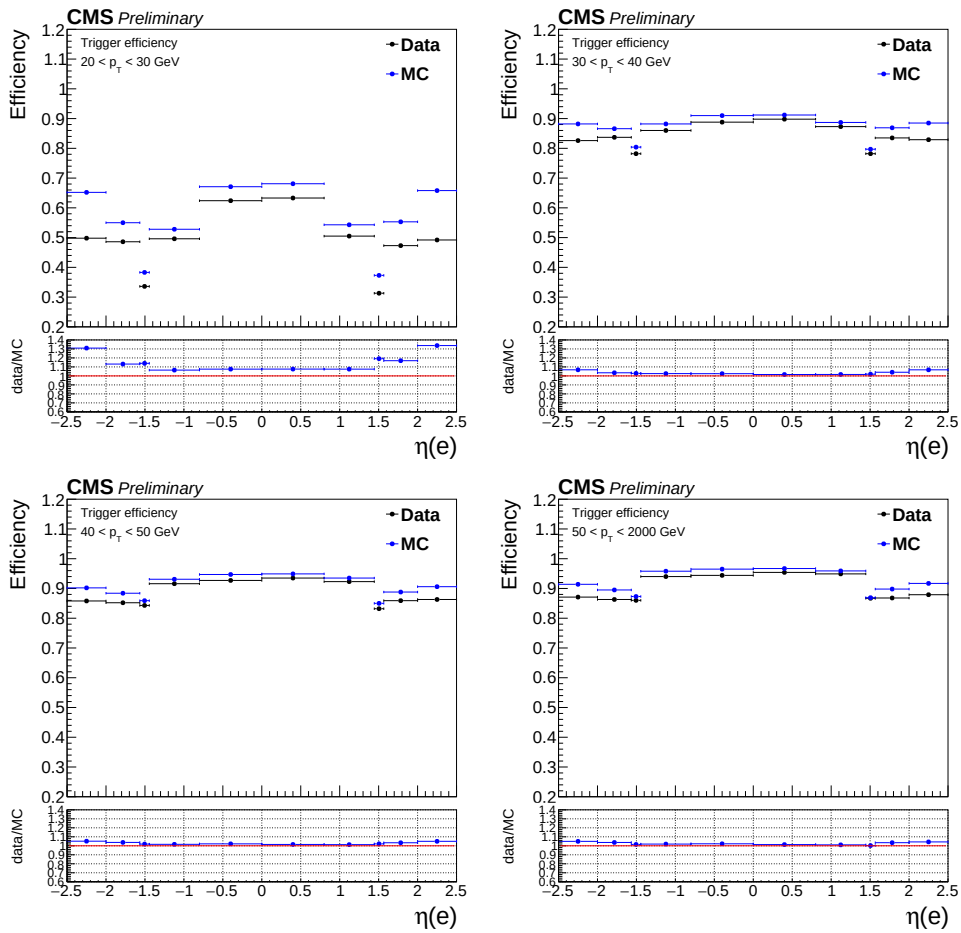

Figure A.8: Electron trigger efficiency as a function of η obtained from the tag-and-probe method for each p_{T} region. The first bin ($10 < p_{\mathrm{T}} < 20\,\mathrm{GeV}$) is not included because it is far below the p_{T} threshold of the trigger ($23\,\mathrm{GeV}$) and the efficiency is basically zero.

Appendix B

Table for the systematic uncertainties

Table B.1: Summary of the systematic uncertainties (%) for the $d\sigma/dm$ (pb/GeV) measurement in the dimuon channel ($m < 120\,\text{GeV}$). The column labelled "Total" corresponds to the quadratic sum of all the experimental sources, except for that Acceptance+PDF.

m (GeV)	Eff. (%)	Det. resol. (%)	Bkgr. est. (%)	FSR (%)	Total (%)	Acceptance+PDF (%)
15–20	3.5	1.9	0.28	0.13	4.0	5.6
20–25	3.5	1.6	0.61	0.26	3.9	4.8
25–30	3.6	1.3	0.45	0.35	3.9	12
30–35	4.0	1.1	0.89	0.38	4.3	9.5
35–40	4.2	1.0	0.98	0.39	4.5	5.6
40–45	4.0	0.95	1.3	0.40	4.3	2.0
45–50	3.3	0.94	1.2	0.47	3.7	1.6
50–55	2.7	0.94	1.1	0.65	3.1	1.7
55–60	2.3	0.95	1.2	0.89	2.9	1.8
60–64	2.1	0.94	0.83	1.1	2.7	2.0
64–68	1.6	0.91	0.72	1.3	2.4	2.0
68–72	1.4	0.86	0.66	1.5	2.3	2.1
72–76	1.1	0.82	0.30	1.5	2.1	2.1
76–81	1.0	0.83	0.20	1.5	2.0	2.1
81–86	1.1	0.94	0.082	1.6	2.1	2.0
86–91	1.3	1.2	0.042	1.6	2.4	2.0
91–96	1.4	1.6	0.042	1.8	2.8	1.9
96–101	1.5	1.9	0.075	1.9	3.1	1.7
101–106	1.6	2.2	0.20	1.9	3.3	1.6
106–110	1.7	2.4	0.46	1.9	3.5	1.4
110–115	1.8	2.5	0.73	1.8	3.6	1.3
115–120	1.9	2.6	1.0	1.6	3.8	1.2

Table B.2: Summary of the systematic uncertainties (%) for the $d\sigma/dm$ (pb/GeV) measurement in the dimuon channel ($m > 120\,\text{GeV}$). The column labelled "Total" corresponds to the quadratic sum of all the experimental sources, except for that Acceptance+PDF.

m (GeV)	Eff. (%)	Det. resol. (%)	Bkgr. est. (%)	FSR (%)	Total (%)	Acceptance+PDF (%)
120–126	2.1	2.8	1.4	1.5	4.0	1.1
126–133	2.3	2.9	1.8	1.5	4.4	1.1
133–141	2.3	3.1	2.2	1.6	4.7	1.0
141–150	2.4	3.3	2.6	1.9	5.2	0.98
150–160	2.4	3.6	2.9	2.2	5.6	0.95
160–171	2.7	3.9	3.3	2.2	6.1	1.2
171–185	2.9	4.0	3.8	2.2	6.6	0.88
185–200	3.1	3.8	4.7	2.2	7.1	1.0
200–220	3.4	3.3	5.8	2.3	7.8	1.2
220–243	3.6	2.9	7.0	2.6	8.8	0.90
243–273	3.8	2.6	8.1	2.9	9.8	0.77
273–320	3.9	2.7	8.8	3.3	11	0.73
320–380	3.9	3.2	9.2	3.4	11	0.65
380–440	4.1	4.0	9.5	3.5	12	0.73
440–510	4.2	4.9	9.5	3.6	12	0.64
510–600	4.2	5.5	9.4	3.8	12	0.45
600–700	4.3	6.0	9.1	4.2	12	0.30
700–830	4.3	19	8.7	4.7	22	0.45
830–1000	4.4	18	8.2	5.0	21	0.76
1000–1500	4.5	17	7.9	5.3	20	1.2
1500–3000	4.7	150	7.7	5.5	160	1.7

Table B.3: Summary of the systematic uncertainties (%) for the $d\sigma/dm$ (pb/GeV) measurement in the dielectron channel ($m < 120\,\text{GeV}$). The column labelled "Total" corresponds to the quadratic sum of all the experimental sources, except for that Acceptance+PDF.

m (GeV)	Eff. (%)	Det. resol. (%)	Bkgr. est. (%)	FSR (%)	Total (%)	Acceptance+PDF (%)
15–20	3.2	0.73	0.98	3.5	4.9	5.7
20–25	3.1	1.0	1.5	3.1	4.8	4.7
25–30	3.1	1.3	2.0	3.1	5.0	9.5
30–35	3.2	1.5	2.5	3.4	5.5	16
35–40	3.4	1.7	3.3	3.9	6.4	16
40–45	3.4	2.0	4.2	4.2	7.1	14
45–50	3.4	2.2	4.7	4.0	7.3	12
50–55	3.4	2.3	4.6	3.5	7.1	9.4
55–60	3.4	2.5	4.2	2.4	6.4	7.6
60–64	3.5	2.8	3.7	1.1	5.9	6.7
64–68	3.0	3.0	2.8	0.71	5.1	5.6
68–72	2.6	2.9	2.0	0.87	4.5	4.7
72–76	2.4	2.4	1.4	0.96	3.8	4.0
76–81	2.2	1.7	0.77	1.0	3.1	3.4
81–86	2.0	0.97	0.30	1.0	2.4	2.8
86–91	1.7	0.53	0.075	1.3	2.2	2.3
91–96	1.6	0.55	0.060	1.9	2.5	1.9
96–101	1.5	0.88	0.20	2.1	2.7	1.6
101–106	1.4	1.6	0.47	2.1	3.0	1.4
106–110	1.4	2.8	0.81	2.1	3.8	1.2
110–115	1.4	3.6	1.1	2.2	4.6	1.1
115–120	1.4	3.6	1.4	2.4	4.7	1.1

Table B.4: Summary of the systematic uncertainties (%) for the $d\sigma/dm$ (pb/GeV) measurement in the dielectron channel ($m > 120\,\text{GeV}$). The column labelled "Total" corresponds to the quadratic sum of all the experimental sources, except for that Acceptance+PDF.

m (GeV)	Eff. (%)	Det. resol. (%)	Bkgr. est. (%)	FSR (%)	Total (%)	Acceptance+PDF (%)
120–126	1.4	3.1	1.7	2.9	4.8	1.1
126–133	1.4	2.9	2.1	4.6	6.0	1.1
133–141	1.4	3.0	2.7	6.3	7.6	1.2
141–150	1.5	3.2	3.1	7.0	8.4	1.2
150–160	1.5	3.4	3.5	7.0	8.7	1.1
160–171	1.5	3.4	4.2	7.1	9.1	1.0
171–185	1.6	3.2	4.9	7.1	9.4	0.88
185–200	1.5	2.5	5.8	7.1	9.6	0.84
200–220	1.5	1.6	6.3	7.1	9.8	0.89
220–243	1.6	0.96	6.9	7.2	10	0.73
243–273	1.6	0.81	7.5	6.9	10	0.67
273–320	1.6	0.84	7.9	6.4	10	0.64
320–380	1.6	0.85	8.1	6.3	10	0.56
380–440	1.6	0.88	9.0	6.6	11	0.48
440–510	1.6	0.92	10	6.7	13	0.41
510–600	1.6	0.93	11	8.0	14	0.37
600–700	1.6	0.95	13	11	18	0.32
700–830	1.6	1.0	19	14	24	0.28
830–1000	1.6	0.96	43	14	45	0.25
1000–1500	1.6	0.82	81	13	82	0.36
1500–3000	1.5	0.76	100	12	100	0.66

Appendix C

Treatment of the correlation and covariance matrices

The understanding of the correlation in the final result is essential to obtain a reliable result from the combination between two channels. The central value and the uncertainty assigned to the combined results depends on the correlation between measurement bins and channels.

The cross section results in each bins are correlated with the values in the other bins due to several sources that have an effect across multiple measurement bins. The efficiency scale factor is one of the example to create the correlation between the bins. As the scale factor is parametrized in single lepton variables (p_{T} and η), same scale factor values can be used in the calculation of the cross sections in different dilepton mass bin. This means that the cross section in multiple bins can be changed coherently if the scale factor in lepton p_{T} and η bin is changed within its uncertainty.

The correlation between two channels should be also taken into account as well as the correlation between measurement bins in each channel. One of the

example to generate the correlation between channels is the theoretical uncertainty on the acceptance and PDF. The acceptance change due to theoretical uncertainties should affect the results in both dimuon and dielectron channel.

In the following section, the correlation property will be discussed for all uncertainties considered in the analysis.

C.1 Correlation property of each uncertainty

C.1.1 Statistical uncertainty

The statistical uncertainty is considered as correlated between measurement bins because the analysis includes unfolding procedures. In other words, a change of signal yield in one bin due to the statistical uncertainty could change the cross section values because the signal yield in the bin is used to compute several unfolding corrections applied to multiple bins.

C.1.2 Systematic uncertainty

The systematic uncertainty can be divided into several groups according to its correlation property.

Luminosity uncertainty

The luminosity uncertainty is assigned with one value (2.3%) for entire bins and same between dimuon and dielectron channel. Therefore, it generate the correlation not only between measurement bins but between channels.

Acceptance uncertainty

As described above, the uncertainty associated to the acceptance comes from the theoretical parts, and it is universal for the dimuon and dielectron channel.

The change of the acceptance due to the theoretical uncertainty simultaneously affect dimuon and dielectron channels. Obviously, It should be considered as 100% correlated between channels.

The other systematic uncertainties

The other systematic uncertainties are divided into "statistical" and "systematic" components. The statistical components means uncertainty sources related to limited statistics. For example, in the background uncertainty, the uncertainty due to the finite statistics in the data control sample is considered as the statistical component. They are considered as correlated between measurement bins due to the same reason with the statistical uncertainty.

The other uncertainty sources are categorized as systematic components. They are usually the uncertainties from the comparison with the other approach with respect to the nominal method used in the analysis. They are considered as uncorrelated in general, except for the uncertainty from the efficiency scale factor, which has correlation between bins.

The exact categorization for each uncertainty is listed below:

Background uncertainty

- Statistical components
  - Uncertainty propagated from the statistical uncertainty on the fake rate (for backgrounds estimated by fake rate method)
  - Uncertainty propagated from the statistical uncertainty on eμ control sample (for backgrounds estimated by eμ method)
  - Uncertainty due to the limited MC statistics (for backgrounds estimated by MC prediction)

- Systematic components
  - Difference between template fitting and ratio method (for backgrounds estimated by fake rate method)
  - Difference with the MC prediction (for backgrounds estimated by eμ method)
  - Uncertainty of the cross section used in the normalization (for backgrounds estimated by MC prediction)

Efficiency SF

- Statistical components
  - Statistical uncertainty on the tag-and-probe efficiency
- Systematic components
  - Tag-and-probe efficiency difference with alternative tag-and-probe settings (e.g. different fit shape, mass range, etc.)
  - Uncertainty due to the different binning (muon channel only)

Detector resolution

- Statistical components
  - Uncertainty from the momentum or energy scale and resolution corrections
  - Uncertainty from the limited MC statistics used in response matrix calculation
- Systematic components
  - Difference of response matrix from different MC generator

FSR

- Statistical components
  - Uncertainty from the limited MC statistics used in response matrix calculation
- Systematic components
  - Difference of response matrix from different MC generator (PHOTOS)

C.2 Covariance matrices

Two ways are used to estimate the covariance matrices for each correlation source. If the correlation is assumed to be 100% (i.e. acceptance uncertainty and luminosity uncertainty), the construction of the covariance matrix is straightforward as the (i,j) component of the matrix can be ($\mathrm{unc}_i \times \mathrm{unc}_j$) where $\mathrm{unc}_{i,j}$ is the uncertainty of i and jth bin.

For the other correlation sources, the covariance matrix is estimated by generating multiple final cross section values with smearing the central value within its uncertainty. The covariance of (i,j) bin $\mathrm{cov}(i,j)$ is estimated by following the usual formula for unbiased covariance:

$$\mathrm{cov}(i,j) = \frac{1}{N-1}\sum_{a=1}^{N}\left(\sigma_i^{\mathrm{smeared},a}\sigma_j^{\mathrm{smeared},a} - \sigma_i^{\mathrm{nominal}}\sigma_j^{\mathrm{nominal}}\right) \qquad \text{(C.1)}$$

where N is the number of produced cross sections (2000), $\sigma_{i(j)}^{\mathrm{smeared},a}$ is ath smeared cross section for $i(j)$th bin and $\sigma_{i(j)}^{\mathrm{nominal}}$ is the nominal cross section of $i(j)$th bin.

The total covariance and correlation matrices for the dimuon channel and dielectron channel are shown in Fig. C.1. Same set of the matrices for the combined result is presented in Fig. C.2.

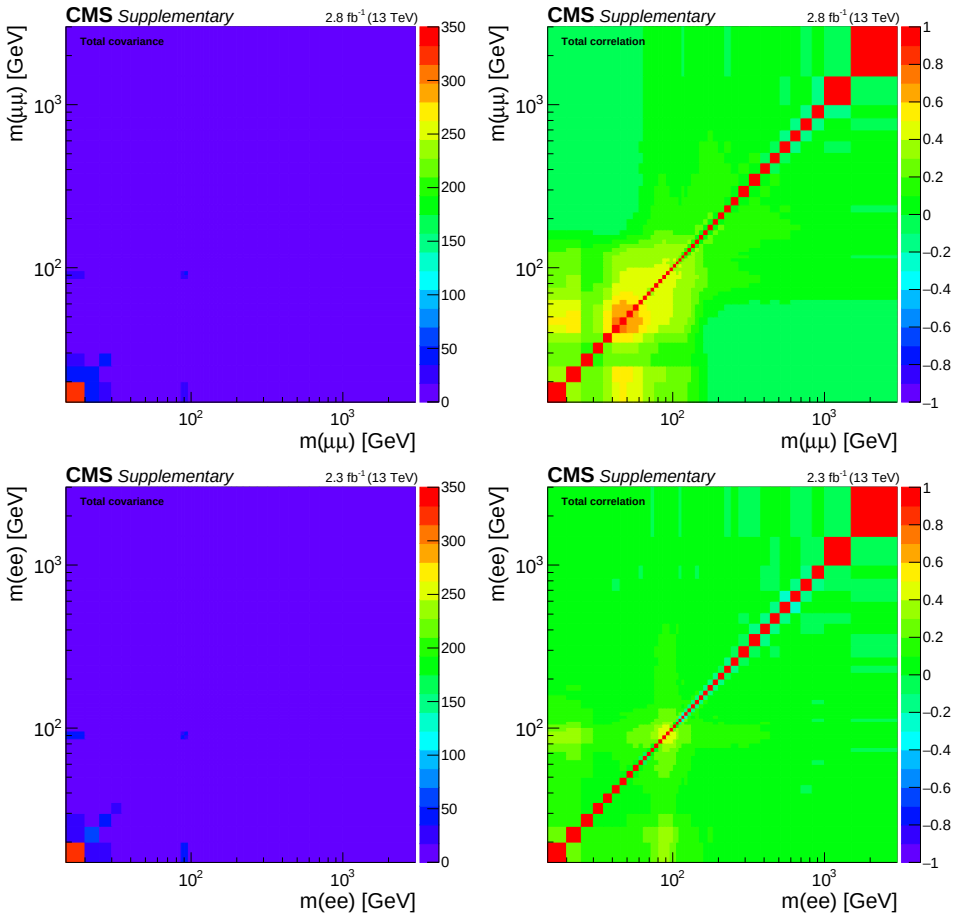

Figure C.1: The covariance (left) and correlation (right) matrices for the dimuon (top) and dielectron (bottom) channels. The correlation from the luminosity uncertainty is included.

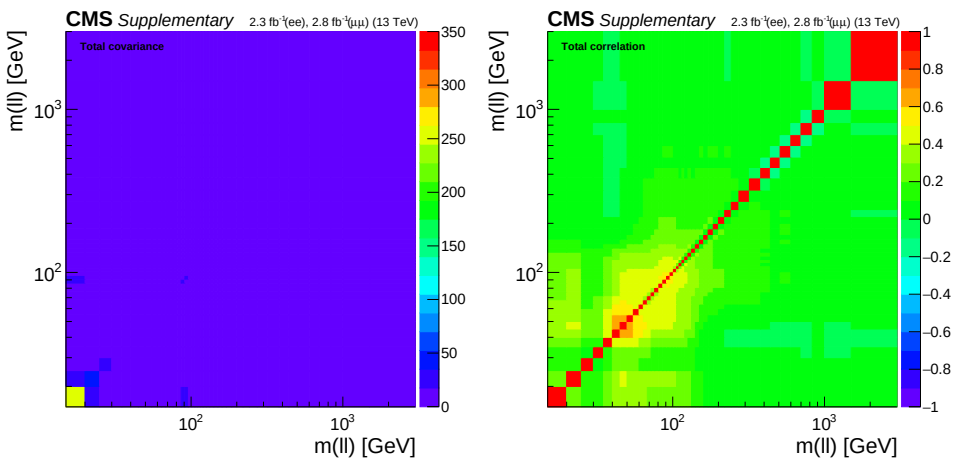

Figure C.2: The covariance and correlation matrices for the combined results. The correlation from the luminosity uncertainty is included.

Appendix D

Table for Differential DY Cross Sections

D.1 Cross section in the full phase space

D.2 Fiducial cross section

D.3 Combined result

Table D.1: Summary of the measured values of $d\sigma/dm$ (pb/GeV) in the dimuon channel ($m < 120\,\text{GeV}$) with the statistical (δ_{stat}), experimental (δ_{exp}) and theoretical (δ_{theo}) uncertainties, respectively. Here, δ_{tot} is the quadratic sum of the three components.

m(GeV)	$\frac{d\sigma}{dm}$ (pb/GeV)	δ_{stat}	δ_{exp}	δ_{theo}	δ_{tot}
15–20	2.5×10^{2}	2.4×10^{0}	1.1×10^{1}	1.4×10^{1}	1.8×10^{1}
20–25	9.9×10^{1}	1.1×10^{0}	4.5×10^{0}	4.7×10^{0}	6.6×10^{0}
25–30	5.3×10^{1}	6.4×10^{-1}	2.4×10^{0}	6.1×10^{0}	6.6×10^{0}
30–35	2.8×10^{1}	3.0×10^{-1}	1.4×10^{0}	2.6×10^{0}	3.0×10^{0}
35–40	1.7×10^{1}	1.5×10^{-1}	8.7×10^{-1}	9.7×10^{-1}	1.3×10^{0}
40–45	1.2×10^{1}	9.7×10^{-2}	5.7×10^{-1}	2.3×10^{-1}	6.2×10^{-1}
45–50	8.5×10^{0}	6.7×10^{-2}	3.7×10^{-1}	1.3×10^{-1}	4.0×10^{-1}
50–55	6.3×10^{0}	5.5×10^{-2}	2.4×10^{-1}	1.1×10^{-1}	2.7×10^{-1}
55–60	5.3×10^{0}	5.0×10^{-2}	2.0×10^{-1}	9.8×10^{-2}	2.3×10^{-1}
60–64	4.9×10^{0}	5.6×10^{-2}	1.7×10^{-1}	9.7×10^{-2}	2.1×10^{-1}
64–68	4.9×10^{0}	5.8×10^{-2}	1.6×10^{-1}	1.0×10^{-1}	2.0×10^{-1}
68–72	5.4×10^{0}	5.9×10^{-2}	1.8×10^{-1}	1.1×10^{-1}	2.2×10^{-1}
72–76	6.5×10^{0}	6.8×10^{-2}	2.0×10^{-1}	1.4×10^{-1}	2.5×10^{-1}
76–81	9.7×10^{0}	7.0×10^{-2}	3.0×10^{-1}	2.0×10^{-1}	3.7×10^{-1}
81–86	2.1×10^{1}	1.1×10^{-1}	6.5×10^{-1}	4.2×10^{-1}	7.9×10^{-1}
86–91	1.5×10^{2}	2.7×10^{-1}	5.0×10^{0}	2.9×10^{0}	5.8×10^{0}
91–96	1.6×10^{2}	2.7×10^{-1}	5.9×10^{0}	3.1×10^{0}	6.6×10^{0}
96–101	1.4×10^{1}	8.5×10^{-2}	5.3×10^{-1}	2.4×10^{-1}	5.9×10^{-1}
101–106	4.9×10^{0}	4.8×10^{-2}	2.0×10^{-1}	7.6×10^{-2}	2.2×10^{-1}
106–110	2.5×10^{0}	4.3×10^{-2}	1.1×10^{-1}	3.6×10^{-2}	1.2×10^{-1}
110–115	1.7×10^{0}	2.8×10^{-2}	7.1×10^{-2}	2.2×10^{-2}	8.0×10^{-2}
115–120	1.1×10^{0}	2.3×10^{-2}	4.7×10^{-2}	1.3×10^{-2}	5.4×10^{-2}

Table D.2: Summary of the measured values of $d\sigma/dm$ (pb/GeV) in the dimuon channel ($m > 120\,\text{GeV}$) with the statistical (δ_{stat}), experimental (δ_{exp}) and theoretical (δ_{theo}) uncertainties, respectively. Here, δ_{tot} is the quadratic sum of the three components.

m(GeV)	$\frac{d\sigma}{dm}$ (pb/GeV)	δ_{stat}	δ_{exp}	δ_{theo}	δ_{tot}
120–126	7.6×10^{-1}	1.8×10^{-2}	3.5×10^{-2}	8.6×10^{-3}	4.1×10^{-2}
126–133	5.2×10^{-1}	1.3×10^{-2}	2.6×10^{-2}	5.5×10^{-3}	2.9×10^{-2}
133–141	3.7×10^{-1}	1.0×10^{-2}	1.9×10^{-2}	3.8×10^{-3}	2.2×10^{-2}
141–150	2.7×10^{-1}	8.0×10^{-3}	1.6×10^{-2}	2.7×10^{-3}	1.8×10^{-2}
150–160	1.9×10^{-1}	6.1×10^{-3}	1.1×10^{-2}	1.8×10^{-3}	1.3×10^{-2}
160–171	1.4×10^{-1}	5.3×10^{-3}	9.1×10^{-3}	1.6×10^{-3}	1.1×10^{-2}
171–185	9.1×10^{-2}	3.6×10^{-3}	6.4×10^{-3}	8.0×10^{-4}	7.3×10^{-3}
185–200	6.3×10^{-2}	2.9×10^{-3}	4.7×10^{-3}	6.5×10^{-4}	5.6×10^{-3}
200–220	4.4×10^{-2}	1.9×10^{-3}	3.6×10^{-3}	5.1×10^{-4}	4.1×10^{-3}
220–243	3.0×10^{-2}	1.5×10^{-3}	2.7×10^{-3}	2.7×10^{-4}	3.1×10^{-3}
243–273	1.7×10^{-2}	9.8×10^{-4}	1.7×10^{-3}	1.3×10^{-4}	2.0×10^{-3}
273–320	9.9×10^{-3}	5.4×10^{-4}	1.1×10^{-3}	7.2×10^{-5}	1.2×10^{-3}
320–380	5.3×10^{-3}	3.4×10^{-4}	6.0×10^{-4}	3.4×10^{-5}	6.9×10^{-4}
380–440	1.6×10^{-3}	2.3×10^{-4}	1.9×10^{-4}	1.2×10^{-5}	3.0×10^{-4}
440–510	1.1×10^{-3}	1.5×10^{-4}	1.3×10^{-4}	6.8×10^{-6}	2.0×10^{-4}
510–600	5.7×10^{-4}	8.9×10^{-5}	7.1×10^{-5}	2.6×10^{-6}	1.1×10^{-4}
600–700	3.2×10^{-4}	6.2×10^{-5}	4.0×10^{-5}	9.6×10^{-7}	7.4×10^{-5}
700–830	8.3×10^{-5}	3.0×10^{-5}	1.8×10^{-5}	3.8×10^{-7}	3.5×10^{-5}
830–1000	5.5×10^{-5}	1.8×10^{-5}	1.1×10^{-5}	4.1×10^{-7}	2.1×10^{-5}
1000–1500	1.1×10^{-5}	4.1×10^{-6}	2.3×10^{-6}	1.3×10^{-7}	4.7×10^{-6}
1500–3000	2.4×10^{-7}	2.4×10^{-7}	3.8×10^{-7}	4.2×10^{-9}	4.5×10^{-7}

Table D.3: Summary of the measured values of $d\sigma/dm$ (pb/GeV) in the dielectron channel ($m < 120\,\text{GeV}$) with the statistical (δ_{stat}), experimental (δ_{exp}) and theoretical (δ_{theo}) uncertainties, respectively. Here, δ_{tot} is the quadratic sum of the three components.

m(GeV)	$\frac{d\sigma}{dm}$ (pb/GeV)	δ_{stat}	δ_{exp}	δ_{theo}	δ_{tot}
15–20	2.2×10^{2}	5.4×10^{0}	1.2×10^{1}	1.2×10^{1}	1.8×10^{1}
20–25	1.0×10^{2}	3.0×10^{0}	5.4×10^{0}	4.8×10^{0}	7.9×10^{0}
25–30	5.1×10^{1}	1.8×10^{0}	2.8×10^{0}	4.9×10^{0}	5.9×10^{0}
30–35	2.8×10^{1}	1.1×10^{0}	1.6×10^{0}	4.3×10^{0}	4.7×10^{0}
35–40	1.9×10^{1}	7.3×10^{-1}	1.3×10^{0}	3.0×10^{0}	3.3×10^{0}
40–45	1.1×10^{1}	4.6×10^{-1}	8.5×10^{-1}	1.6×10^{0}	1.8×10^{0}
45–50	8.2×10^{0}	3.2×10^{-1}	6.3×10^{-1}	9.5×10^{-1}	1.2×10^{0}
50–55	5.7×10^{0}	2.6×10^{-1}	4.2×10^{-1}	5.3×10^{-1}	7.3×10^{-1}
55–60	5.7×10^{0}	2.1×10^{-1}	3.9×10^{-1}	4.3×10^{-1}	6.1×10^{-1}
60–64	4.3×10^{0}	2.6×10^{-1}	2.7×10^{-1}	2.8×10^{-1}	4.7×10^{-1}
64–68	4.8×10^{0}	2.4×10^{-1}	2.7×10^{-1}	2.7×10^{-1}	4.5×10^{-1}
68–72	5.5×10^{0}	2.7×10^{-1}	2.8×10^{-1}	2.6×10^{-1}	4.7×10^{-1}
72–76	6.8×10^{0}	2.8×10^{-1}	3.0×10^{-1}	2.7×10^{-1}	4.9×10^{-1}
76–81	1.0×10^{1}	2.9×10^{-1}	3.8×10^{-1}	3.4×10^{-1}	5.9×10^{-1}
81–86	2.4×10^{1}	3.8×10^{-1}	8.2×10^{-1}	6.8×10^{-1}	1.1×10^{0}
86–91	1.5×10^{2}	6.0×10^{-1}	4.8×10^{0}	3.4×10^{0}	5.9×10^{0}
91–96	1.5×10^{2}	5.4×10^{-1}	5.2×10^{0}	3.0×10^{0}	6.1×10^{0}
96–101	1.3×10^{1}	1.8×10^{-1}	4.7×10^{-1}	2.1×10^{-1}	5.5×10^{-1}
101–106	4.9×10^{0}	1.0×10^{-1}	1.9×10^{-1}	6.7×10^{-2}	2.2×10^{-1}
106–110	2.6×10^{0}	9.5×10^{-2}	1.2×10^{-1}	3.2×10^{-2}	1.5×10^{-1}
110–115	1.5×10^{0}	6.2×10^{-2}	7.7×10^{-2}	1.7×10^{-2}	1.0×10^{-1}
115–120	1.1×10^{0}	4.8×10^{-2}	5.6×10^{-2}	1.2×10^{-2}	7.5×10^{-2}

Table D.4: Summary of the measured values of $d\sigma/dm$ (pb/GeV) in the dielectron channel ($m > 120\,\text{GeV}$) with the statistical (δ_{stat}), experimental (δ_{exp}) and theoretical (δ_{theo}) uncertainties, respectively. Here, δ_{tot} is the quadratic sum of the three components.

m(GeV)	$\frac{d\sigma}{dm}$ (pb/GeV)	δ_{stat}	δ_{exp}	δ_{theo}	δ_{tot}
120–126	7.9×10^{-1}	3.5×10^{-2}	4.2×10^{-2}	8.8×10^{-3}	5.6×10^{-2}
126–133	5.7×10^{-1}	2.5×10^{-2}	3.7×10^{-2}	6.6×10^{-3}	4.5×10^{-2}
133–141	3.3×10^{-1}	1.9×10^{-2}	2.7×10^{-2}	3.9×10^{-3}	3.3×10^{-2}
141–150	3.1×10^{-1}	1.6×10^{-2}	2.7×10^{-2}	3.6×10^{-3}	3.1×10^{-2}
150–160	1.7×10^{-1}	1.1×10^{-2}	1.5×10^{-2}	1.9×10^{-3}	1.9×10^{-2}
160–171	1.4×10^{-1}	8.9×10^{-3}	1.3×10^{-2}	1.4×10^{-3}	1.6×10^{-2}
171–185	1.0×10^{-1}	6.5×10^{-3}	9.8×10^{-3}	9.0×10^{-4}	1.2×10^{-2}
185–200	5.4×10^{-2}	4.4×10^{-3}	5.4×10^{-3}	4.6×10^{-4}	6.9×10^{-3}
200–220	4.3×10^{-2}	3.2×10^{-3}	4.3×10^{-3}	3.8×10^{-4}	5.4×10^{-3}
220–243	3.0×10^{-2}	2.4×10^{-3}	3.2×10^{-3}	2.2×10^{-4}	4.0×10^{-3}
243–273	1.5×10^{-2}	1.5×10^{-3}	1.6×10^{-3}	1.0×10^{-4}	2.2×10^{-3}
273–320	9.3×10^{-3}	7.9×10^{-4}	9.9×10^{-4}	6.0×10^{-5}	1.3×10^{-3}
320–380	4.9×10^{-3}	5.0×10^{-4}	5.2×10^{-4}	2.8×10^{-5}	7.2×10^{-4}
380–440	2.8×10^{-3}	3.6×10^{-4}	3.2×10^{-4}	1.3×10^{-5}	4.8×10^{-4}
440–510	5.0×10^{-4}	1.9×10^{-4}	6.4×10^{-5}	2.0×10^{-6}	2.0×10^{-4}
510–600	5.9×10^{-4}	1.2×10^{-4}	8.3×10^{-5}	2.2×10^{-6}	1.4×10^{-4}
600–700	3.2×10^{-4}	8.2×10^{-5}	5.6×10^{-5}	1.0×10^{-6}	1.0×10^{-4}
700–830	5.9×10^{-5}	3.5×10^{-5}	1.4×10^{-5}	1.7×10^{-7}	3.8×10^{-5}
830–1000	9.6×10^{-6}	5.6×10^{-6}	4.3×10^{-6}	2.5×10^{-8}	7.1×10^{-6}
1000–1500	9.1×10^{-6}	5.0×10^{-6}	7.5×10^{-6}	3.3×10^{-8}	9.0×10^{-6}
1500–3000	4.3×10^{-7}	4.3×10^{-7}	4.4×10^{-7}	2.8×10^{-9}	6.2×10^{-7}

Table D.5: Summary of the measured values of fiducial $d\sigma/dm$ (pb/GeV) (with no FSR correction applied) in the dimuon channel ($m < 120\,\text{GeV}$) with the statistical (δ_{stat}) and experimental (δ_{exp}) uncertainties shown separately. Here, δ_{tot} is the quadratic sum of the two components.

m(GeV)	$\frac{d\sigma}{dm}$ (pb/GeV)	δ_{stat}	δ_{exp}	δ_{tot}
15–20	1.2×10^{0}	1.1×10^{-2}	5.5×10^{-2}	5.6×10^{-2}
20–25	9.0×10^{-1}	9.8×10^{-3}	4.0×10^{-2}	4.2×10^{-2}
25–30	9.2×10^{-1}	1.1×10^{-2}	4.2×10^{-2}	4.3×10^{-2}
30–35	1.3×10^{0}	1.3×10^{-2}	6.1×10^{-2}	6.3×10^{-2}
35–40	1.7×10^{0}	1.5×10^{-2}	8.6×10^{-2}	8.7×10^{-2}
40–45	2.1×10^{0}	1.7×10^{-2}	1.0×10^{-1}	1.0×10^{-1}
45–50	2.3×10^{0}	1.7×10^{-2}	1.0×10^{-1}	1.0×10^{-1}
50–55	2.1×10^{0}	1.7×10^{-2}	8.1×10^{-2}	8.2×10^{-2}
55–60	2.1×10^{0}	1.7×10^{-2}	7.5×10^{-2}	7.7×10^{-2}
60–64	2.2×10^{0}	2.0×10^{-2}	7.2×10^{-2}	7.5×10^{-2}
64–68	2.4×10^{0}	2.2×10^{-2}	7.2×10^{-2}	7.6×10^{-2}
68–72	2.8×10^{0}	2.3×10^{-2}	8.1×10^{-2}	8.4×10^{-2}
72–76	3.5×10^{0}	2.7×10^{-2}	9.6×10^{-2}	9.9×10^{-2}
76–81	5.4×10^{0}	2.8×10^{-2}	1.4×10^{-1}	1.5×10^{-1}
81–86	1.1×10^{1}	4.5×10^{-2}	3.1×10^{-1}	3.1×10^{-1}
86–91	6.8×10^{1}	1.1×10^{-1}	2.0×10^{0}	2.0×10^{0}
91–96	6.9×10^{1}	1.1×10^{-1}	2.2×10^{0}	2.2×10^{0}
96–101	6.1×10^{0}	3.6×10^{-2}	2.1×10^{-1}	2.1×10^{-1}
101–106	2.2×10^{0}	2.0×10^{-2}	7.8×10^{-2}	8.1×10^{-2}
106–110	1.2×10^{0}	1.9×10^{-2}	4.3×10^{-2}	4.7×10^{-2}
110–115	7.6×10^{-1}	1.2×10^{-2}	3.0×10^{-2}	3.2×10^{-2}
115–120	5.0×10^{-1}	1.0×10^{-2}	2.1×10^{-2}	2.3×10^{-2}

Table D.6: Summary of the measured values of fiducial $d\sigma/dm$ (pb/GeV) (with no FSR correction applied) in the dimuon channel ($m > 120\,\text{GeV}$) with the statistical (δ_{stat}) and experimental (δ_{exp}) uncertainties shown separately. Here, δ_{tot} is the quadratic sum of the two components.

m(GeV)	$\frac{d\sigma}{dm}$ (pb/GeV)	δ_{stat}	δ_{exp}	δ_{tot}
120–126	3.6×10^{-1}	7.9×10^{-3}	1.6×10^{-2}	1.8×10^{-2}
126–133	2.5×10^{-1}	5.8×10^{-3}	1.2×10^{-2}	1.3×10^{-2}
133–141	1.8×10^{-1}	4.5×10^{-3}	8.9×10^{-3}	1.0×10^{-2}
141–150	1.3×10^{-1}	3.7×10^{-3}	7.2×10^{-3}	8.1×10^{-3}
150–160	9.4×10^{-2}	2.9×10^{-3}	5.3×10^{-3}	6.1×10^{-3}
160–171	6.9×10^{-2}	2.5×10^{-3}	4.2×10^{-3}	4.9×10^{-3}
171–185	4.7×10^{-2}	1.7×10^{-3}	3.1×10^{-3}	3.6×10^{-3}
185–200	3.3×10^{-2}	1.4×10^{-3}	2.4×10^{-3}	2.8×10^{-3}
200–220	2.4×10^{-2}	9.7×10^{-4}	1.9×10^{-3}	2.1×10^{-3}
220–243	1.6×10^{-2}	7.7×10^{-4}	1.4×10^{-3}	1.6×10^{-3}
243–273	9.8×10^{-3}	5.3×10^{-4}	9.4×10^{-4}	1.1×10^{-3}
273–320	5.8×10^{-3}	3.1×10^{-4}	6.0×10^{-4}	6.7×10^{-4}
320–380	3.2×10^{-3}	2.0×10^{-4}	3.4×10^{-4}	3.9×10^{-4}
380–440	1.0×10^{-3}	1.4×10^{-4}	1.2×10^{-4}	1.8×10^{-4}
440–510	7.2×10^{-4}	9.6×10^{-5}	8.5×10^{-5}	1.3×10^{-4}
510–600	4.0×10^{-4}	6.0×10^{-5}	4.8×10^{-5}	7.6×10^{-5}
600–700	2.3×10^{-4}	4.3×10^{-5}	2.7×10^{-5}	5.0×10^{-5}
700–830	6.4×10^{-5}	2.1×10^{-5}	1.4×10^{-5}	2.5×10^{-5}
830–1000	4.2×10^{-5}	1.4×10^{-5}	8.4×10^{-6}	1.6×10^{-5}
1000–1500	8.9×10^{-6}	3.3×10^{-6}	1.8×10^{-6}	3.8×10^{-6}
1500–3000	2.1×10^{-7}	2.1×10^{-7}	3.2×10^{-7}	3.8×10^{-7}

Table D.7: Summary of the measured values of fiducial $d\sigma/dm$ (pb/GeV) (with no FSR correction applied) in the dielectron channel ($m < 120\,\text{GeV}$) with the statistical (δ_{stat}) and experimental (δ_{exp}) uncertainties shown separately. Here, δ_{tot} is the quadratic sum of the two components.

m(GeV)	$\frac{d\sigma}{dm}$ (pb/GeV)	δ_{stat}	δ_{exp}	δ_{tot}
15–20	5.5×10^{-1}	1.3×10^{-2}	2.3×10^{-2}	2.6×10^{-2}
20–25	4.4×10^{-1}	1.2×10^{-2}	1.9×10^{-2}	2.3×10^{-2}
25–30	3.9×10^{-1}	1.2×10^{-2}	1.7×10^{-2}	2.1×10^{-2}
30–35	3.6×10^{-1}	1.3×10^{-2}	1.7×10^{-2}	2.2×10^{-2}
35–40	5.1×10^{-1}	1.8×10^{-2}	2.9×10^{-2}	3.4×10^{-2}
40–45	6.7×10^{-1}	2.3×10^{-2}	4.1×10^{-2}	4.7×10^{-2}
45–50	1.0×10^{0}	3.1×10^{-2}	6.7×10^{-2}	7.4×10^{-2}
50–55	1.2×10^{0}	3.8×10^{-2}	8.0×10^{-2}	8.9×10^{-2}
55–60	1.8×10^{0}	4.3×10^{-2}	1.1×10^{-1}	1.2×10^{-1}
60–64	2.0×10^{0}	6.0×10^{-2}	1.2×10^{-1}	1.4×10^{-1}
64–68	2.6×10^{0}	6.7×10^{-2}	1.4×10^{-1}	1.6×10^{-1}
68–72	3.2×10^{0}	7.6×10^{-2}	1.6×10^{-1}	1.8×10^{-1}
72–76	4.3×10^{0}	8.3×10^{-2}	1.9×10^{-1}	2.0×10^{-1}
76–81	6.5×10^{0}	8.7×10^{-2}	2.4×10^{-1}	2.5×10^{-1}
81–86	1.4×10^{1}	1.2×10^{-1}	4.3×10^{-1}	4.5×10^{-1}
86–91	5.9×10^{1}	1.9×10^{-1}	1.7×10^{0}	1.7×10^{0}
91–96	5.0×10^{1}	1.7×10^{-1}	1.4×10^{0}	1.4×10^{0}
96–101	4.7×10^{0}	5.9×10^{-2}	1.4×10^{-1}	1.5×10^{-1}
101–106	1.8×10^{0}	3.4×10^{-2}	5.8×10^{-2}	6.7×10^{-2}
106–110	1.0×10^{0}	3.1×10^{-2}	4.0×10^{-2}	5.1×10^{-2}
110–115	6.1×10^{-1}	2.1×10^{-2}	2.8×10^{-2}	3.5×10^{-2}
115–120	4.4×10^{-1}	1.7×10^{-2}	2.1×10^{-2}	2.7×10^{-2}

Table D.8: Summary of the measured values of fiducial $d\sigma/dm$ (pb/GeV) (with no FSR correction applied) in the dielectron channel ($m > 120\,\text{GeV}$) with the statistical (δ_{stat}) and experimental (δ_{exp}) uncertainties shown separately. Here, δ_{tot} is the quadratic sum of the two components.

m(GeV)	$\frac{d\sigma}{dm}$ (pb/GeV)	δ_{stat}	δ_{exp}	δ_{tot}
120–126	3.3×10^{-1}	1.3×10^{-2}	1.5×10^{-2}	1.9×10^{-2}
126–133	2.4×10^{-1}	9.3×10^{-3}	1.1×10^{-2}	1.4×10^{-2}
133–141	1.4×10^{-1}	7.0×10^{-3}	7.0×10^{-3}	9.9×10^{-3}
141–150	1.3×10^{-1}	5.9×10^{-3}	7.0×10^{-3}	9.2×10^{-3}
150–160	7.9×10^{-2}	4.4×10^{-3}	4.4×10^{-3}	6.3×10^{-3}
160–171	6.2×10^{-2}	3.5×10^{-3}	3.7×10^{-3}	5.1×10^{-3}
171–185	4.6×10^{-2}	2.6×10^{-3}	3.0×10^{-3}	3.9×10^{-3}
185–200	2.7×10^{-2}	1.9×10^{-3}	1.9×10^{-3}	2.6×10^{-3}
200–220	2.1×10^{-2}	1.4×10^{-3}	1.5×10^{-3}	2.1×10^{-3}
220–243	1.5×10^{-2}	1.1×10^{-3}	1.1×10^{-3}	1.6×10^{-3}
243–273	7.9×10^{-3}	6.7×10^{-4}	6.4×10^{-4}	9.3×10^{-4}
273–320	5.0×10^{-3}	4.0×10^{-4}	4.2×10^{-4}	5.8×10^{-4}
320–380	2.8×10^{-3}	2.6×10^{-4}	2.4×10^{-4}	3.5×10^{-4}
380–440	1.6×10^{-3}	1.9×10^{-4}	1.5×10^{-4}	2.4×10^{-4}
440–510	3.4×10^{-4}	1.1×10^{-4}	3.6×10^{-5}	1.1×10^{-4}
510–600	3.7×10^{-4}	6.6×10^{-5}	4.3×10^{-5}	7.9×10^{-5}
600–700	1.9×10^{-4}	4.9×10^{-5}	2.7×10^{-5}	5.5×10^{-5}
700–830	3.9×10^{-5}	2.2×10^{-5}	7.6×10^{-6}	2.3×10^{-5}
830–1000	8.0×10^{-6}	4.6×10^{-6}	3.4×10^{-6}	5.7×10^{-6}
1000–1500	6.6×10^{-6}	3.5×10^{-6}	5.4×10^{-6}	6.4×10^{-6}
1500–3000	3.2×10^{-7}	3.2×10^{-7}	3.2×10^{-7}	4.6×10^{-7}

Table D.9: Summary of the combined values of $d\sigma/dm$ (pb/GeV) using the results from both the dimuon and dielectron channels ($m < 120\,\text{GeV}$). Here, δ_{tot} is the quadratic sum of the statistical, experimental and theoretical uncertainties.

m(GeV)	$\frac{d\sigma}{dm}$ (pb/GeV)	δ_{tot}
15–20	2.3×10^{2}	1.6×10^{1}
20–25	1.0×10^{2}	6.3×10^{0}
25–30	5.2×10^{1}	5.7×10^{0}
30–35	2.8×10^{1}	3.0×10^{0}
35–40	1.8×10^{1}	1.3×10^{0}
40–45	1.2×10^{1}	6.1×10^{-1}
45–50	8.5×10^{0}	3.9×10^{-1}
50–55	6.2×10^{0}	2.7×10^{-1}
55–60	5.4×10^{0}	2.3×10^{-1}
60–64	4.8×10^{0}	2.0×10^{-1}
64–68	4.9×10^{0}	2.0×10^{-1}
68–72	5.4×10^{0}	2.2×10^{-1}
72–76	6.6×10^{0}	2.6×10^{-1}
76–81	9.8×10^{0}	3.7×10^{-1}
81–86	2.2×10^{1}	7.9×10^{-1}
86–91	1.5×10^{2}	5.2×10^{0}
91–96	1.6×10^{2}	5.6×10^{0}
96–101	1.3×10^{1}	4.8×10^{-1}
101–106	4.9×10^{0}	1.8×10^{-1}
106–110	2.6×10^{0}	1.1×10^{-1}
110–115	1.6×10^{0}	6.8×10^{-2}
115–120	1.1×10^{0}	4.7×10^{-2}

Table D.10: Summary of the combined values of $d\sigma/dm$ (pb/GeV) using the results from both the dimuon and dielectron channels ($m > 120\,\text{GeV}$). Here, δ_{tot} is the quadratic sum of the statistical, experimental and theoretical uncertainties.

m(GeV)	$\frac{d\sigma}{dm}$ (pb/GeV)	δ_{tot}
120–126	7.7×10^{-1}	3.5×10^{-2}
126–133	5.4×10^{-1}	2.6×10^{-2}
133–141	3.6×10^{-1}	1.9×10^{-2}
141–150	2.8×10^{-1}	1.6×10^{-2}
150–160	1.8×10^{-1}	1.1×10^{-2}
160–171	1.4×10^{-1}	9.1×10^{-3}
171–185	9.4×10^{-2}	6.4×10^{-3}
185–200	6.0×10^{-2}	4.5×10^{-3}
200–220	4.4×10^{-2}	3.3×10^{-3}
220–243	3.0×10^{-2}	2.5×10^{-3}
243–273	1.6×10^{-2}	1.5×10^{-3}
273–320	9.6×10^{-3}	8.9×10^{-4}
320–380	5.1×10^{-3}	5.0×10^{-4}
380–440	1.9×10^{-3}	2.5×10^{-4}
440–510	7.9×10^{-4}	1.4×10^{-4}
510–600	5.8×10^{-4}	8.9×10^{-5}
600–700	3.2×10^{-4}	6.0×10^{-5}
700–830	7.2×10^{-5}	2.6×10^{-5}
830–1000	1.4×10^{-5}	6.7×10^{-6}
1000–1500	1.1×10^{-5}	4.2×10^{-6}
1500–3000	3.1×10^{-7}	3.6×10^{-7}

초록

본 연구에서는 뮤온 채널(muon channel)과 전자 채널(electron channel)에서 두 렙톤(lepton)의 불변 질량(invariant mass)에 대한 드렐-얀 과정(Drell-Yan process)의 미분 산란 단면적을 15 GeV 부터 3000 GeV 까지 측정하였다. 이를 통해 표준 모형(standard model)에 대한 정밀한 검증 뿐만 아니라 양성자 구조에 대한 이해를 향상시키는 데 목적이 있다. 이 결과는 넓은 불변 질량 범위에 대한 드렐-얀 산란단면적 측정 중 13 TeV 질량 중심 에너지 데이터를 사용한 첫 번째 결과이다. 이 연구에서는 대형 강입자 충돌기(Large Hadron Collider)의 CMS (Compact Muon Solenoid) 검출기에서 받은 양성자-양성자 충돌 데이터를 사용하였으며, 누적 광도(integrated luminosity)는 뮤온 채널과 전자 채널 각각 2.8fb^{-1} 과 2.3fb^{-1} 이다. 각 채널에서의 미분 산란 단면적은 이론적인 보정치를 추가한 것과 추가하지 않은 것, 두 가지 모두 포함하였다. 또한, 더 나은 정밀도를 위해 두 채널 결과의 결합도 진행하였다. 미분 산란단면적 결과는 양자 색역학(quantum chromodynamics)의 예측과 비교하였으며 주어진 정밀도 내에서 잘 일치함을 확인하였다.

주요어: 서울대학교, 고에너지물리학, LHC, CMS, Drell-Yan, 산란단면적, 졸업논문

학번: 2014-21367